VOLUME 6 NUMBER 3-4 2019 ISSN 2409-6121; eISSN 2522-1361

Physical Sciences and Technology

National Nanotechnological Laboratory of Open Type
Institute of Experimental and Theoretical Physics

Physical Sciences and Technology is publishing two number in a year by al-Farabi Kazakh National University, al-Farabi ave., 71, 050040, Almaty, the Republic of Kazakhstan
website: http://phst.kaznu.kz/

Any inquiry for subscriptions should be send to:
Gauhar Mussabek, al-Farabi Kazakh National University
al-Farabi ave., 71, 050040, Almaty, the Republic of Kazakhstan
e-mail: gauharmussabek@gmail.com

SCOPE AND AIM

Physical Sciences and Technology provides an original paperback for the publication of peerreviewed research and review articles in all fields of Physics and related Technology. The topics, included in the scope, especially emphasize understanding of the physics underlying modern technology.

Subject areas may include, but are not limited to the following fields: Astronomy and Space Research, Theoretical Physics and Astrophysics, Plasma Physics and Related Technology, Chemical Physics and Related Technology, Condensed Matter Physics and Related Technology, Thermal physics and Related Technology, Nuclear Physics and Related Technology, Nanomaterials and Nanotechnology, Applied Atomic and Molecular Physics, Material Sciences and Related Technology, Electronics and Related Technology, Instrumentation, Photonics and Quantum Electronics, Signal processing.

The Journal is issued under the auspices of the National Nanotechnological Laboratory of Open Type and Institute of Experimental and Theoretical Physics and is published two times a year by the «Kazakh University» Publishing House. The International Editorial Board of the Journal consists of leading researchers from different countries of the world. The Journal is wide open for contributions that both lie at the far frontiers of contemporary physics and are particularly aimed at applications of the scientific principles of physics to modern technological problems.

IRSTI 29.27.01, 29.19.01 https://doi.org/10.26577/phst-2019-2-p1

Quantum methods in the development of new materials

E. Son[1*], I. Abrikosov[2], A. Khvan[2] and P. Levashov[1]

[1]*Joint Institute for High Temperature RAS, 13/2 Izhorskaya St., 125412, Moscow, Russia*
[2]*Moscow Institute of Steel and Alloys, 9 Leninsky Prospect, 119049, Moscow, Russia*
[*]*e-mail: son.eduard@gmail.com*

The analysis of quantum methods for supercomputer simulations “ab initio”, quantum Monte-Carlo (QMC), Density Functional Theory (DFT) and semiempirical approaches like Tomas-Fermi at finite temperatures (TFFT) for gas, plasma and solid phases equilibrium thermodynamics and transport properties are presented. Thermodynamic potentials, entropy, specific enthalpy and their derivatives, specific heat capacity, velocity of sound, shock wave entropy behavior, diffusion, thermal and electrical conductivity, dielectric functions of the new materials for Atomic Energy Industry are analysed. The results are presented in the developed Data Base of Atomic Materials. Equation of state for aluminium melting, temperature dependence of Al thermal conductivity, the thermal pressure of the electrons for tungsten and Al dielectric function are obtained on the basis of experiment and simulation and compared with other works. Al shock adiabats, Al temperature – density and Al sound velocity are analysed by using QMD and MPTEOS simulations. Porous W pressure – mass velocity is investigated using experiments and simulations by QMD.

Key words: Material Data Base, DFT, QMC, Monte Carlo, Tomas-Fermi, EOS.
PACS numbers: 52.65.y, 64.30.t, 64.60.De

1. Introduction

The progress in the real acceleration in the number of available materials is associated with an increase in the information component in their development. Exponential growth in computing power and data storage density, combined with advances in computer science (e-science), have produced an information revolution. Big Data management techniques have now found use in information retrieval technologies, Life Sciences, Economics, Social Media, etc. Recently, an innovative idea has been formulated to integrate materials development techniques with data management technologies, the so-called Materials Informatics (MI) or Materials Genome (MG). Its implementation will bring a change in the basic paradigm in Materials Science (MS), replacing the traditional method of trial and error with a highly productive scientifically-based approach. A number of countries have already launched programs with strong government support in this direction, such as “The Center for the Design of Materials for Functional Electronics” in the United States. In 2016, three Centers of Excellence for the study of Big Data sets management in Materials Science begin their activities in Europe: MAX, NOMAD and ECAM. It is very important for Russia to take a leading role in this area. To this aim, we propose Interdisciplinary Project "Genome of nuclear energy materials" with the Rosatom (Russian Atomic Energy Commission) collaboration.

The task is set as follows. To create materials for the new types of reactors, to ensure the safety of existing nuclear power plants, there are problems with the creation of materials with properties that would meet the requirements of standards, long-term operation and reliability. After determining the required properties of the materials on the basis of existing interactive (constantly updated and corrected) databases can be analyzed candidates for new materials. Then the first-principle (ab-initio) calculations are made and the molecular structure of the new material is determined. After that, the technologies for obtaining these materials are determined and, as a rule, a new material is created on the basis of additive technologies. The resulting material must pass a full cycle of testing and certification. The proposed approach, which includes the use of interactive databases, primitive

quantum calculations, technology development and experimental research, is not trivial, but it is the only way that can lead to success in the field of nuclear engineering.

To achieve this goal, an interdisciplinary team of leading researchers with complementary expertise in material modelling, machine learning, database development, visualization, and experimental synthesis and analysis of the properties of new materials is being created. The developed approach will have sufficient potential to significantly reduce, by an order of magnitude or more, the cost, risks and time of discovery of new materials and bringing them to the commercial market.

2 Ab initio calculations and design of solid and liquid materials

2.1 Aims and goals of ab initio calculations

The strategic goal of the project is to provide the possibility of scientifically-based development of new materials based on the management of large data sets, proposed by the revolutionary progress of the theory of modeling, computing power, Informatics, statistics and visualization. We will produce, store and classify large amounts of material data based on our own computer simulations and experiments, as well as from a wide range of literature sources and databases available to us. Research of Big Data sets using effective machine learning (ML) algorithms will allow to discover new materials and phenomena with promising technological applications, to recognize new relations “parameter to properties” and “parameter to parameter”. It will allow to receive qualitatively new ideas, inaccessible for usual methods of research. Indeed, the effectiveness of the transition from data to knowledge depends on the adequacy and correctness of abstraction methods. Examples of successful abstractions are the Periodic table of elements or so-called Ashby diagrams, which graphically select relationships between two or more properties of materials or their classes. Such diagrams are widely used by material scientists and engineers. However, the use of approaches developed for Big Data sets in materials science until recently was limited to excessive labor-intensive experimental data acquisition. With the use of computer modeling, the efficiency of obtaining data on the properties of materials increases significantly. At the same time, the problem of transition from data to knowledge using traditional empirical methods becomes difficult to solve. Using the new revolutionary approaches developed in the framework of our project, we will be able to identify the scientific context of key concepts in materials science, and use it to model and predict the properties and behavior of materials under various conditions and in a variety of applications.

2.2 Review of previous research developed by authors and their research groups

Previous research developed by the group developed Nuclear Gas Core Reactor is presented in [1-3]. The next scientific results for materials were obtained.

* A new generation of materials modeling methods has been developed with qualitatively new possibilities of taking into account real external conditions, namely temperature effects of crystal lattice oscillations, magnetic excitations, as well as multielectronic effects [4-5].

* The applicability of the developed methods to describe the behavior of materials in extreme conditions is demonstrated. A detailed experimental and theoretical study of the behavior of one of the incompressible Os metals at a pressure greater than 770 GPA was carried out, revealing a new type of electronic transition caused by the intersection of internal levels (CLC) [6].

* The importance of multielectronic effects in the case of Fe properties research is shown [4]. It is shown that their consideration leads to a theoretical prediction of the presence of electronic topological transitions in iron under pressure. Experimental measurements of sound velocity as a function of pressure confirm the presence of a transition [8].

* A study of the dependence on the pressure of the magnetic hyperfine field in Nickel oxide NiO [9], which confirmed the antiferromagnetic state of NiO up to 280 GPA. This is the highest pressure where magnetism has been observed so far in any material.

* The influence of stresses and multicomponent alloying on the phase stability of Fe-Cr alloys, which are the base materials for nuclear reactors, is studied [10].

* Within the framework of fundamental interdisciplinary studies, the evidence for stabilization of the Fe-10 at structure of the BCC is presented. % Ni alloys at pressures above 225 GPA and temperatures above 3400 K, and it is theoretically demonstrated that the alloy can be stable in the Earth's core [11].

* In our recent work, the structural properties of graphite and diamond as a function of applied

pressure were calculated using the Density Functional Theory (DFT) and various methods to incorporate the Van der Waals interaction.

* Theoretical and experimental study of structural and magnetic properties of fec O_3 siderite at high pressure and temperature has been performed [12]. The reason for the increase in the Neel temperature and the stability of the AFM state of $FeCO_3$ when the pressure increases relative to the DLM structure is analyzed. It is shown that when heated to the temperature of the Earth's core and pressures above 50 GPA, siderite $FeCO_3$ practically disintegrates into various oxides.

* Peculiarities of pressure influence on properties of carbides and nitrides were studied. Calculations of monocrystalline and polycrystalline elastic properties in the range from 0 to 1200 K, taking into account temperature contributions, were carried out for a technologically important paramagnetic CRN alloy by a new TDEP method with force constant symmetrization [13]. It was shown that there is a significant increase in the isotropy of the elastic properties of CrN with temperature. The influence of anharmonic effects on phase stability was analyzed and physical properties of AlN nitride characterized by unusually high thermal conductivity were determined [14].

* Members of the scientific group have extensive experience in the field of thermodynamic modeling by Calphad methods both for individual substances and in dual and multicomponent systems, as well as in the field of experimental determination of phase rotations and thermodynamic properties, which is reflected in the relevant publications [16-20].

* We reviewed opportunities to improve job modeling in the new pure element database [21].

* As a result of joint work with RWTH Aachen, a detailed experimental analysis of the key system for the development of Fe-Mn-Al-C high manganese compounds was carried out [23-24].

* A new thermodynamic database for Precimn high manganese steels describing the Fe-Mn-Al - Cr-Nb-Si-Ni-Ti-V-C-N system and its subsystems was constructed [26].

* On the basis of thermodynamic calculations the reasons are revealed and recommendations on optimization of compositions of steels for the purpose of elimination of formation of nonmetallic inclusions at welding of HDV of branch pipes are issued

* On the basis of thermodynamic calculations and experimental studies, the causes and mechanisms of formation of harmful inclusions of non-ferrous impurities of non-ferrous metals on the surface of steels made of secondary raw materials were found.

* Work is underway to create a new generation pure and pure element substances database (Calphad 3-0) within the SGTE consortium to replace the existing Pure Elements Database 1991[22, 25].

* The technique of quantitative analysis of integral Auger spectra is developed, which provides an assessment of the content of all elements that can be detected on the surface of brittle intergranular fracture. With the help of the developed technique, spectra from the database of Auger studies of hull reactor steels (CR) obtained at the SIC "Kurchatov Institute" were analyzed.

* The mutual influence of the elements that make up the GZ, correlations between their content (P-C, P-Ni, C-Cr), kinetics of accumulation of P in the GZ are established. Preliminary estimates show that the concentration of P in GZ initially increases, and then, after about 16 and 22 years, respectively, changes slightly. This result is also confirmed by thermodynamic Calphad calculations. For binary systems Me-P and Me-Me3P, where Me = Fe, Cr, Ni, concentrations of phosphide and phosphorus in GZ were calculated at 315 C. Concentrations of iron phosphides (0.012 in mole fractions), chromium (0.014) and Nickel (0.012), and phosphorus (0.041) were obtained. The latter value is well compared with the experimental value of 0.037 obtained after exposure of 195,000 hours (more than 22 years) at T=315 S.

2.3. Example of ab-initio modeling and experimental investigation of the properties of ultra-high temperature solid solutions $Ta_xZr_{1-x}C$

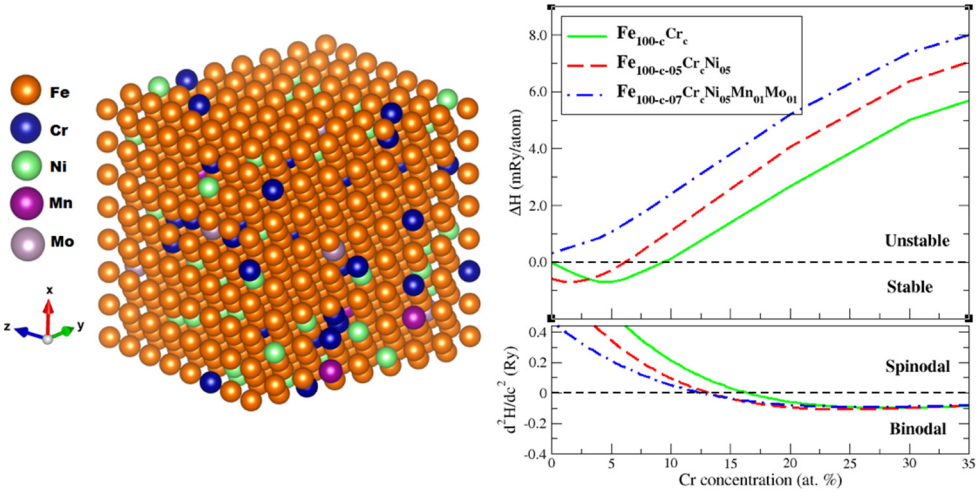

Figure 1 – Effect of multicomponent alloying
with Ni, Mn and Mo on phase stability of bcc Fe-Cr alloys

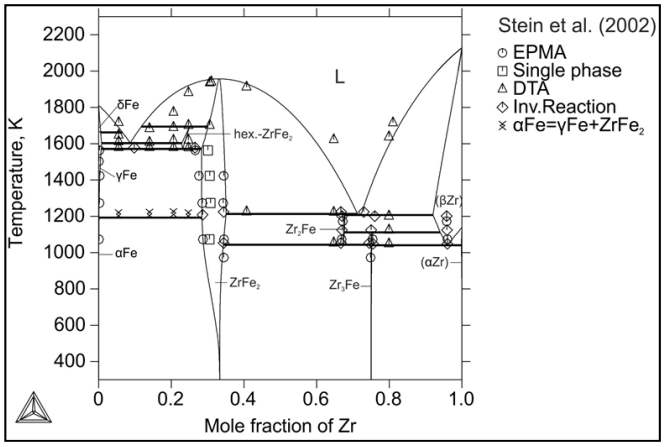

Figure 2 – Re-assessment of Zr-Fe phase diagram [49]

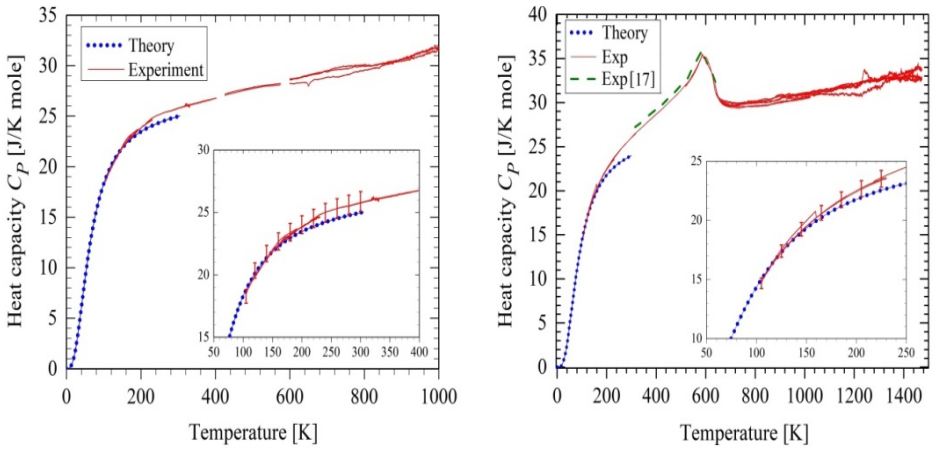

Figure 3 – Heat capacity Zr_3Fe a) and $ZrFe_2$ b) - theory and experiments
(collaboration with Freiberg University of Mining and Technology, Germany)

3 Ab initio calculations and design of liquid and plasma materials including extreme states

3.1. Quantum Molecular Dynamics metals in extreme states

Quantum Molecular Dynamics (VASP)

- Adiabatic Approximation
- Electrons are quantum particles, defined by electron density in DFT at fixed ion positions
- Ions are classical particles in the fields of other ions and electrons described by Newton's laws.
- Number of particles – up to 1000, time simulation 1 ns,
- NVT - Ensemble

The quantum molecular dynamics method allows direct calculation of some thermodynamic functions, including pressure, energy, and heat capacity; additional calculations are necessary to calculate entropy. In addition, the quantum molecular dynamics method approximates the energy spectrum of the system, which makes it possible to apply the Kubo-Greenwood formula to calculate the dynamic Onsager coefficients and calculate the transport and optical electronic properties, including the static coefficients of electrical conductivity and thermal conductivity. Some results of VASP simulations are presented in Figures 4-8.

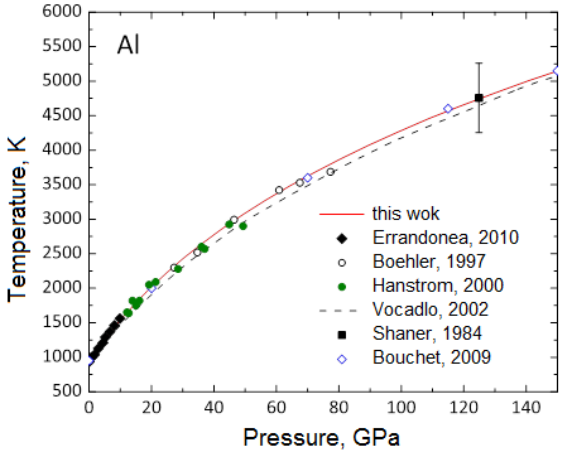

Figure 4 – Aluminum melting experiments and simulations

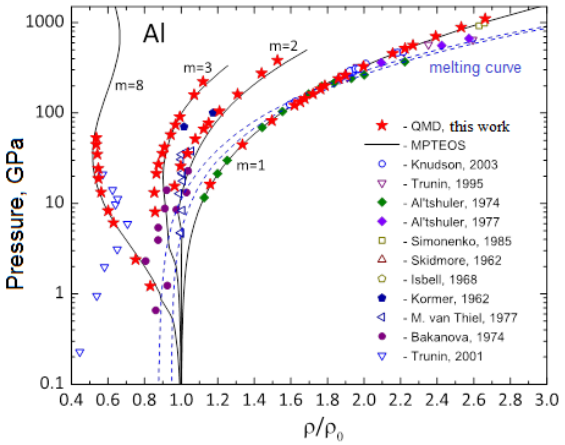

Figure 5 – Al shock adiabats simulations by QMD and MPTEOS

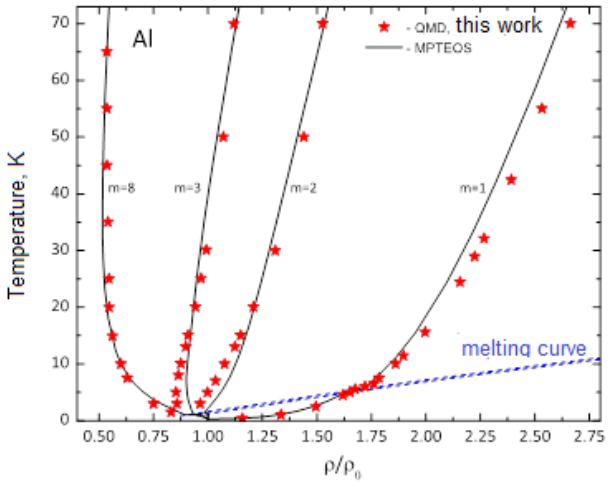

Figure 6 – Al temperature – density simulations by QMD and MPTEOS

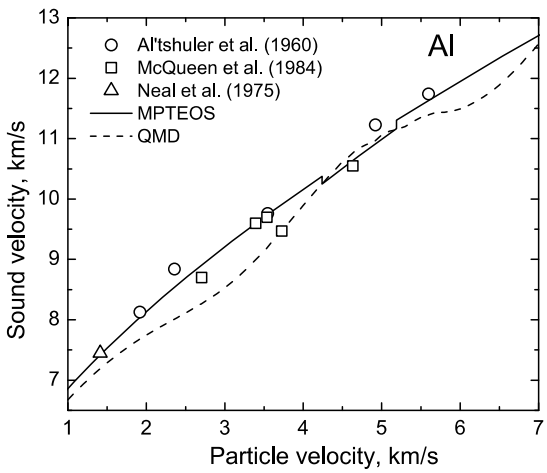

Figure 7 – Al sound velocity, experiments and simulations by QMD and MPTEOS

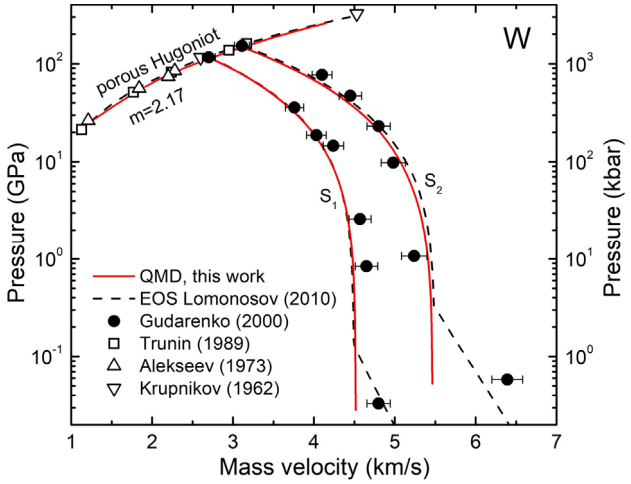

Figure 8 – Porous W pressure – mass velocity, experiments and simulations by QMD

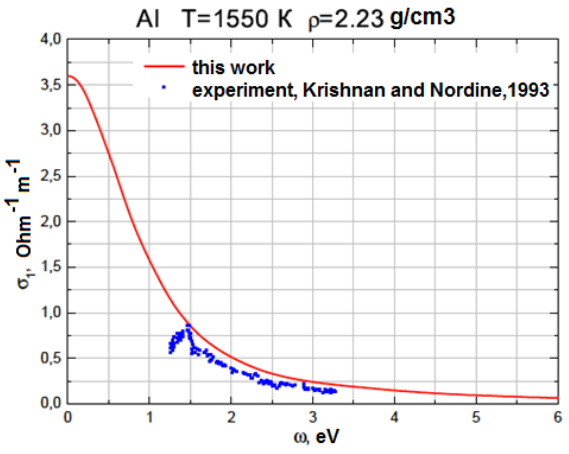

Figure 9 – Al dielectric function simulation and experiment

3.2. Thermodynamic functions in Thomas-Fermi model at finite temperatures

Thomas-Fermi model has been developed for matter thermodynamic properties by Feynman, Metropolis and Teller [50]. In our Data Base approach for high temperature material properties the Thomas- Fermi model in the next formulation. Let V(r) - atomic potential for particle in cell. The Poisson equation has the form of [50]:

$$\Delta V = -4\pi Z\delta(r) + \frac{2}{\pi}(2\theta)^{3/2} I_{1/2}\left(\frac{V(r)+\mu}{\theta}\right)$$

The boundary condition for potential are used for the cell center and at the boundary:

$$rV(r)\big|_{r=0} = Z \qquad V(r_0) = 0 \qquad \frac{dV(r)}{dr}\Big|_{r=r_0} = 0$$

At finite temperature electron densities could be expressed by integrals

$$I_k(x) = \int_0^\infty \frac{y^k dy}{1+\exp(y-x)}$$

Free energy in the canonical ensemble has the form

$$F(V,T) = \frac{2\sqrt{2}\upsilon_a T^{5/2}}{\pi^2}\left[I_{3/2}\left(\frac{\mu}{T}\right) - 8\int_0^1 u^5 I_{3/2}(\phi)\,du + 3\int_0^1 u^5 \phi I_{1/2}(\phi)du\right]$$

Thermodynamic functions could be presented by second derivatives of free energy. For derivatives of pressure and entropy are:

$$P_V^{'} = -F_{VV}^{''} = \frac{(2\theta)^{3/2}}{2\pi^2} I_{1/2}\left(\frac{\mu}{T}\right)\left(\mu_V^{'}\right)_{N,T}$$

$$P_T^{'} = -F_{VT}^{''} = \frac{(2\theta)^{3/2}}{2\pi^2}\left[I_{1/2}\left(\frac{\mu}{T}\right)\left(\mu_T^{'}\right)_{N,V} + \frac{5}{3} I_{3/2}\left(\frac{\mu}{T}\right) - \frac{\mu}{T} I_{1/2}\left(\frac{\mu}{T}\right)\right]$$

$$S_T^{'} = -F_{TT}^{''} = \frac{3\sqrt{2}\upsilon_a}{\pi^2 T^{3/2}}\int_0^1 \left[5T^2u^5 I_{3/2}(\phi) + 3u^3\left(\varphi_T^{'}T^2 - 2\varphi T\right) I_{1/2}(\phi) - u\varphi\left(\varphi_T^{'}T - \varphi\right) I_{-1/2}(\phi)\right] du$$

Internal energy could be found from the 1st law of thermodynamics:

$$E_T = E(V,T) - E(V,0) = \int_0^T T_1 S_T'(V,T_1)\,dT_1$$

Results of simulations are resented in figure 10 for thermal pressure of electrons and temperature dependence of thermal conductivity for aluminum.

4. Data Bases for Atomic Energy materials

All data from ab-initio and semiempirical simulations are used in the Data Base of Atomic Materials on the basis of approach described in [4-48].

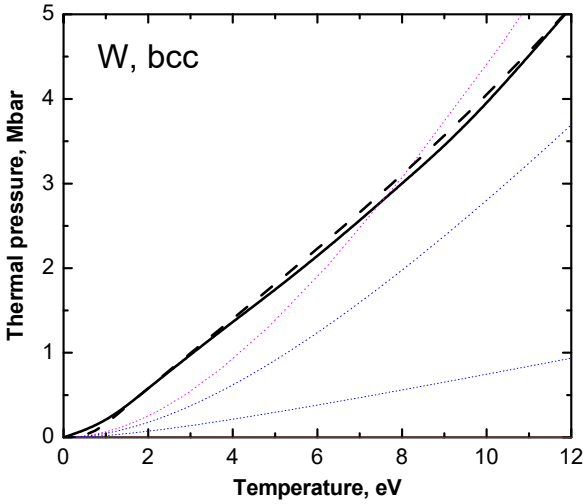

Figure 10 – The thermal pressure of the electrons for Tungsten, ion temperature $T_i = 0$, V = V0.

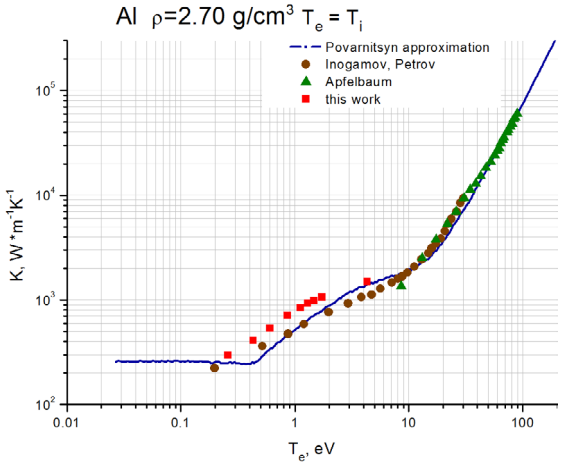

Figure 11 – Temperature dependence of thermal conductivity Al.

5. Conclusions

Modern quantum ab-initio approaches and powerful supercomputers have made it possible to directly calculate the thermophysical properties of substances. In many cases, even today, the calculations can replace the experiment. Calculations are possible for substances of complex composition and structure, this requires significant computing power. The results are presented in the developed Data Base for Atomic Energy Materials.

Acknowledgments. The work was carried out with the financial support of the Ministry of Science and Higher Education of the Russian Federation (unique identifier of PNIER RFMEFI60719X0323**).**

References

1. Gryaznov V. K., Iosilevsky I. L., Krasnikov Y. G., Kuznetsova N. I., Kucherenko V. I., Lappo G. B., Lomakin B. N., Son E. E., Fortov V. E., Editor Ievlev, V.M. (1980) Thermophysical properties of working environments of gas-phase nuclear reactor. M. Atomizdat.

2. Sheindlin M. A., Son E. E. (2011) Lasers in high-temperature energy materials. Izvestiya RAS. Energy, 5, 88-103.

3. Brykin M.V., Son E.E., Sheindlin M.A. (2011) Numerical simulation of the dynamics of noncongruent melting of binary materials. High Temperature, 49, 6, 841–848.

4. Ceder, G., Persson K.A. (2013) The Stuff of Dreams. Scientific American. 309, 6, 36-40.

5. Jain A., Ong Sh.P., Hautier G., Chen W., Richards W.D., Dacek S., Cholia Sh., Gunter D., Skinner D., Ceder G., Persson, K.A. (2013) Commentary: The Materials Project: A materials genome approach to accelerating materials innovation. APL Materials, 1, 011002.

6. http://nomad-coe.eu/; http://www.max-center.eu/; http://www.e-cam2020.eu/

7. Shulumba N., Hellman O., Raza Z., Alling B., Barrirero J., Mücklich F., Abrikosov I.A., Odén, M. (2016) Anharmonicity changes the solid solubility of a random alloy at high temperatures. Phys. Rev. Lett., 117, 205502.

8. Ponomareva A.V., Gornostyrev Yu.N., Abrikosov, I.A. (2014) Ab initio calculations of solution enthalpies of substitutional and interstitial impurities in paramagnetic fcc Fe. Phys. Rev. B, 90, 014439.

9. Dubrovinsky L., Dubrovinskaia N., Bykova E., Abrikosov I.A. (2015) The most incompressible metal Osmium at static pressures above 750 GPa. Nature, 525, 226.

10. Pourovskii L.V., Mravlje J., Ferrero M., Parcollet O., Abrikosov, I.A. (2014) Impact of electronic correlations on the equation of state and transport in ε-Fe. Phys. Rev. B, 90, 155120.

11. Glazyrin K., Pourovskii L.V., Dubrovinsky L., Abrikosov I.A. (2013) Phys. Rev. Lett., 110, 117206.

12. Potapkin V., Dubrovinsky L., Sergueev I., Abrikosov I.A. (2016) Magnetic interactions in NiO at multimegbar pressure. Phys. Rev. B, 93, 201110 (R).

13. Ponomareva, A.V., Ruban, A.V., Vekilova, O.Yu., Abrikosov, I.A. (2011) Effect of pressure on phase stability in Fe-Cr alloys. Phys. Rev. B, 84, 094422;

14. Ponomareva A.V., Ruban A.V., Mukhamedov B.O., Abrikosov I.A. (2018) Effect of multicomponent alloying with Ni, Mn and Mo on phase stability of bcc Fe-Cr alloys. Acta Mater., 150, 117.

15. Golosova N.O., Kozlenko D.P., Dubrovinsky L.S., Cerantola V., Bykov M., Bykova E., Kichanov S.E., Lukin E.V., Savenko B.N., Ponomareva A.V., Abrikosov I.A (2017) Magnetic and structural properties of $FeCO_3$ at high pressures. Phys. Rev. B, 96, 134405.

16. Mozafari E., Alling B., Steneteg P., Abrikosov I. (2015) Role of N defects in paramagnetic CrN at finite temperatures from first principles. Phys. Rev. B, 91, 094101.

17. Shulumba N., Raza Z., Hellman O., Janzén E., Abrikosov I.A., Odén, M. (2016) Impact of anharmonic effects on the phase stability, transport and electronic properties of AlN. Phys. Rev. B, 94, 104305.

18. Bykova E., Bykov M., Černok A., Tidholm J., Simak S.I., Hellman O., Belov M.P., Abrikosov I.A., Liermann H.-P., Hanfland M., Prakapenka V.B., Prescher C., Dubrovinskaia N., Dubrovinsky L. (2018) Metastable silica high pressure polymorphs as structural proxies of deep Earth silicate melts. Nature Commun., 9, 4789.

19. Hallstedt B., Khvan A.V., Lindahl B.B., Selleby M., Liu S. (2017) PrecHiMn-4—A thermodynamic database for high-Mn steels. Calphad, 56, 49-57.

20. Jacob A., Schmetterer C., Khvan A.V., Kondratiev A., Ivanov D., Hallstedt B. (2016) Liquidus Projection and thermodynamic modelling of the Cr-Fe-Nb ternary system. Calphad; 54, 1-15.

21. Dinsdale A.T., Khvan A.V., Watson A. (2014) Critical assessment 5: Thermodynamic data for vacancies. Mat Science and Technology (United Kingdom), 30, 14, 1715-1718.

22. Khvan A.V., Dinsdale A.T., Uspenskaya I.A., Zhilin M., Babkina T., Phiri A.M. (2018) A thermodynamic description of data for pure Pb from 0 K using the expanded Einstein model for the solid and the two state model for the liquid phase. Calphad, 60, 44-55.

23. Tang F., Bogdanovsk D., Bajenova I., Khvan A., Dronskowski R., Hallstedt B. (2018) A CALPHAD assessment of the Al–Mn–C system supported by ab initio Calculations. Calphad, 60, 231-239.

24. Fartushna I., Bajenova I., Khvan A., Cheverikin V., Ivanov D.O., Shilundeni S., Alpatov A., Sachin K., Hallstedt B. (2018) Experimental investigation of solidification and isothermal sections at 1000 and 1100 °C in the Al-Fe-Mn-C system with special attention to the kappa-phase. Journal of Alloys and Compounds, 735, 1211-1218.

25. Dinsdale A.T., Akhmetova A.M., Khvan A.V., Aristova N.M. (2015) A critical assessment of thermodynamic and phase diagram data for the Ge-O system. J Phase Equil. Diffusion, 36, 3, 254-261.

26. Povarnitsyn M.E., Itina T.E., Levashov P.R., Khishchenko K.V. (2013) Mechanisms of nanoparticle formation by ultra-short laser ablation of metals in liquid environment. Phys. Chem. Chem. Phys., 15, 3108-3114.

27. Povarnitsyn, M.E., Andreev, N.E., Levashov, P.R., Khishchenko, K.V., Kim, D.A., Novikov, V.G., Rosmej, O.N. (2013) Laser irradiation of thin films: effect of energy transformation. Las. Part. Beams., 31, 663-671.

28. Filinov V.S., Ivanov Yu.B., Fortov V.E., Bonitz M., Levashov P.R. (2013) Color path-integral Monte-Carlo simulations of quark-gluon plasma: Thermodynamic and transport properties. Phys. Rev. C., 87, 035207;

29. Sin'ko G.V., Smirnov N.A., Ovechkin A.A., Levashov P.R., Khishchenko K.V. (2013) Thermodynamic functions of the heated electron subsystem in the field of cold nuclei. High Energy Density Physics, 9, 309.

30. Minakov D.V., Levashov P.R., Khishchenko K.V., Fortov V.E. (2014) Quantum molecular dynamics simulation of shock-wave experiments in aluminum. J. Appl. Phys., 115, 223512.

31. Dyachkov S.A., Levashov P.R. (2014) Region of validity of the finite-temperature Thomas-Fermi model with respect to quantum and exchange corrections. Phys. Plasmas, 21, 052702.

32. Knyazev D.V., Levashov P.R. (2014) Transport and optical properties of warm dense aluminum in the two-temperature regime: Ab initio calculation and semiempirical approximation. Phys. Plasmas, 21, 073302.

33. Krasnova P.A., Levashov P.R. (2015) Two-phase isochoric Stefan problem for ultrafast processes. Int. J. Heat and Mass Transfer, 83, 311-316.

34. Povarnitsyn M.E., Fokin V.B., Levashov P.R., Itina T.E. (2015) Molecular dynamics simulation of subpicosecond double-pulse laser ablation of metals. Phys. Rev. B, 92, 174104.

35. Minakov D.V., Levashov P.R. (2015) Melting curves of metals with excited electrons in the quasiharmonic approximation. Phys. Rev. B, 92, 224102.

36. Minakov D.V., Levashov P.R. (2016) Thermodynamic properties of LiD under compression with different pseudopotentials for lithium. Comp. Mat. Sci., 114, 128-134.

37. Gnyusov S.F., Rotshtein V.P., Mayer A.E., Rostov V.V., Gunin A.V., Khishchenko K.V., Levashov P.R. (2016) Simulation and experimental investigation of the spall fracture of 304L stainless steel irradiated by a nanosecond relativistic high-current electron beam. Int. J. Fracture, 199, 59-70.

38. Dyachkov S.A., Levashov P.R., Minakov D.V. (2016) Region of validity of the Thomas-Fermi model with corrections. Phys. Plasmas, 23, 112705.

39. Minakov D.V., Levashov P.R., Fokin V.B. (2017) Vibrational spectrum and entropy in simulation of melting. Comp. Mat. Sci., 127, 42-47.

40. Fokin V.B., Povarnitsyn M.E., Levashov P.R. (2017) Simulation of ablation and plume dynamics under femtosecond double-pulse laser irradiation of aluminum: Comparison of atomistic and continual approaches. Appl. Surf. Sci., 396, 1802-1807.

41. Dozhdikov V.S., Basharin A.Yu., Levashov P.R., Minakov D.V. (2017) Atomistic simulations of the equation of state and hybridization of liquid carbon at a temperature of 6000 K in the pressure range of 1–25 GPa. J. Chem. Phys., 147, 214302.

42. Minakov D.V., Paramonov M.A., Levashov P.R. (2018) Consistent interpretation of experimental data for expanded liquid tungsten near the liquid-gas coexistence curve. Phys. Rev. B, 97, 024205.

43. Povarnitsyn M.E., Levashov P.R., Knyazev D.V. (2018) Simulation of ultrafast bursts of subpicosecond pulses: in pursuit of efficiency. Appl. Phys. Lett., 112, 051603.

44. Alexandrov A.A., Orlov V.F. (2017) Thermophysical properties of working substances of heat power engineering. 2nd ed., Rev. and additional. Moscow: publishing house MEI.

45. Aleksandrov A.A., Orlov K.A., Ochkov V.F. (2009) Thermophysical properties of working substances of heat power engineering: an Internet Handbook. Moscow: publishing house MEI.

46. Ochkov V.F., Orlov K.A., Alexandrov A.A., Bochkov A.V. (2015) Properties of water and water vapor: network, open, interactive IT-resources. Teploenergetika, 5, 71-80.

47. Ochkov V.F., Ustyuzhanin E.E., Zhuo K.K., Shishakov V.V. (2015) Thermophysical databases: from the table to interactive Internet resources and "cloud" templates. Thermophysics of high temperatures, 53, 4, 544-550.

48. Ochkov V.F., Orlov K.A., Zhuo K.K. (2014) Cloud" functions and templates engineering calculations for nuclear power plants. Thermal Engineering, 10, 68-72.

49. Muhamedov B., Saenko I., Ponomareva, A.V., Kriegel M.J., Chugreev A., Udovsky A., Fabrichnaya O., Abrikosov, I.A. (2019) Thermodynamic and physical properties of Zr3Fe and ZrFe2 intermetallic compounds. Intermetallics, 109, 189-196.

50. Feynman R., Metropolis N., Teller E. (1949) Equations of state of elements based on the generalized Fermi-Thomas theory. Phys.Rev., 75, 1561.

IRSTI 29.27.07 https://doi.org/10.26577/phst-2019-2-p2

Simulation of Coulomb particles collisions and calculation of Lyapunov exponent for bound orbits

K.M. Turekhanova* and A.M. Murat

Institute of Experimental and Theoretical Physics, Al-Farabi Kazakh National University, 71, al-Farabi Ave, 050040, Almaty, Kazakhstan
**e-mail: kunduz@physics.kz*

The computer simulation from the first principles allows us to obtain results for systems consisting of many particles and interacting according to the Coulomb law (plasma, star clusters and astrophysical objects). In this work, the methodology of simulation for Coulomb systems is investigated. The influence of rounding errors, integration errors of reversible Newton equations is studied on the characteristics of Coulomb collisions on the basis of the consideration of several model problems. The trajectories of two particles attracted to the positively charged force center are got for various initial coordinates and velocities and also their energetic natures are researched. It is shown that the symmetries are broken and the particle paths are destroyed due to rounding errors and calculation errors. The degree of deviation from symmetry is described by the value of the Lyapunov exponent, which characterizes the chaos and turbulence in plasmas for the system. The results can be also extended to the system of gravitating masses.

Key words: Molecular Dynamics, Coulomb system, elementary processes, Lyapunov exponent, bound orbit, numerical simulation
PACS numbers: 52.20.-j, 52.20.Fs

1 Introduction

The physics of elementary processes in dense plasma is one of the fundamental directions in modern physics, v of such system's properties is of considerable interest in connection with the study of natural plasma phenomena occurring in astrophysical objects, the creation of the scientific foundations of new plasma technologies and the solution of the problem of controlled thermonuclear fusion. There are some problems associated with the lack of adequate theoretical models for some plasma phenomena and the multiparameter nature of such systems. In the experimental study of the properties of such plasmas, In such situations, the problem is partially solved by using modern methods of computer modeling of physical systems [1-7]. The main properties of the classical Coulomb plasma were studied by the method of the dynamics of many particles for determination of the thermodynamic characteristics, the distributed microfields, shielding and etc. [8-12]. In this paper we have used numerical simulation methods for describing of the collisions of Coulomb particles and for estimation of Lyapunov exponent, which characterizes the chaos and turbulence in plasmas. Relaxation of kinetic energy to equilibrium state was studied by molecular dynamic method for non-equilibrium strongly coupled plasmas [13], where the concept of dynamical memory time t_m was discussed. The fluctuation of energy ΔE and K-entropy was treated. The Lyapunov exponent in the phase space for ion one-component plasmas with the use of the three-dimensional SCOPE had been evaluated in [9]. The parameter describing chaotic treatment of system was got as a function of the time integral of the correlation function for the second derivative of the interparticle potential, that establishes a link between the Lyapunov exponent and the transport coefficients [14]. There were developed an analytical model for the largest Lyapunov exponent in dilute plasma. The model showed that it related to the dielectric response function [15]. The effect of inevitable experimental noise had been investigated and its full spectrum has been achieved to confirm transition from quasiperiodicity to chaos in plasma [16-18].

2 The simulation method

The idea of particle method is the numerically solving the motion equations of (Newton's equations) for a system of particles interacting with each other and with the walls. The particle method is based on the ideology of modeling from the first principles (*ab initio*) [19].

The problem of the occurrence of chaos in dynamical systems also attracts attention in connection with the transition from reversible equations of dynamics to irreversible kinetic equations. The computer simulation from the first principles allows us to obtain results for systems consisting of many particles and interacting according to the Coulomb law (plasma, star clusters). Instability of trajectories, irreversibility of the numerical solutions, mixing of the phase volume in Hamiltonian systems led to a slowdown in recombination in a system of a limited number of particles.

The present work is devoted to the research of the divergence rate of initially close phase trajectories of the classical Coulomb system. In our opinion, the particle method is very fruitful in studying the fundamental properties of a system of many particles. The simulation from the first principles gives the possibility to study the occurrence of chaos in nonlinear dynamical systems. The progress in the study of dynamic chaos based on the Kolmogorov-Arnold-Moser theorem (KAM theory) for the Coulomb system of particles has limited applicability due to the non-integrability of the system [20-22]. In the present work the rate of initially close phase trajectories in the system the plasma non-ideality index, and the calculation accuracy are investigated on the basis of numerical simulation and analytical estimates. For criterion for the similarity characteristics of equilibrium plasma is used the Lyapunov exponent [23-25].

On the calculation of the divergence rate of initially close phase trajectories we use the Lyapunov exponent, which is the most important quantitative characteristic of Hamiltonian and dissipative systems. The Lyapunov exponents determine the measure of stochasticity of Hamiltonian systems [26, 27]. The maximum of them σ_1 is widely used as a criterion for stochasticity [16].

Let the dynamics of a system consisting of 2n particles is determined by the equations:

$$\frac{dx_k}{dt} = V_k\left(x\right), \quad k = 1,2,...,12n$$

The difference between the vectors of two phase trajectories clossing to the initial moment is $\Delta x = x_2\left(t\right) - x_1\left(t\right)$, that can be determined from the linearized equation

$$\frac{d\Delta x}{dt} = G\Delta x, \; G = \frac{dV}{dx}$$

where G is the Jacobian matrix. The average speed of the exponential divergence of the initial close phase trajectories is determined as follows [16, 17]:

$$\sigma_1 = \lim \frac{1}{t} \ln \frac{d\left(t\right)}{d\left(0\right)} \tag{1}$$

$$\text{at } t \to \infty \text{ and } d\left(0\right) \to 0$$

where $d\left(t\right) = \left|x_1\left(t\right) - x_2\left(t\right)\right| = d\left(0\right)\exp\left(\sigma_1 t\right)$ is the distance between close phase trajectories at the initial time $t = 0$. The solution of the linear equation for Δx can be written as:

$$\Delta x = T\left(t\right)\Delta x\left(0\right), \quad T\left(t\right) = \exp\left[\int_0^t G\left(x\left(\tau\right)d\tau\right)\right]$$

expanding for small times τ the matrix exponential $T(\tau)$ in a series we get for eigenvalues of the transition matrix $1 + \tau\lambda_i$, where λ_i is eigenvalues of the Jacobian matrix. For a linear system, the maximum eigenvalue λ_i of the Jacobian matrix determines the rate of exponential recession of the trajectories $\sigma_1 = \lambda_1$. In this case, the path divergence vector becomes collinear to the corresponding eigenvector.

The similarity criterion is the non-ideality parameter $\Gamma = e^2 / \left(r_i T_e\right)$, where $r_i = \left(3/4\pi N_i\right)^{1/3}$ is radius of sphere with volume per particle, that follows from the dimension theory for the Coulomb system, where the radius of the sphere with volume per one ion. Therefore, for an equilibrium system with a Maxwellian distribution of particles over velocities, the Lyapunov exponent of particles' system can be represented in the form of

$\sigma_1 = t_c \sigma_1^0 \left(N_p, \Gamma \right)$ where $\sigma_1^0 \left(N_p, \Gamma \right)$ is the dimensionless Lyapunov exponent, t_c is the characteristic time.

A rough estimate of the Lyapunov exponent for plasma can be obtained from an analogy with the known value of the Lyapunov exponent for rigid spheres with Maxwellian distribution [18]:

$$\sigma_1 \approx \frac{V_0}{l} \ln\left(1 + \frac{l}{2R}\right) = \frac{3\upsilon_T R^2}{\pi^{1/2} r_i^3} \ln\left(1 + \frac{2r_i^3}{3R^3}\right) \qquad (2)$$

where $l = 1/\pi R^2 N$ is the mean free length, $V_0 = 4\upsilon_T / \pi^{1/2}$ is the average relative particle velocity, R is the radius of hard spheres, N is their density. The expression (2) determines the increase in the distance between initially close points of the phase trajectories in the form:

$$d(t) = d(0)\left[1 + l/2R\right]^{V_0 t/l}$$

Each collision of particles leads to an increase in the distance between phase trajectories by factor of $1 + l/(2R)$.

3 The results and discussions

In presented paper we consider several elementary problems on which there are demonstrated some features of simulation methods of Coulomb collisions. Moreover we acknowledge the effect of calculation errors on the physical result, rounding errors, irreversibility of difference schemes, and to methods for estimating the exponential spread of initially close phase trajectories.

For clarity of presentation we study the dynamics of two particles moving in the same plane in the vicinity of an infinitely heavy (motionless) power center. For convenience there are used the dimensionless units in which the charge and mass of the moving particles are equal to unity.

We consider four formulations of the problems of the motion of two particles in the field of a force center attracting them.

1) The trajectories of two particles attracted to the positively charged force center are showed in figure 1, they repel each other. The initial position of the first particle is a circular orbit of radius 0.05. The second another particle flies to the first particle from far to the right with an impact parameter of 0.04 on speed 1. The total energy of the first particle is negative, it is in finite orbit, the total energy of the second particle is positive and it is free, but the full energy of whole system is negative.

The figure obviously shows the physics of the polarization interaction of an electron with a monovalent atom: an electron swooping on an atom polarizes it, an electron begins to be attracted to the induced dipole, then as a result of a close collision it passes to a bound orbit and the first electron becomes free. In this case, the total energy of a free electron after collision increases, i.e. appropriately there is occurred that a bound electron sinks deeper into a potential well. A more detailed study of this process with the calculation of all average characteristics, in particular, the diffusion coefficient of bound electron along the energy axis will be presented in a separate work.

2) The trajectories of two particles, attracted to a positively charged force center are showed in figures 2-4, they repeal each other and their energy characteristics are given in figures 5-8. The initial position of the first particle is the same as in the first problem, but the second is located symmetrically with respect to the center at the same speed. In this formulation, the particles have move along elliptical trajectories symmetrically with respect to the force center.

There are followed the breaking of symmetry and the particle paths are destroyed due to rounding errors and calculation errors. The degree of deviation from symmetry is characterized by the value of the Lyapunov exponent for this system.

3) In figures 9-11 there are demonstrated the trajectories of the same as in the previous problem of the symmetric system, but the particles move in elliptical orbits. The time dependence of the absolute value of the difference in kinetic energy of two charged particles is presented in figures 12, 13 for this system, where they move around the center of force with initial coordinates and velocities.

In this case, the difference in the kinetic energies of the initially symmetric system is determined by the spreading rate of initially close phase trajectories. In this formulation the initial deviation is not specified, but it is obtained as a result of the accumulation of rounding errors over time period in order of 10. Further the divergence of the trajectories (energies) is characterized by exponential growth. The indicator of this growth is the Lyapunov exponent (the slope of the straight line in the semi-logarithmic scale is in figure 13).

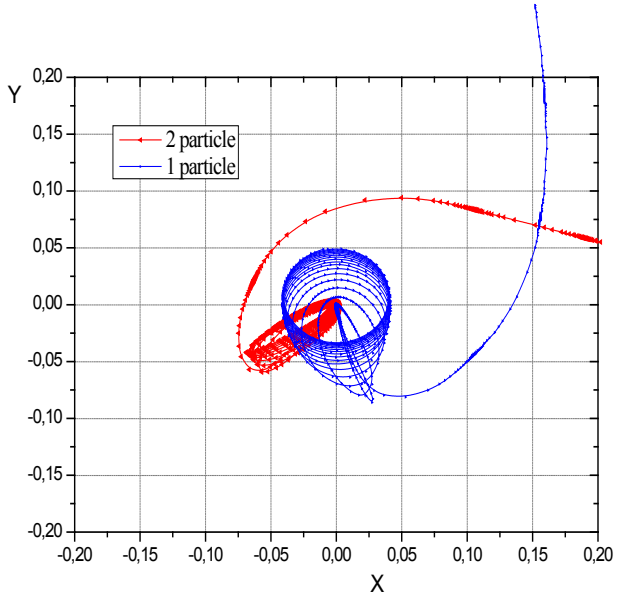

Figure 1 – The trajectory of two charged particles around a force center with initial coordinates and velocities:
P1(0, 0.05, 0) ; V1(-4, 0, 0) and
P2(1, 0.04, 0) ; V2(-1, 0, 0)

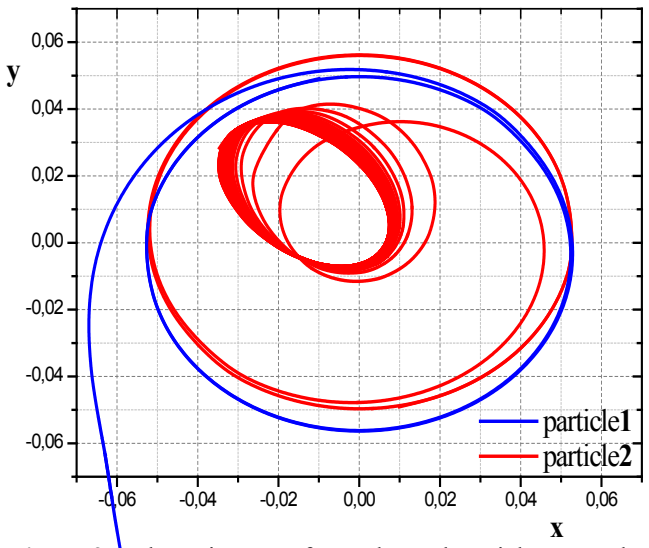

Figure 2 – The trajectory of two charged particles around a force center with initial coordinates and velocities:
P1(0, 0.05, 0) ; V1(-4, 0, 0);
P2(0, -0.05, 0) ; V2(4, 0, 0)

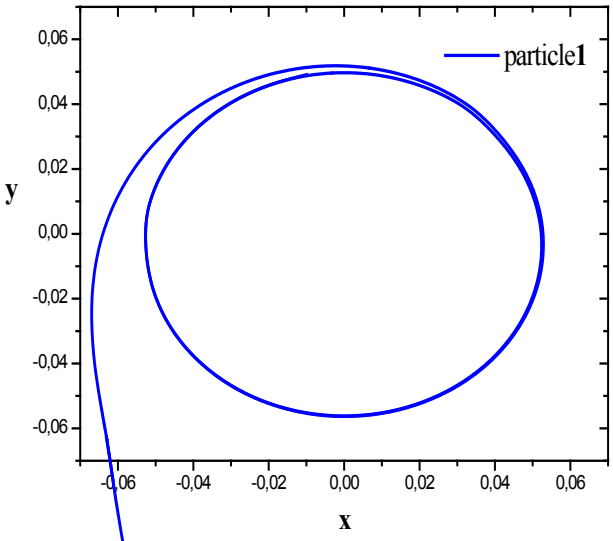

Figure 3 – The trajectory of charged particle around a force center with initial coordinate and velocity:
P1(0, 0.05, 0) ; V1(-4, 0, 0)

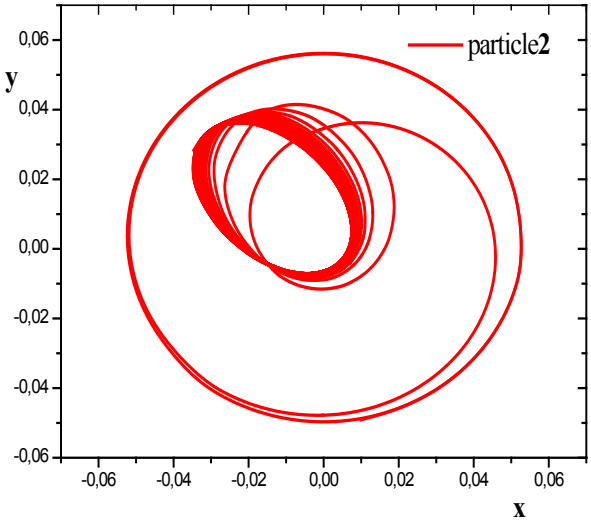

Figure 4 – The trajectory of charged particle around a force center with initial coordinate and velocity:
P2(0, -0.05, 0) ; V2(4, 0, 0)

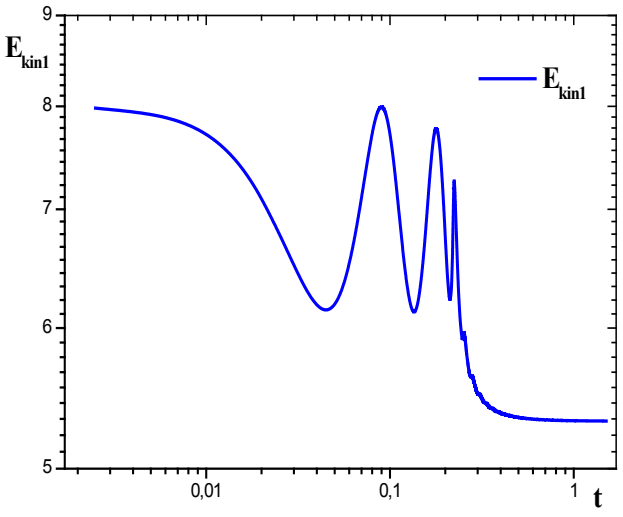

Figure 5 – The kinetic energy of charged particle around a force center with initial coordinate and velocity: P1(0, 0.05, 0) ; V1(-4, 0, 0)

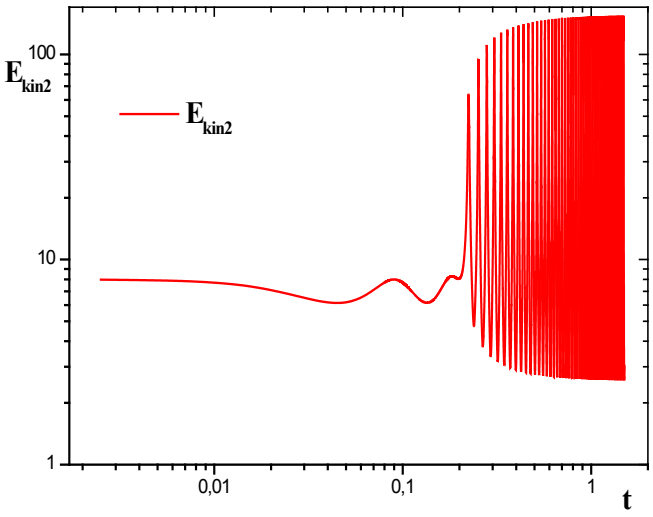

Figure 6 – The kinetic energy of charged particle around a force center with initial coordinate and velocity: P2(0, -0.05, 0) ; V2(4, 0, 0)

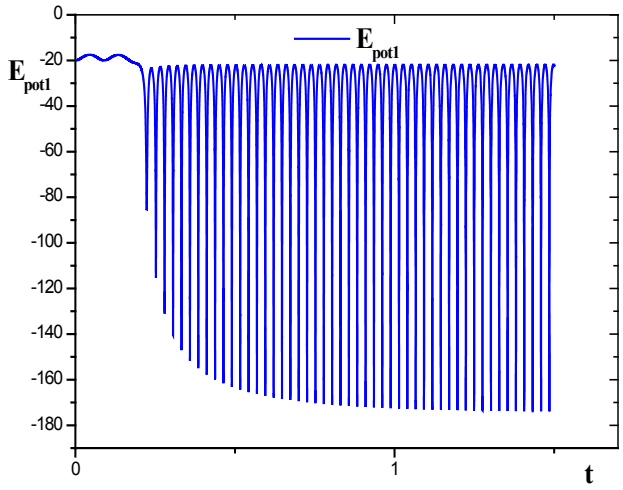

Figure 7 – The potential energy of charged particle around a force center with initial coordinate and velocity: P1(0, 0.05, 0) ; V1(-4, 0, 0)

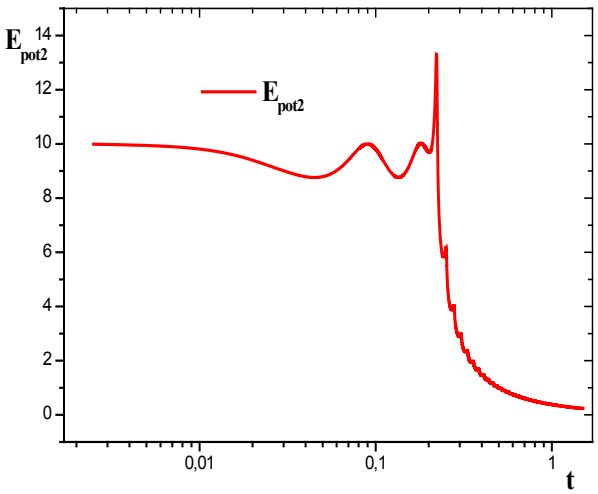

Figure 8 – The potential energy of charged particle around a force center with initial coordinate and velocity: P2(0, -0.05, 0) ; V2(4, 0, 0)

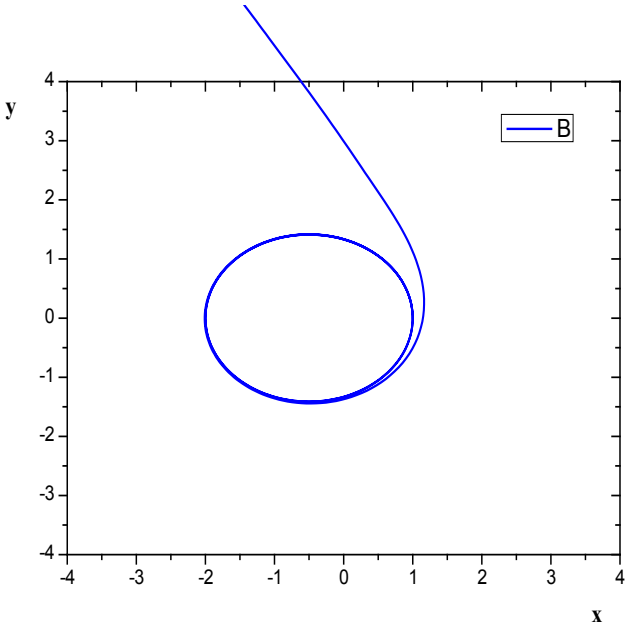

Figure 9 – The trajectory of charged particle around a force center with initial coordinate and velocity: P1(1, 0, 0) ; V1(0, 1, 0)

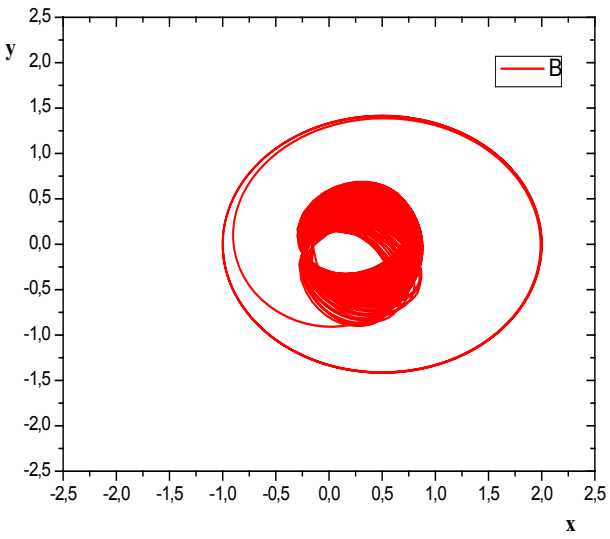

Figure 10 – The trajectory of charged particle around a force center with initial coordinate and velocity: P2(-1, 0, 0) ; V2(0, -1, 0)

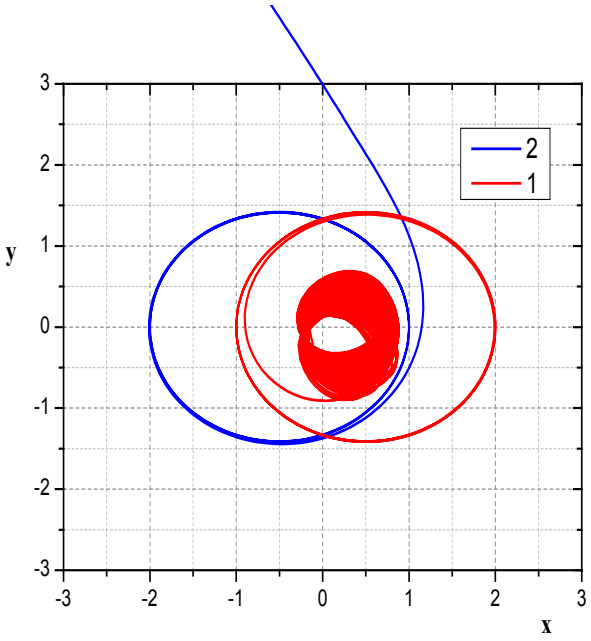

Figure 11 – The trajectory of two charged particles around a force center with initial coordinates and velocities: P1(1, 0, 0) ; V1(0, 1, 0) and P2(-1, 0, 0) ; V2(0, -1, 0)

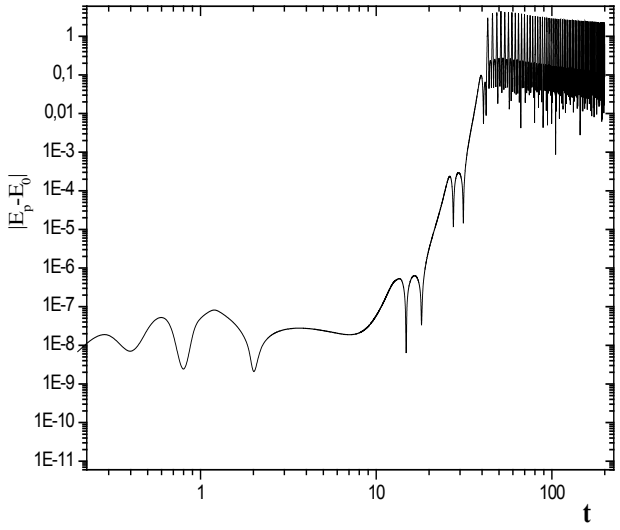

Figure 12 – The time dependence of absolute value of the kinetic energy difference of two charged particles which move around a force center with initial coordinates and velocities:
P1(1, 0, 0) ; V1(0, 1, 0) and P2(-1, 0, 0) ; V2(0, -1, 0)

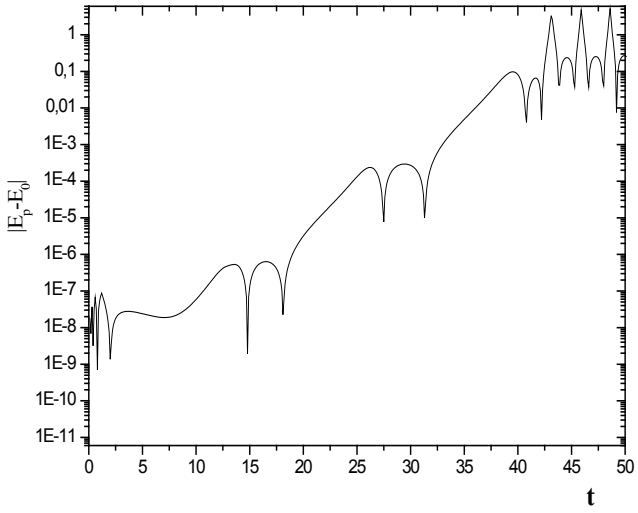

Figure 13 – The time dependence of absolute value of the kinetic energy difference of two charged particles which move around a force center with initial coordinates and velocities:
P1(1, 0, 0) ; V1(0, 1, 0) and P2(-1, 0, 0) ; V2(0, -1, 0)

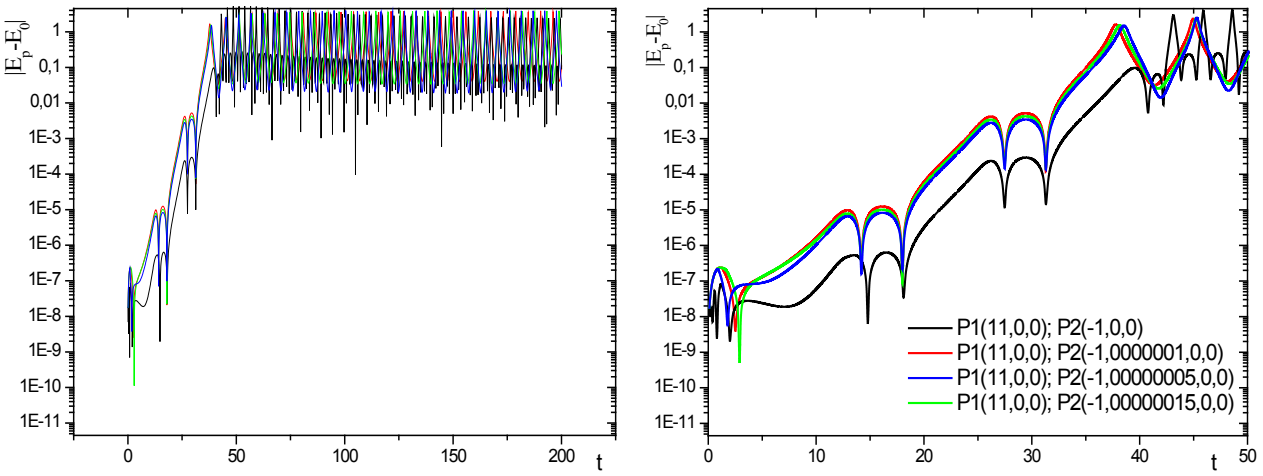

Figure 14 – The absolute value of the change in the difference of kinetic energies of two charged particles around a force center with initial velocities V1(0, 1, 0) и V2(0, -1, 0) and with different initial coordinates at the initial time
_____ P1(11,0,0); P2(-1,0,0)
_____ P1(11,0,0); P2(-1,0000001,0,0)
_____ P1(11,0,0); P2(-1,00000005,0,0)
_____ P1(11,0,0); P2(-1,00000015,0,0)

4) The similar time-dependent dependences of the absolute value of the kinetic energy difference of two charged particles is showed in figure 14, they move around the center of force with initial coordinates and velocities. But in this case the difference is that the total energies is defined by a bit initial deviation of fluctuation of the second particle's coordinate. In such setting, the further divergence of the trajectories (energies) is also characterized by exponential growth. The indicator of this growth is the Lyapunov exponent (slope of a straight line in a semi-logarithmic scale is in the figure 14).

3 Conclusions

In this work the methodology of simulation for Coulomb systems is investigated. The influence of rounding errors, integration errors of reversible Newton equations is investigated on the characteristics of Coulomb collisions on the basis of the consideration of several model problems. The get results can be also extended to the system of gravitating masses. An estimate of the Lyapunov exponent for system of classical Coulomb particles on dependence of particle's number in the system, the nonideality degree of plasma and the accuracy of integration of Newton's equations can be useful for analyzing the results of modeling systems with a large number of particles. The main attention is paid to the case of the interaction of free and bound particles, which is especially important at consideration of strongly non-ideal systems.

Acknowledgment: The authors would like to thank prof. S.A. Maiorov for helpful discussion. This work was partially supported by the RFBR grant No. 19-08-00611a.

References

1. Pierleoni C., Margo W.R., Ceperley D.M., & Bernu B. (1996). Path integral MonteCarlo simulation of hydrogen plasma. In W.D. Kraeft, M. Shlanges (Eds.) . Physics of Strongly Coupled Plasma . London: World Scientific NJ. 11–26.
2. Morozov I.V., Norman G.E., & Valuev A.A.. (2001). Stochastic properties of strongly coupled plasmas. Phys. Rev. E., 63, 36405.
3. Bezkrovniy V., Filinov V.S., Kremp D., Bonitz M., Schlanges M., Kraeft W.D., Levashov P.R., & Fortov V.E. (2004). Monte-Carlo results for the hydrogen Hugoniot . Phys. Rev. E, 70, 057401
4. Baimbetov F.B., Ramazanov T.S., Dzhumagulova K.N., Kadyrsizov E.R., Petrov O.F., & Gavrikov A.V. (2006). Modelling of dusty plasma properties by computer simulation methods. J.Phys.A: Math. And Genю, 39, 4521–4525.
5. Donkó Z. (2009) . Molecular dynamics simulations of strongly coupled plasmas. J. Phys. A: Math. Theor, 42, 213029.
6. Ignatov A.M. (2017). Brownian motion of a plasma crystal . Plasma Physics Reports, 43, 659–667.
7. Chap A.M., & Sedwick J.R.. (2017). Coulomb collision model for use in nonthermal plasma simulation. Phys. Rev. E, 95, 063209
8. Maiorov S.A., Tkachev A.N., & Yakovlenko S.I. (1994). Metastable supercooled plasma. Physics-Uspekhi, 37(3), 279-288.
9. Maiorov S.A., Tkachev A.N., & Yakovlenko S.I. (1995). Metastable state of supercooled plasma. Physics Scripta, 51, 498.
10. Bobrov A.A., Bronin S.Ya., Zelener B.B., Zelener B.V., Manykin E.A., & Khikhlukha D.R. (2011). Collision recombination coefficient in ultracold plasma. Molecular Dynamics Calculation. JETP, 139, 605.
11. Lankin A.V., & Norman G.E.. (2009). Collisional recombination in strongly coupled plasma. J. Phys. A, 42, 214032.
12. Bannasch G., & Pohl T. (2011). Rydberg atom formation in strongly correlated ultracold plasmas. Phys. Rev.A, 84, 052710.
13. Furukawa H., & Nishihara K. (1990). Reduction in bremsstrahlung emission from hot, dense binary-ionic-mixture plasmas. Phys.Rev. A , 42, 3532.
14. Barnett D.M., Tajima T., Nishihara, Ueshima Y., & Furukawa H. (1996). Lyapunov Exponent of a Many Body System and Its Transport Coefficients. Physical Review Letters, 76, 1812.
15. Nishihara K. & Ueshima Y. (1999). Lyapunov exponent of dilute gas, liquid and solid plasmas. *Plasma Phys. Control. Fusion* , 41, A257.
16. Huang W., Ding W. X., Feng D. L., & Yu C. X. (1994). Estimation of a Lyapunov-exponent soectrum of plasma chaos. Phys. Rev. E, 50.

17. Ueshima Y., Nishihara K., Barnett D.M., Tajima T., & Furukawa H. (1997). Particle simulation of Lyapunov exponents in one-component strongly coupled plasmas . Phys. Rev. E, 55, 3439.
18. Pyragas K. (1997). Conditional Lyapunov exponents from time series. Phys. Rev. E, 56, 5183.
19. Hockney, J. R. (1981). Eastwood Computer Simulation Using Particles, New York : McGraw-Hill.
20. Lichtenberg A. J. & Lieberman M. A. (1992). Regular and Stochastic Motion. Springer .
21. Mayer J. & Goeppert-Mayer M. (1977). Statistical Mechanics. New York: Wiley. 540.
22. Schuster H.G. (1984). Deterministic Chaos. Weinheim: Physik-Verlag.
23. Ebeling W., Kreft W., & Kremp D. (1977). Theory of Bound States and Ionization Equilibrium in Plasma and Solids. Berlin: Academie-Verlag.
24. Maiorov S.A. (1999). Divergence of the phase trajectories of a Coulomb system. Bulletin of the Lebedev Physics Institute, 1, 25.
25. Eggleston. D.L. (2018). Application of chaos theory to the particle dynamics of asymmetry-induced transport. Physics of Plasmas, 25, 032305.
26. Zaslavsky G.M. (1984). *Chaos in Dynamical Systems*. Moscow: Nauka.
27. Hoover W.G., & Hoover C.G. (2012). Time Reversibility, Computer Simulation, Algorithms, Chaos (2nd ed) . World Scientific Publishing Company.

IRSTI 41.21.05; 41.21.19 https://doi.org/10.26577/phst-2019-2-p3

A new Java-based application in solar physics

A. Sarsembayeva [1,*], F. Belisarova [1], M. Odsuren[2] and A. Sarsembay[3]

[1]*Department of Physics and Technology, Al-Farabi Kazakh National University, 71, al-Farabi Ave., 050040, Almaty, Kazakhstan*
[2]*School of Engineering and Applied Sciences, National University of Mongolia, Ikh surguuliin gudamj 3, 14201, Ulaanbaatar, Mongolia*
[3]*School-Lyceum №250 named after T.Komekbayev, 19A, Balky bazar Str., 120500, Karmakchi, Kyzylorda, Kazakhstan*
*e-mail: *sarsembaeva.a@kaznu.kz*

Solar-based flares are one of the most impressive energetic events in the solar atmosphere. Given their part of job in the solar corona's energy balance and their function playing important role in the space weather, numerous observations researched the release of energy and induction of solar flares, focusing on the solar active. National solar observatories are providing the overall network with a wealth of data, covering extensive time ranges (e.g. Solar and Heliospheric Observatory, SOHO), numerous perspectives (Solar Terrestrial Relations Observatory, STEREO), and returning a lot of information (Solar Dynamics Observatory, SDO). Specifically, the huge amount of SDO data are accessible only from a few repositories, such type of data as a full-cadence data or full-disk of scientific concern are hard to download, because of their size. To address these difficulties we have begun to build up a new solar application using the Java programming language for a stand-alone application type (GUI).

Key words: temperature, EM, reconnection rate, Java.
PACS number(s): 96.60.−j; 96.60.Iv; 96.60.qe

1. Introduction

Solar flares are powerful explosions of radiation, while coronal mass ejections are enormous clouds of solar material and magnetic fields that eject from the Sun at high speeds. Damaging emission from a solar flare cannot go through the atmosphere of the Earth and affect physically humans, but when they are sufficiently enough they can disturb the Earth's atmosphere in the layer where GPS and communications signals travel [1].

Solar burst, on the other way, directly influence to the Earth's ionosphere and radio communications on the ground, and furthermore spread of energetic particles into space. Hense, for comprehension and prediction of space weather and the solar flares impact on the Earth, a comprehension of coronal mass ejections and solar flares is required.

Solar and stellar flares have been studied using both ground and space-based investigation [2-3]. Currently, using *GOES* and soft X-ray data of *Yohkoh* Bragg crystal spectrometer, by [4] proposed between's the peak temperature of solar flares and their volume emission measure a exceptional correlation, where n is the electron number density and V is the volume. Shimizu [5] found a comparative connection in microflares observed by the *Yohkoh* soft X-ray telescope. Feldman, Laming, & Doschek [4] show that this relationship can also be effectively extrapolated to the instanse of stellar X-ray flares.

Figure 1 shows the observed emission measure and temperature relationship, based on solar flare data by Feldman et al. ([4]; higher hatched area), solar microflare data by Shimizu ([5]; lower hatched area), and four stellar flares by [4] (asterisks). All of the four stellar flares appear to lie on the correlation between's flare temperature and emission measure, including solar micro flares as well as stellar flares [6].

Figure 1 shows the observed ratio between the solar and stellar flares emission measure and as well as their temperatures. The emission measure and temperature's correlation given by the equation (1) is plotted as solid lines with the values of magnetic field strength B = 15, 50, 150G in the case of $n_0 = 10^9$ cm^{-3}. Figure 1 illustrates that the observed ratio line coincide to the magnetic field

strength's line with the 30-150G and for solar and stellar flares coronal magnetic field strength is evaluated to be about 40-300G. In addition, we can plot the relation between the emission measure and temperature for constant solar flare loop length from the equations (1) and (2) if we exclude the magnetic field strength, which is additionally in Figure 1 appeared in as dash-dotted lines. It is known that the characteristic size of a solar micro flaring loop is 10^8 – 10^9 cm and the characteristic size of a solar flaring loop is about 10^9 – 10^{10} cm. These values completely reliable with observations [6].

The primary reason for developed Java-based solar application is to accommodate solar activity near real-time information and definition of the solar parameters. This Java application open to a wide range of users. Cross-platform application was created by following 3 standards: intuitive, simplicity and user-friendliness. The combination of these 3 standards contributes to improving the usability.

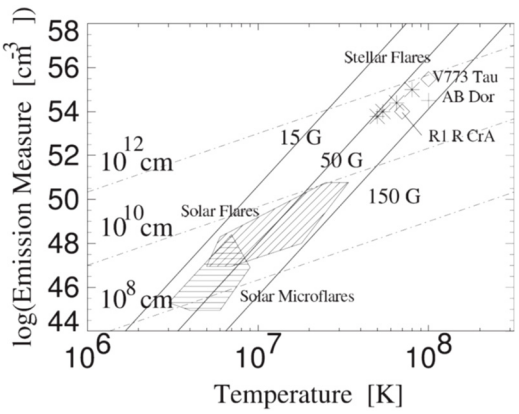

Figure 1 – The solar and stellar flares temperature and emission measure correlation [7].

2. User interface and external tools

In order to establish an OS independent application, Java was selected as a programming language. Java is an OS independent platform and distributed free of charge. Graphical UIs simplify use of PCs by displaying data in a way that allows rapid assimilation and manipulation. The standards of UI design, for example, flexibility and efficiency are intended to improve the quality of UI design and structure. A good GUI configuration does not require to memorize the steps needed to perform an action for program users. Taking the aforementioned facts into account, a stand-alone type application is being developed. This application is entirely written using the Swing and SwingX library (Java programming language).

The objective of this work is to accomplish better system usability through design decisions personalized in the program architecture. Advanced features implemented in program can allow users to save their time. The efficiency of application directly depends from well-designed user-interface and its functionality. The implementation of such features over-simplifies the problem and provides little guidance for the user interface designer. Therefore usage of advanced components of Java gives great opportunity to users to achieve easiness and efficiency during the compilation time. Usability is critical for the success of program and should never be overlooked. Good usability can improve the performance of program.

Figure 2 shows the GUIs main window which is partitioned into four areas. At the top of the application located a menu bar which is used to perform basic and common operations. This includes the following menus: ‘File’, ‘Edit’. Between the menu bar and the content menu is a toolbar which provides three very frequently used controls: ‘OPEN’, ‘EDIT’, ‘COPY’, ‘PASTE’, ‘SAVE’, ‘SELECT’, ‘CLEAR’, and a comma-separated values file - ‘CSV’, which allows data to be saved in a tabular format and ‘GRAPH’ is a visual plotting of the relationship between variable quantities. The left panel is used to display content menu. Content menu consists ‘Temperature’, ‘Emission measure’, ‘Particle acceleration’, and ‘Energy release’ which contains two nodes ‘Sweet Parker model’, ‘Petschek model’.

Figure 3 illustrates the layout window of Temperature and Emission measure panel. All panels offers a list of panels to get an input text value.

The efficiency of stand-alone type application directly depends on well-designed content and its functionality. A new solar application was developed using Java language. The main motivation was the need for a platform-independent language, that could be accessible in various operation systems. The primary purpose of solar application is to provide advanced functionality for the users. A solar application was designed for both beginners and expert users to allow users to save their time by using advanced features of the program. During the development of new a solar application we followed 3 key principles:

- Intuitive (no need to invest time into learning):

✓ You shouldn't have to read a manual to become more productive;

✓ Clean and intuitive user-interface.

- Simplicity (the quality of being easy to understand):

✓ The Toolbar is the most important design element on an editor development because it is a singular tool that gives users a sense of orientation.

- User-friendliness (the quality of being functional):

✓ Collapsible/expandable item;

✓ Add/remove buttons;

✓ Filterable suggestion field;

✓ Dynamic suggestion field.

The advanced functionalities presently used to achieve the user-friendliness are briefly described below:

- Collapsible/expandable item

Collapsible/expandable function was implemented to simplify the tasks and decisions by creating a visual representation of a user interface. This function can reduce complexity for users.

- Add/remove buttons

Similar to the concept of collapsible/expandable items, the number of input areas must be minimum at first. These areas can be added/removed interactively by buttons.

- Filterable suggestion field

Filterable suggestion field aims to save users time and allows to users to avoid the mistakes.

- Dynamic suggestion field

The main function of a dynamic suggestion fields is to make data input easier and more reliable. For example, the user chooses an input from one list, which restricts the related contents of another list.

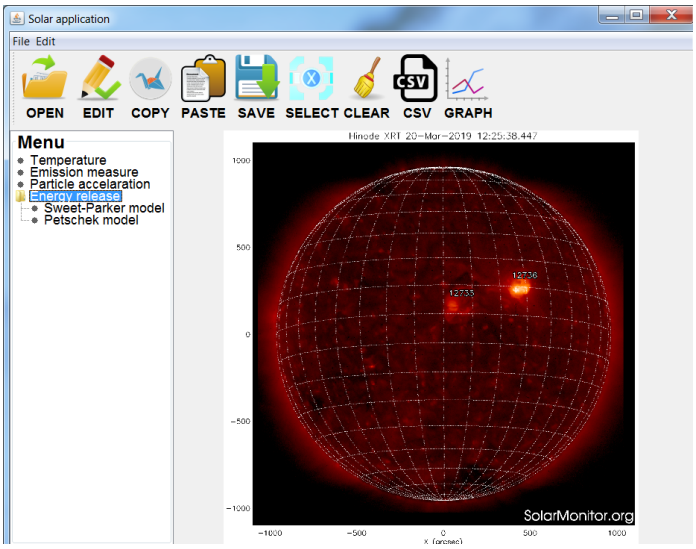

Figure 2 – The layout of main window of the Java application

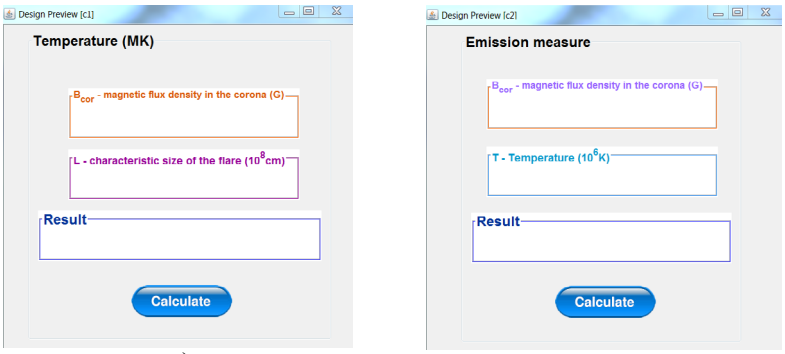

a) b)

Figure 3 – a) The layout of Temperature panel.
b) The layout of Emission measure panel.

Supported platforms: since Microsoft Windows operating systems are the most widely used computer platforms, execution of application on Microsoft Windows has been considered with a priority. The program has been tested on Windows XP, 7 and 10. Application execution on the GNU/Linux operating system has not been tested very often, but we confirmed it runs under Ubuntu 14.04.3 LTS. Application has not yet been tested on Mac OS.

3. Method

For quantitative physical comprehension of processes in the atmosphere of the Sun, the X-ray fluxes are in a limited of use. However, they affect the emission measure and temperature of the plasma that delivers the soft X-rays, and these physical quantities are vital: from them, the energetics of solar flares and other energy releases can be deduced.

[4] presented that there is a ratio between solar flare emission measure and temperature for solar flares as well as for some of stellar flares. [7] continued this ratio between emission measure and temperature and applied it for solar micro flares, T-Tauri star flares, and protostellar flares. It is outstanding that the relationship holds in a very wide range, 4×10^6 K < T < 10^8 K and 10^{45} cm^{-3} < EM < 10^{56} cm^{-3}. Shibata and Yokoyama [7] then could find that this universal correlation can be interpreted by the simple scaling law (see Figure 1),

$$EM \simeq 10^{48} cm^{-3} \left(\frac{B}{50\ G}\right)^{-5} \left(\frac{n_0}{10^9 cm^{-3}}\right)^{3/2} \left(\frac{T}{10^7 K}\right)^{17/2}, \quad (1)$$

The temperature were obtained in SunPY using the methods of White et al. [10-11] who used the CHIANTI atomic physics database to model the response of the ratio of the short (0.5-4 angstrom) to long (1-8 angstrom) channels of the XRSs onboard various GOES satellites [12].

Yokoyama & Shibata [8] performed magnetohydrodynamic numerical simulations of the reconnection, including both heat conduction and chromospheric evaporation and found a simple scaling relation:

$$T = 10^7 K \left(\frac{B}{50\ G}\right)^{6/7} \left(\frac{n_0}{10^9 cm^{-3}}\right)^{-1/7} \left(\frac{L}{10^9 K}\right)^{2/7}, \quad (2)$$

Evaluated convective electric field related to the magnetic reconnection rate, which conceivably during a solar flare takes a significant part in charged particle acceleration [6]:

$$E = 3 \times 10^3 \left(\frac{M_A}{0.1}\right) \left(\frac{B}{100\ G}\right)^2 \left(\frac{n_{jet}}{10^{10} cm^{-3}}\right)^{-\frac{1}{2}} Vm^{-1}. \quad (3)$$

The magnetic reconnection rate is commonly considered to play a key role in the build-up of energy in solar flares. The reconnection rate is an significant quantity, since it puts demanding constraints on the magnetic reconnection model. In spite of its significance, what defines the flares magnetic reconnection rate is still an open question. Sweet [13] and Parker's [14-15] steady reconnection model have a proposed reconnection rate value, which is equal to the $M_A = (\mathrm{Re}_m)^{-1/2}$, $\mathrm{Re}_m = (V_A L / \eta)$ is the magnetic Reynolds number characterized by the Alfven velocity and η is the magnetic diffusivity $\eta \sim 10^4 (\frac{T}{10^6 K})^{-3/2} cm^2 s^{-1}$. Petschek [16] identified that the previous model lacks the impacts of waves and proposed his model with $M_A \lesssim \pi / [8 \ln(8\,\mathrm{Re}_m)]$ [17-21].

4. Results

The length of a stellar flaring loop (10^{10} – 10^{12} cm) is much larger than the characteristic size of a solar flares. This value is reliable with observations at the surface of young stars is very strong that average field strength is order kilo Gauss [9].

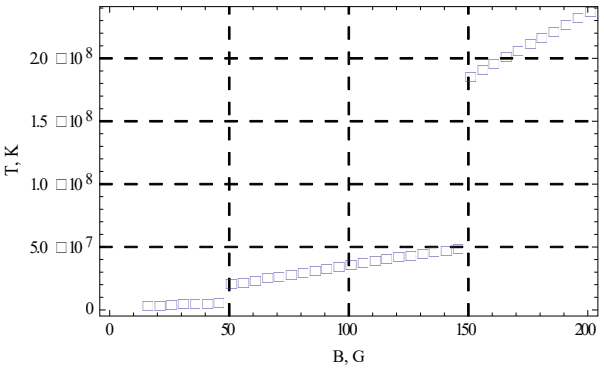

Figure 4 – The correlation between temperature and magnetic flux density of solar and stellar flares.

The motivation behind why some of stellar flares, particularly young star flares, show high temperature and exceptionally a large amount of

total energy, which is because the characteristic size of stellar flares is much larger than the solar flares. When the length of a flaring loop have a large value, the temperature of a solar flare increases in proportion to $L^{2/7}$ regardless of whether the magnetic field is the equivalent, for the reason that the conduction cooling become less efficient for a longer loop [22-25]. Figure 4 shows the correlation between the temperature of solar and stellar flares and their magnetic flux density obtained using the solar application.

5. Conclusions

A new Java-based application is being developed by Java as a stand-alone application, which provides an environment for determination of emission measure and temperature of solar flares. A solar application also allow to users define the magnetic reconnection rate (Sweet-Parker and Petschek model). The Swing component library was used to implement the GUI. In the current stage, the design of the user interface, coding for input forms and link with utilities were implemented. A solar application was developed by following 3 principles: intuitive, simplicity and user-friendliness. The combination of these 3 principles contributes to improving the usability. Advanced features implemented in the program can allow users to save their time. Java is basically an OS independent platform, however, tests on each OS may be necessary. At present, the test was only performed in Microsoft Windows and Linux, and will be performed in Mac OS in near future.

References

1. Garcia, H. A. (2004). Forecasting meth. for occurrence and magnitude of proton storms with solar hard X rays. Space Weather, Vol. 2, S06003.

2. Svestka, Z., Cliver, E.W. (1992). Eruptive sol. flares. Lecture Notes in Physics, 399, 1.

3. Haisch, B., Strong, K.T. and Rodono, M. (1991). Flares on the Sun and other Stars. Ann. Revs. Astron. Astrophys., 29, 275.

4. Feldman, U., Laming, J.M., Doschek, G.A. (1995). The correlation of Sol. flare temp. and EM Extrapolated to the Case of Stellar Flares. Astrophys. J. Lett., 451, L79.

5. Shimizu, T. (1995). Energetics and Occurrence Rate of Active-Region transient brightenings and implications for the heating of the active-region Cor. Publ. Astron. Soc. Japan, 47, 251–263.

6. Shibata, K., Magara, T. (2011). Sol. flares: Magnetohydrodynamic Processes. Living Rev. Sol. Phys. 8, 6.

7. Shibata, K., Yokoyama, T. (1999). Origin of the Universal correl. between the flare temp. and the EM for Solar and Stellar Flares. Astrophys. J. Lett., 526, L49–L52.

8. Yokoyama, T., Shibata, K. (1998). A Two-dimensional Magnetohydrodynamic simulation of chromospheric Evaporation in a Solar Flare Based on a Mag. Reconnection Model. Astrophys. J. Lett., 494 , L113.

9. Johns-Krull, C.M., Valenti, J.A., Koresko, C. (1999). Measuring the Mag. field on the Classical T Tauri Star BP Tauri. Astrophys. J., 516, 900–915.

10. White, S.M., Thomas, R.J. & Schwartz, R.A. (2005). Updated expressions for determining temp. and EM from goes soft x-ray measurements. Sol Phys, 227, 231.

11. Feldman, U. and Widing, K. G. (2003). Elemental abundances in the Sol. upper atmosphere derived by spectroscopic means. Space Sci Rev. 107, 665.

12. The Sunpy Community et al. (2015). SunPy-Python for sol. phys. Comput. Sci. Disc., 8, 014009.

13. Sweet P.A. (1958). Electromagnetic Phenomena in cosmical phys. Cambridge: Cambridge Univ. Press.

14. Parker E.N. (1957). Sweet's mechanism for merging mag. fields in conducting fluids.J. Geophys. Res., Vol.62, 509-520.

15. Parker E.N. (1963). The sol. flare phenomenon and theory of reconnection and annihilation of mag. fields. Astrophys. J. Supp., Vol.8, 177-211.

16. Petschek H.E. (1964). Mag. field annihilation. Physics of Solar Flares/ed. by W.N. Hess. NASA SP-50. Washington: DC, 425-439.

17. Sarsembayeva A.T., Belisarova F.B., Odsuren M., Sarsembay A.T., Kalymova Zh. (2012). Definition of reconnection rate of sol. flares registered in 2011-2012 years. Adv. Studies Theor. Phys., Vol.6, no.28, 1405-1408.

18. Sarsembayeva A.T., et al. (2019). 26 January, 2019 sol. flares diagnostics based on the soft x-ray EM. NEWS of the National Academy of Sciences of the Republic of Kazakhstan. Series of Physical and Mathematical. №2, 41-46.

19. Nitta S. (2004). Outflow structure and reconnection rate of the self-similar evolution model of fast mag. reconnection. Astrophysical Journal, Vol.610, 1117.

20. Matthaeus W.H., Lamkin S.L. (1985). Rapid mag. reconnection caused by finite amplitude fluctuations. Phys. Fluids, Vol.28, 303.

21. Tajima T., Shibata K. (1997). Plasma astrophys. Addison- Wesley.

22. Dere K.P. (1996). The rate of mag. reconnection observed in the sol. atmosphere. ApJ., Vol.472, 864.

23. Tsuneta S. (1996). Structure and dynamics of mag. reconnection in a sol. flare. The Astrophysical Journal, Vol.456, 840-849.

24. Tsuneta S., Masuda S., Kosugi T., Sato J. (1997). Hot and superhot plasmas above an impulsive flare loop. ApJ., Vol.478, 787.

25. Isobe H., Yokoyama T., Shimojo M., Morimoto T., Kozu H., Eto S., Narukage N., Shibata K. (2002). Reconnection rate in the decay phase of a long dur. event flare on 1997 May 12. ApJ., Vol.566, 528.

IRSTI 29.27.39; 29.27.47 https://doi.org/10.26577/phst-2019-2-p4

Generation of ultrahigh fields by microbubble implosion

M. Murakami[1*], A. Arefiev[2], M.A. Zosa[1] and J. Honrubia[3]

[1]*Institute of Laser Engineering, Osaka University, Osaka, 565-0871, Japan*
[2]*UC San Diego, 9500 Gilman Drive, 92093-0411, La Jolla, California, USA*
[3] *School of Aeronautical and Space Engineering, Madrid Polytechnic University, 3, Plaza adrenal Cisneros, Madrid, Spain*
[*]*e-mail: murakami-m@ile.osaka-u.ac.jp*

Breaking the 100-MeV barrier for proton acceleration will help elucidate fundamental physics and advance practical applications from inertial confinement fusion to tumor therapy. A novel concept of "microbubble implosion (MBI)" is proposed. In the MBI concept, bubble implosion combines micro-bubbles and ultra-intense laser pulses of 10^{20} – 10^{22} Wcm^{-2} to generate ultrahigh fields and relativistic protons. The bubble wall protons are subject to volumetric acceleration toward the center due to the spherically symmetric electrostatic force generated by hot electrons filling the bubble. Such an implosion can generate an ultrahigh density proton core of nanometer size on the collapse, which results in an ultrahigh electrostatic field to emit energetic protons in the relativistic regime. Laser intensity scaling is investigated for accelerated proton energy and attainable electrostatic field using MBI. Three-dimensional particle-in-cell and molecular dynamics simulations are conducted in a complementary manner. As a result, underlying physics of MBI are revealed such as bubble-pulsation and ultrahigh energy densities, which are higher by orders of magnitude than, for example, those expected in a fusion-igniting core of inertially confined plasma. MBI has potential as a plasma-optical device, which optimally amplifies an applied laser intensity by a factor of two orders of magnitude; thus, MBI is proposed to be a novel approach to the Schwinger limit.

Key words: Ultraintense ultrashort laser, relativistic protons, Schwinger limit, microbubble implosion, high-energy-density physics.
PACS numbers: 52.38.Kd, 52.30.Ex, 52.40.Kh, 52.65.-y

1 Introduction

In the past quarter century, the chirped-pulse-amplification (CPA) technique has increased the laser intensity more than ten mil-lion times [1]. Consequently, diverse research via laser-matter interactions has been pursued. Examples include fast ignition [2-4] and high energy particle acceleration for electrons and ions with respect to different applications [5-8]. These studies have been conducted under the relativistic electron regime [9], corresponding to the laser intensity I_L with $10^{18} < I_L$ (Wcm^{-2}) $< 10^{22}$. Utilizing laser fields is, however, far from straightforward because of their rapid oscillations. This presents a fundamental difficulty, particularly when attempting to accelerate ions that can then be used for a range of promising applications. A common approach to circumvent this difficulty is to first heat electrons in a laser-irradiated target [10-14].

As the heated electrons expand, they generate a strong electric field at the target surface that causes ions to accelerate [15-18]. For example, Coulomb explosion is a well-known scheme for ion acceleration [19-22], in which nm- to μm-sized clusters are irradiated by an intense laser pulse to blow off most of the electrons in a moment. The remaining ions then begin to spherically expand due to the strong Coulomb force. All these ion acceleration schemes strongly depend on the laser intensity applied on the targets. As well as the particle acceleration, high field science such as vacuum physics [23-29] is also important and fundamental topics in high energy density physics via laser. In quantum electrodynamics (QED), the Schwinger limit, $E_S = m_e^2c^3/eh \sim 1.3\text{x}10^{18}$ Vm^{-1}, is reported as the scale above which the electromagnetic field is expected to create electron-positron pairs spontaneously, where m_e is the electron mass, c is the speed of light in a vacuum, e is the elementary charge, and h is the Planck constant. The electric field at the Schwinger limit corresponds to the laser intensity $I_L \sim 2.3\text{x}10^{29}$ Wcm^{-2}. To date, many studies have focused on increasing laser performance with

regard to power and intensity [30-33]. While the threshold for electron-positron pair production may be substantially below E_S for multiple focusing pulses [34, 35], the current "distance" in the laser intensity to the Schwinger limit is still roughly five to six orders of magnitude away even by taking such measures into account.

Recently we have proposed a conceptually new approach to generate ultrahigh fields and resultant high energy protons, which is referred to as "microbubble implosion" (MBI), picture is illustrated in Figure 1(a). Suppose that a spherical micron-sized bubble, prepared artificially in a solid target, is forced to implode when placed into a heat bath composed of hot electrons (Figure 1(b)), which are actively circulating in and outside of the bubble [36]. For simplicity, the target is assumed to be pure hydrogen. The ion implosion continues until the ions become compressed to a nanometer scale such that their radial inward motion is halted by the resulting outward electric field. This means further compression of the original laser energy in space and time in the shape of an extremely dense ion core, which leads to generation of an ultrahigh electric field at the center. This field is much stronger than the field that initiated the implosion, and it causes a violent explosion of the compressed ions, with resulting energies many times higher than the energy gained during the implosion. Below we construct a simple semi-analytical model, which encapsulates the important features obtained from multidimensional simulations. Not only can this model easily visualize the underlying physics of this novel phenomenon but also define the limiting performance.

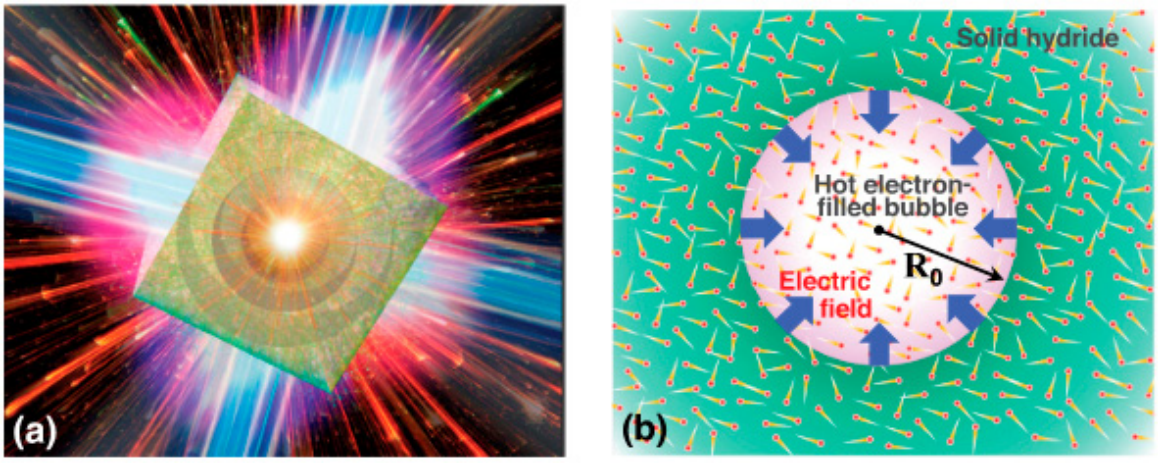

Figure 1 – (a) Envisioned picture showing all of the main events of microbubble implosion (MBI), i.e., laser illumination, hot electron spread, implosion, and proton flash at the end.
(b) Schematic picture showing the core mechanism of MBI. Being filled with hot electrons in the bubble, the bulk of the protons begin to accelerate toward the center in a spherically symmetric manner.

Phenomena such as converging shock waves and sonoluminescence are similar to a bubble implosion. Shock waves are observed in many branches of physics. Although sonoluminescence is a relatively new phenomenon in the acoustics field, Lord Rayleigh proposed the basic idea (contraction of a water bubble) over a century ago. The behavior of bubble implosions reported in this study remarkably differs. Extremely high temperatures and low densities characterize the physical states of collapsing converging waves at the center in shock waves and sonoluminescence. By contrast, extremely high densities and practically zero temperatures for protons characterize bubble implosions.

2 Dynamics of Microbubble Implosion

2.1 One-dimensional hybrid simulation

Hot electron distribution in the bubble is the key physical issue in MBI. We first conducted 1D hybrid simulations, in which electrons and ions are treated as an electrostatic field and particles, respectively. Practically, the specific value of the ionization degree in space, $\alpha = n_{i0}/n_{s0}$, results from the interplay between the laser and the target material. Hence, it depends on the external parameters such as the absorbed laser energy and the target volume. The electron distribution in the bubble is obtained by solving the Poisson Boltzmann (P-B) equation, $\nabla\varphi = 4\pi e[n_{ec} \exp(e\,\varphi\,/T_e)$

– n_i], where φ is the electric potential and n_{ec} is the temporal electron density at the center. After normalizing the P-B equation, the present system is found to depend on a single dimensionless parameter defined by $\Lambda = R_0/\lambda_{Di}$, where $\lambda_{Di} = (T_e/4\pi n_{i0}e^2)^{1/2}$ is the Debye length. As a function of Λ, the P-B equation is numerically solved to give $\varphi(r)$ and consequently $n_e(r)$ under the appropriate boundary conditions. The potential profile $\varphi(r)$ evolves over time in accordance with the temporal ion density profile $n_i(r)$. The two dimensionless variables, R_1/R_0 and Λ, constitute the analysis as control parameters.

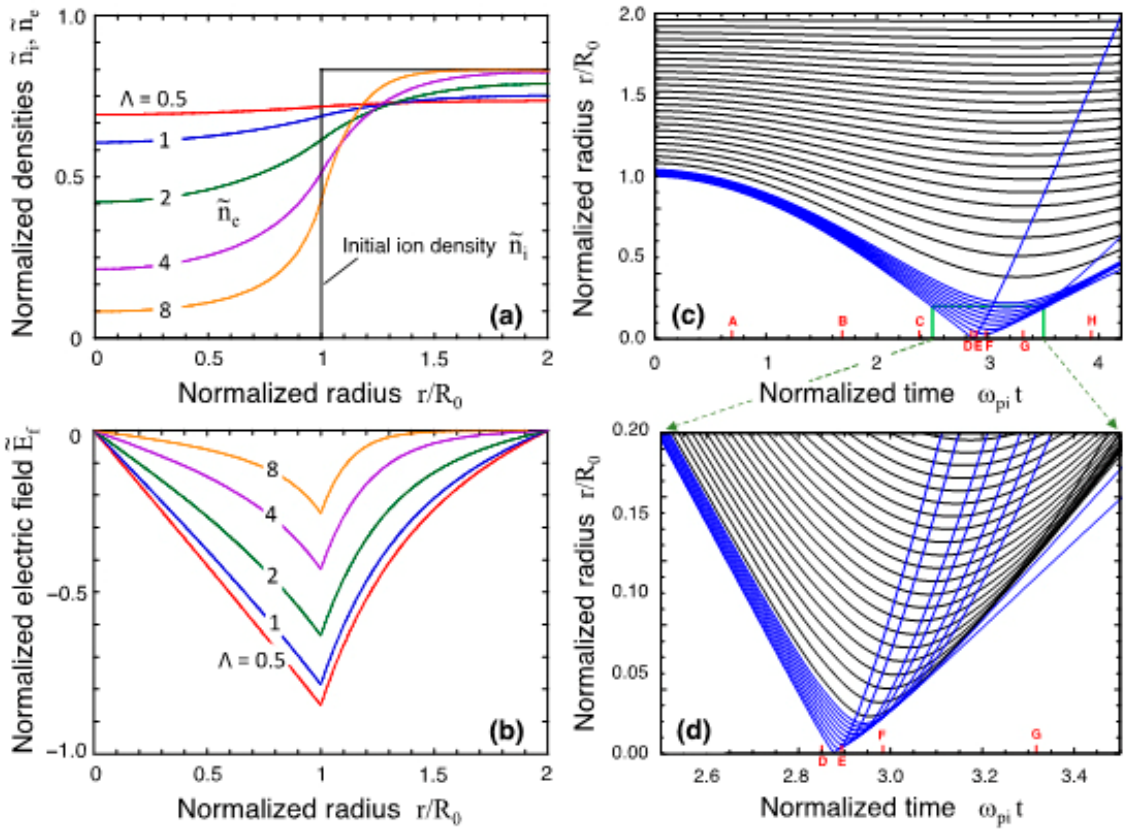

Figure 2 – (**a**) Initial density profiles of the electron and the ion normalized by the initial ion density, respectively. (**b**) the electric field as a function of Λ. (**c**) Ion trajectories obtained by 1D simulation under $R_1/R_0 = 2$ and $\Lambda = 0.5$. The black curves correspond to initial radii, while the blue curves divide the innermost segment to better observe the implosion dynamics. The labels, A – H, are to compare other physical quantities in the following Figures. For the solid density, the normalized unit time corresponds to 3.4 fs. (**d**) Magnified view of the rectangle part in (**c**).

Figures 2(a) and (b) show the initial profiles for the electron density n_e (r) and the electric field, respectively, obtained for different values of Λ and a fixed initial ion density profile normalized by n_{i0}. The electron profiles for $\Lambda < 1$ are rather flat over the entire domain, while they conspicuously reduce in the bubble with increasing Λ (>2). It is convenient to normalize time t and use the dimensionless quantity $\omega_{pi0}t$ instead, where $\omega_{pi0} = \sqrt{4\pi n_{i0}Z^2e^2/m_i}$ is the ion plasma frequency and m_i is the ion mass.

Figure 2(c) shows the ion trajectories for the entire time region under the bubble conditions of $R_1/R_0 = 2$ and $\Lambda = 0.5$. The black curves correspond to initial radii with a constant increment of $\Delta r = 0.04R_0$, while the blue curves subdivide the innermost segment to better resolve the implosion dynamics. The labels along the time axis, A – H, are to compare other physical quantities in subsequent figures.

Figure 2(d) shows a zoom-in of the rectangular in Figure 2(c). Until time D, all of the ion trajectories remain laminar, so that one curve does not intersect another. However, upon the collapse (time E), the innermost trajectory is strongly ejected radially outwards and this is the phenomenon that we call the proton flash. In Figure 2(d), the innermost seven

trajectories in blue represent flashed protons and they behave quite differently from the other trajectories. These trajectories sharply cut across the other trajectories, confirming that the flashed protons quickly slide down a Coulomb potential that can be effectively viewed as quasi-static. These "runaway" protons are emitted from a very small volume with $r \sim 0.05R_0$ due to an explosive acceleration under the ultrahigh electric field that is generated by the accumulated proton core at the center.

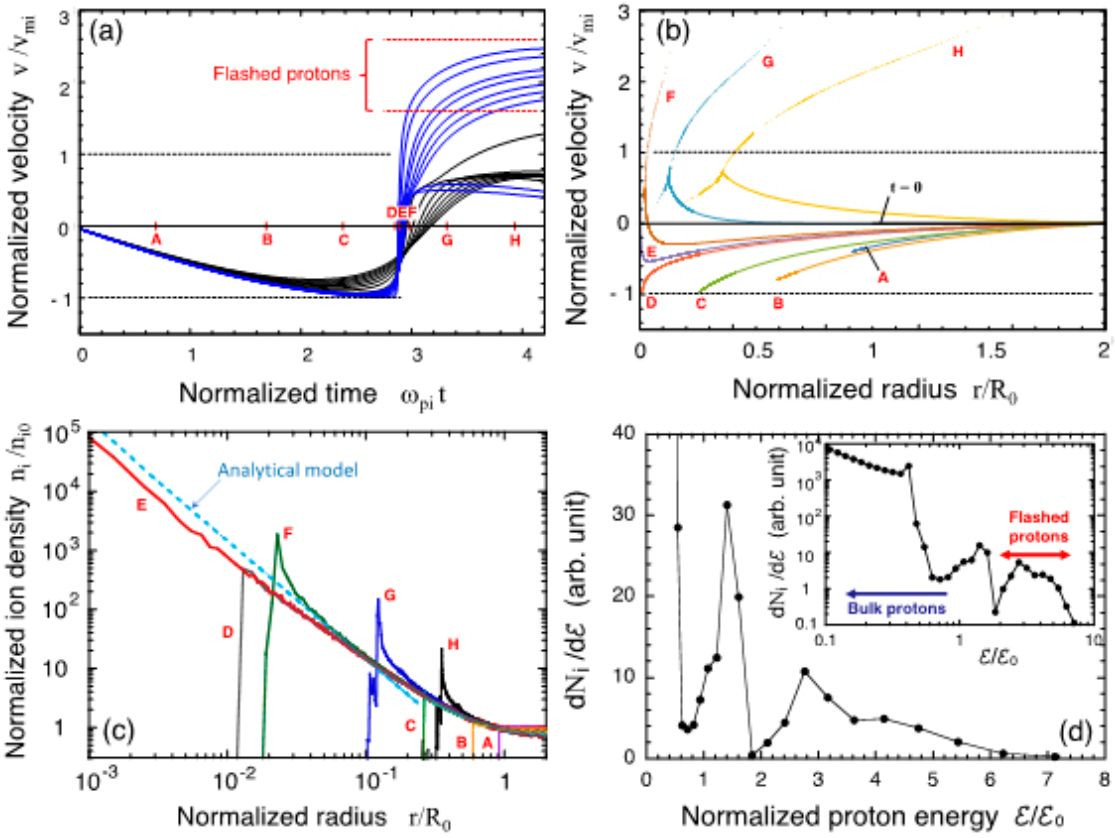

Figure 3 – (**a**) Temporal evolution of the velocities of individual protons normalized by the maximum implosion velocity v_{mi}. (**b**) Overall view of the velocity profiles at the snapshot times A – H. (**c**) Density profiles normalized by the solid density at different times A – H. **(d)** Energy spectrum at time H. The inset stands for the same data given in the main frame but in double-logarithmic scales. The unit of the energy is chosen to be the maximum kinetic energy in the implosion phase. The two-humped structure is attributed to the acceleration process at the singular behavior at the center

Figure 3(a) shows the velocity evolution of the flashed protons and the surrounding protons, normalized by the maximum implosion velocity v_{mi}. The blue and black curves correspond to those in Figure 2(d). Upon the collapse (times D – F), the velocity of the flashed protons drastically increases, exceeding the maximum implosion velocity by a factor of 2.0 – 2.5, which are simply squared to give corresponding energy amplification by a factor of 4 – 6. This energy amplification for the flashed protons is due to their sliding down the steep Coulomb potential slope. The innermost protons are the first ones to be reflected near the center. The dynamics of the other protons that follow and that are located a bit outwards is similar, but the expulsion is slightly delayed and the resulting energy amplification factor is smaller.

Figure 3(b) shows snapshots of the proton velocity as a function of radius for times A – H in Fig. 2(c). For practical laser and target parameters, the proton flash occurs over a very short time interval and a very small volume corresponding to times D – F. The flashed protons have a much higher velocity than surrounding bulk protons, as can be seen in snapshots

G and H. It should be noted that, at such later times, a snowplow-like two-stream-structure is formed.

2.2 Three-dimensional Particle-In-Cell (PIC) simulation

We performed 3D PIC simulations with an open-source code EPOCH [37]. We employed such a periodic boundary condition that a single bubble was located at the center of a cubic plasma volume with one side of L = 1200 nm and the minimum cell size of 6 nm. For simplicity, laser-matter interaction was not taken into account. Initially, the bubble of R_0 = 300 nm was set to be empty, and a uniform charge-neutral plasma surrounding the bubble was composed of hot electrons with T_e = 10 MeV and cold ions with density of $n_{i0} = n_{e0} = 10^{21}$ cm^{-3}.

Figure 4(a) shows the snapshots of bubble implosion with the proton density distributions color-coded. The pulsating behavior of MBI is robust despite that the shrinking bubble is substantially deformed into a squared shape due to accumulated numerical errors under the Cartesian mesh employed in the PIC code. Figure 4(b) shows the temporal evolution of the proton energy spectrum. The pulsation period is estimated to be $T_{cyc} \sim 150$ fs, which indeed agrees with the interval between the 1st ($t \sim 70$ fs) and the 2nd ($t \sim 220$ fs) proton flash. Furthermore, throughout the explosion phase, the maximum implosion energy of 230 keV is amplified up to 1.4 MeV with an amplification factor of ~ 6, which agrees well with the results observed in the 1D hybrid simulation.

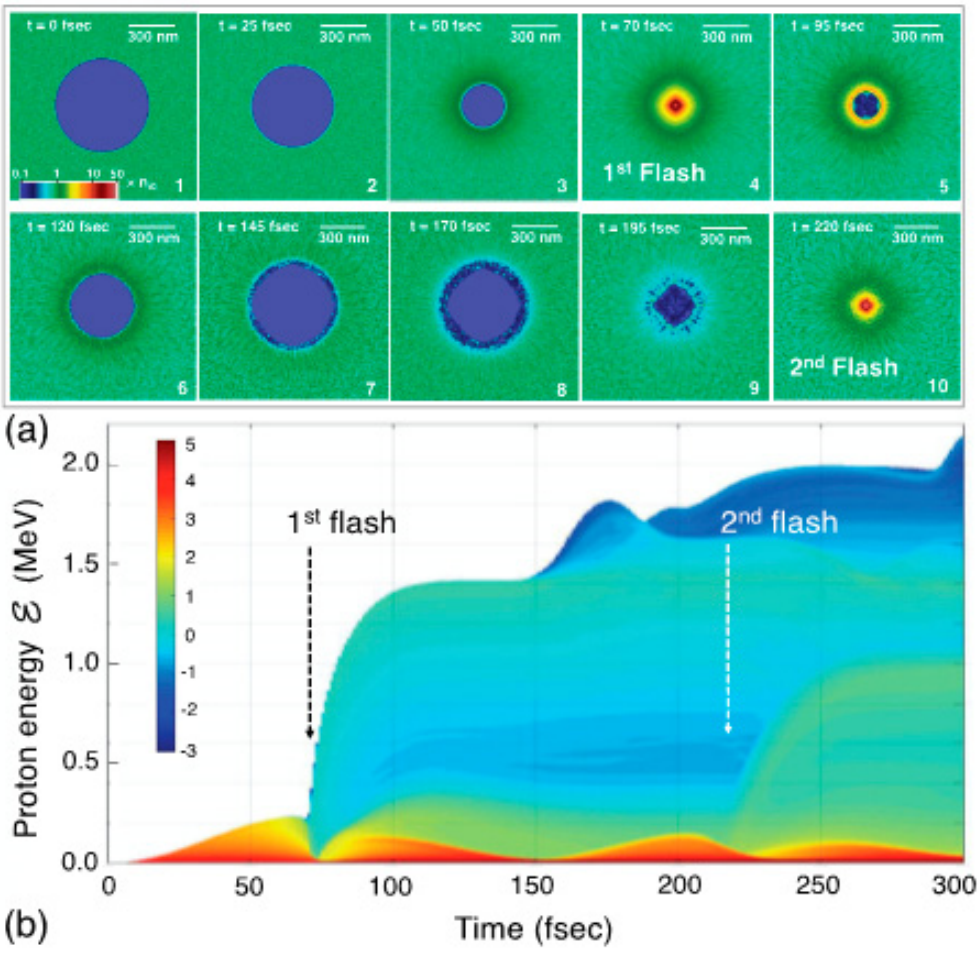

Figure 4 – 3D PIC simulation of MBI. Initially, the bubble of R_0 = 300 nm is empty. A uniform charge-neutral plasma surrounding the bubble is composed of hot electrons with T_e = 10 MeV and cold protons with density of $n_{i0} = n_{e0} = 10^{21}$ cm^{-3}. **(a)** Snapshots of the bubble collapse with the proton density distributions being color-coded. **(b)** Temporal evolution of the proton energy spectrum for the same case as in panel **(a)**. The integers β assigned along the color bar in panel **(b)** indicate proton density n_i such that $n_i = 10^{\beta}$ cm^{-3}eV^{-1}.

3 Generation of Ultrahigh-Energy-Density Nanosphere

While PIC simulations can provide a comprehensive physical picture by treating a lot of particles, the dynamic range is limited because of the fixed size of the cartesian cells. In contrast, molecular dynamic (MD) simulations can treat the dynamics over a much wider dynamic range, taking all binary collisions into account, but because of that they are limited to a much smaller number of particles.

Figure 5(a) compares the density profiles at the maximum compression obtained by 3D MD simulations and the 1D model. The fixed parameters are $R_0 = 1$ nm and $n_{i0} = 5\text{x}10^{22}$ cm^{-3}, assuming $\Lambda << 1$. The inset shows the initial configuration of the pseudo-particles used for the simulations, where we took the innermost four atomic layers into account. One thousand pseudo-protons are uniformly arranged on each of the four layered spherical surfaces [38] with an interatomic distance $d_0 = 0.27$ nm. Each pseudo-proton carries a mass and charge corresponding to about 10 real protons. The electrons were treated as a uniform background. Here, it should be noted that in the 3D MD simulations, all binary collisions between the pseudo-protons are precisely computed. This feature is indispensable when evaluating proton dynamics on such an infinitesimally small scale as nanometer.

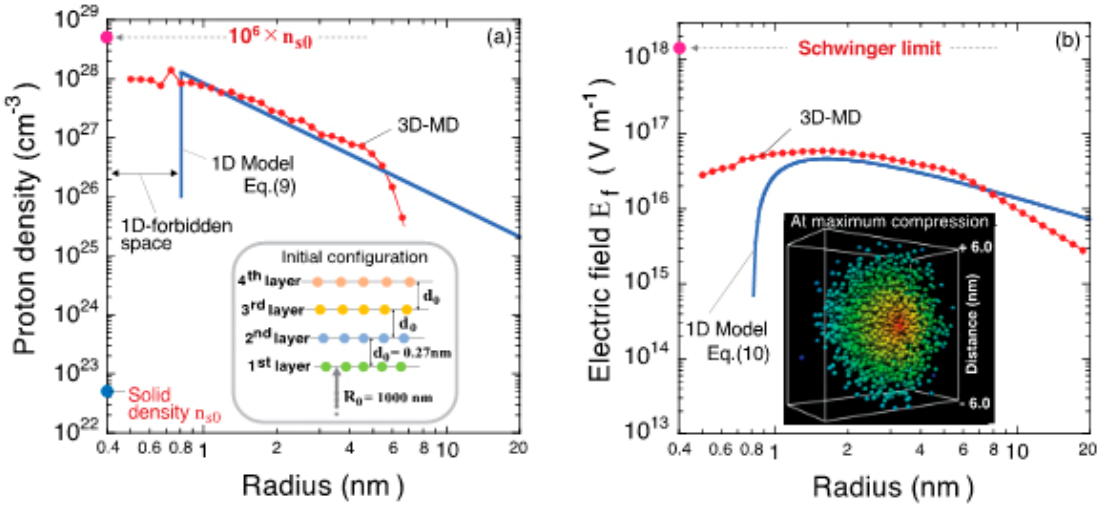

Figure 5 – **(a)** Comparison of the proton density at the maximum compression between the 3D molecular dynamic simulations and the 1D model. Fixed parameters are $R_0 = 1$ nm and $n_{i0} = 5\text{x}10^{22}$ cm^{-3}. The curve labeled "3D-MD" is obtained using the innermost four layers as shown in the inset. **(b)** Comparison of the electrostatic fields between the simulations and the model. The inset shows the proton distribution around the center (color-coded in accordance with the distance from the center).

It is remarkable that the four atomic layers eventually stagnate after imploding down to the small radii < 6 nm. Upon the bubble collapse, the particles scatter around the 1D minimum radius, $r = r_{min} \sim 0.8$ nm, by random collisions, and a substantial part of them is further compressed into an even smaller central volume (1D-forbidden space). The characteristic time interval of proton stagnation at the center is about 10 as. The observed average proton densities inside the sphere for $r < 1$ nm are roughly 10^{28} cm^{-3} as demonstrated in Figure 5(a). Meanwhile, the maximum density predicted by the 1D model is $1.3\text{x}10^{28}$ cm^{-3}, which together with the overall spatial profile agrees well with the simulation result.

Figure 5(b) compares the electric field obtained by the 1D model, with the 3D MD simulation. The 1D curve excellently reproduces the simulation curve in the core volume for $r < 6$ nm. By contrast, for r > 6 nm, the simulation curve decays more swiftly than the 1D curve according to the power law, $E_f \sim r^{-2}$. This is because the almost all the protons are accumulated in the core volume at the maximum compression. The inset shows the hemispherical perspective view of the protons distributed around the target center at the

maximum compression, where distances of the proton from the center are color-coded. To the best of our knowledge, we do not know of any other principles published in the literature to achieve such unprecedented physical quantities on earth as the compressed density on the order of 10^5 – 10^6 times the solid density and the electrostatic field on the order of 10^{16} – 10^{17} Vm^{-1}.

4 Conclusions

We propose a novel concept, bubble implosion, to generate an ultrahigh field to accelerate pro- tons to relativistic energies. A simple model and 1D, 2D, and 3D simulations comprehensively investigate the dynamics of the bubble implosion. This phenomenon is very likely to occur in reality. A stable implosion shrinks to a nanometer size and achieves an ultradense proton core, forming an unprecedentedly high electric field and producing proton flashes. The generation of an ultrahigh field is attributed to spherical convergence to the center. Moreover, Coulomb-imploded bubbles are robust and behave as nano-pulsars repeating implosion and explosion to emit energetic protons. Although the present paper assumes pure hydrogen targets, a modified scenario should be applicable to other hydrides.

Current laser technology is suitable to experimentally identify bubble implosion by observing proton emissions at relativistic energies, which will be a major breakthrough to crack the 100-MeV barrier. For such experiments, a uniform and well-activated Coulomb field must be created inside the bubbles by laser irradiation of micron-sized bubbles embedded inside a solid target. We have demonstrated in terms of the 2D simulation that a symmetric bubble implosion can be achievable even under a realistic condition of laser-matter interaction. Consequently, the present concept should provide a new platform to elucidate fundamental phenomena in the fields of high-energy-density physics [39] and astrophysics.

Microbubble implosion thus holds promise in principle to achieve such an ultrahigh-energy-density state of matter that is higher by orders of magnitude than those expected in a fusion-igniting core of inertially confined plasma. Introducing high-Z materials to MBI as the target composition or a surface coating are expected to achieve even higher electric fields and resultant proton energies. MBI has potential as a plasma-optical device, which optimally amplifies the applied laser intensity by a factor of two orders of magnitude.

Acknowledgments

M.M. was supported by the Japan Society for the Promotion of Science (JSPS). A.A. was supported by the Air Force Office of Scientific Research under Award No. FA9550-17-1-0382.

References

1. Strickland D. & Mourou G. (1985). Compression of amplified chirped optical pulses. Opt. Commun., 55, 447-449.

2. Tabak M., Hammer I., Glinsky M. E., Kruer W. L., Wilks S. C., Woodworth J., Campbell E. M., Perry M. D., & Mason R. J. (1994). Ignition and high gain with ultrapowerful lasers. Phys. Plasmas, 1, 1626.

3. Wilks S. C., Langdon A. B., Cowan T. E., Roth M., Singh M., Hatchett S., Key M. H., Pennington D., MacKinnon A., & Snavely R. A. (2001). Energetic proton generation in ultra-intense laser–solid interactions. Phys. Plasmas, 8, 542.

4. Roth M., Cowan T. E., Key M. H., Hatchett S. P., Brown C., Fountain W., Johnson J., Pennington D. M., Snavely R. A., Wilks S. C., Yasuike K., Ruhl H., Pegoraro F., Bulanov S. V., Campbell E. M., Perry M. D., & Powell H. (2001). Fast ignition by intense laser-accelerated proton beams. Phys. Rev. Lett., 86, 436-439.

5. Daido H., Nishiuchi M., & Pirozhkov A. S. (2012). Review of laser-driven ion sources & their applications. Rep. Prog. Phys., 75, 056401.

6. Tajima T. & Dawson J. M. (1979). Laser Electron Accelerator. Phys. Rev. Lett., 43, 267.

7. Bulanov S. V. & Khoroshkov V. S. (2002). Feasibility of using laser ion accelerators in proton therapy. Plasma Phys. Rep., 28, 453-456.

8. Gonsalves A. J., Nakamura K., Daniels J., Benedetti C., Pieronek C., de Raadt T. C. H., Steinke S., Bin J. H., Bulanov S. S., van Tilborg J., Geddes C. G. R., Schroeder C. B., Toth Cs., Esarey E., Swanson K., Fan-Chiang L., Bagdasarov G., Bobrova N., Gasilov V., Korn G., Sasorov P., & Leemans W. P. (2019). Petawatt Laser Guiding and Electron Beam Acceleration to 8 GeV in a Laser-Heated Capillary Discharge Waveguide. Phys. Rev. Lett., 122, 084801.

9. Atzeni S. & Meyer-ter-Vehn J. (2004). Fast ignition. In The Physics of Inertial Fusion: BeamPlasma Interaction, Hydrodynamics, Hot Dense Matter. Oxford University Press.

10. Malka V., Fritzler S., Lefebvre E., dfHumieres E., Ferrand R., Grillon G., Albaret C., Meyroneinc S., Chambaret J.-P., Antonetti A., & Hulin D. (2004). Practicability of protontherapy using compact laser systems. Med. Phys., 31, 1587.

11. Borghesi M., Fuchs J., Bulanov S. V., Mackinnon A. J., Patel P. K., & Roth M. (2006). Fast Ion Generation by High-Intensity Laser Irradiation of Solid Targets and Applications. Fusion Sci. Technol., 49, 412.

12. Nakamura T., Bulanov S. V., Esirkepov T., & Kando M. (2010). High-Energy Ions from Near-Critical Density Plasmas via Magnetic Vortex Acceleration. Phys. Rev. Lett., 105, 135002.

13. Yin L., Albright B. J., Bowers K. J., Jung D., Fernandez J. C., and Hegelich B. M. (2011). Three-Dimensional Dynamics of Breakout Afterburner Ion Acceleration Using High-Contrast Short-Pulse Laser and Nanoscale Targets. Phys. Rev. Lett., 107, 045003.

14. Weng S. M., Liu M., Sheng Z. M., Murakami M., Chen M., Yu L. L., & Zhang J. (2016). Dense blocks of energetic ions driven by multi-petawatt lasers. Sci. Rep., 6, 22150.

15. Esirkepov T., Borghesi M., Bulanov S. V., Mourou G., & Tajima T. (2004). Highly Efficient Relativistic-Ion Generation in the Laser-Piston Regime. Phys. Rev. Lett., 92, 175003.

16. Murakami M. & Basko M. M. (2006). Self-similar expansion of finite-size non-quasi-neutral plasmas into vacuum: Relation to the problem of ion acceleration. Phys. Plasmas, 13, 012105.

17. Bulanov S. S., Bychenkov V. Yu., Chvykov V., Kalinchenko G., Litzenberg D. W., Matsuoka1 T., Thomas A. G. R., Willingale L., Yanovsky V., Krushelnick K., & Maksimchuk A. (2010). Generation of GeV protons from 1 PW laser interaction with near critical density targets. Phys. Plasmas, 17, 043105.

18. Haberberger D., Tochitsky S., Fiuza F., Gong C., Fonseca R. A., Silva L. O., Mori W. B., & Joshi C. (2012). Collisionless shocks in laser-produced plasma generate monoenergetic high-energy proton beams. Nat. Phys., 8, 95–99.

19. Ditmire T., Zweiback J., Yanovsky V. P., Cowan T. E., Hays G., & Wharton K. B. (1997). High-energy ions produced in explosions of superheated atomic clusters. Nature, 386, 54-56.

20. Zweiback J., Smith R. A., Cowan T. E., Hays G., Wharton K. B., Yanovsky V. P., & Ditmire T. (2000). Nuclear Fusion Driven by Coulomb Explosions of Large Deuterium Clusters. Phys. Rev. Lett., 84, 2634.

21. Murakami M. & Mima K. (2009). Efficient generation of quasimonoenergetic ions by Coulomb explosions of optimized nanostructured clusters. Phys. Plasmas, 16, 103108.

22. Peano F., Peinetti F., Mulas R., Coppa G., & Silva L. O. (2006). Kinetics of the Collisionless Expansion of Spherical Nanoplasmas. Phys. Rev. Lett., 96, 175002.

23. Sauter F. (1931). Uber das Verhalten eines Elektrons im homogenen elektrischen Feld nach der relativistischen Theorie Diracs. Z. Phys., 69, 742.

24. Heisenberg W. & Euler H. (1936). Consequences of Dirac's theory of positrons. Z. Phys. 98, 714.

25. Schwinger J. (1951). On gauge invariance and vacuum polarization. Phys. Rev., 82, 664.

26. Popov V. S. (2002). On Schwinger mechanism of e^+e^- pair production from vacuum by the field of optical and X-ray lasers. Phys. Lett. A, 298, 83.

27. Narozhny N. B., Bulanov S. S., Mur V. D., & Popov V. S. (2004). On e^+ e^- pair production by a focused laser pulse in vacuum. Phys. Lett. A, 330, 1.

28. DiPiazza A., Lotstedt E., Milstein A. I., & Keitel C. H. (2009). Barrier control in tunneling e^+ – e^- photoproduction. Phys. Rev. Lett., 103, 170403.

29. Dumlu C. K. & Dunne G. V. (2010). The Stokes Phenomenon and Schwinger Vacuum Pair Production in Time-Dependent Laser Pulses. Phys. Rev. Lett., 104, 250402.

30. Korn G., (2011).WhiteBook on ELI Science and Technology with Ultra-Intense Lasers. CNRS: Cedex.

31. Garrec B. L., Sebban S., Margarone D., Precek M., Weber S., Klimo O., Korn G., & Rus B. (2014). ELI-beamlines: Extreme light infrastructure science and technology with ultra-intense lasers. Proc. SPIE, 8962, 89620I.

32. Kuhn S., Dumergue M., Kahaly S., Mondal S., Csizmadia T., Farkas B., Major B., Cormier E., Kalashnikov M., Calegari F., Devetta M., Frassetto F., Poletto L., Stagira S., Vozzi C., Nisoli M., Rudawski P., Maclot S., Campi F., Wikmark H., Arnold C. L., Heyl C. M., Johnsson P., L'Huillier A., Lopez- Martens R., Haessler S., Bocoum M., Boehle F., Vernier A., Iaquaniello G., Skantzakis E., Papadakis N., Kalpouzos C., Tzallas P., Lpine F., Charalambidis D., Osvay K., & Sansone G. J. (2017). The ELI-ALPS facility: the next generation of attosecond sources. Phys. B: At. Mol. Opt. Phys., 50, 132002.

33. Gales S., Tanaka K. A.,. Balabanski D. L, Negoita F., Stutman D., Tesileanu O., Ur C. A., Ursescu D., Andrei I., Ataman S., Cernaianu M. O., D'Alessi L., Dancus I., Diaconescu B., Djourelov N., Filipescu D., Ghenuche P., Ghita D. G., Matei C., Seto K., Zeng M., & Zamfir N. V. (2018). The extreme light infrastructure—nuclear physics (ELI-NP)

facility: new horizons in physics with 10 PW ultra-intense lasers and 20 MeV brilliant gamma beams. Rep. Prog. Phys., 81, 094301.

34. Bulanov S. S., Mur V. D., Narozhny N. B., Nees J., & Popov V. S. (2010). Multiple colliding electromagnetic pulses: a way to lower the threshold of e+e− pair production from vacuum. Phys. Rev. Lett., 104, 220404.

35. Bulanov S. S., Esirkepov T. Z., Thomas A. G. R., Koga J. K., & Bulanov S. V. (2010). On the Schwinger limit attainability with extreme power lasers. Phys. Rev. Lett., 105, 220407.

36. Murakami M., Arefiev A., & Zosa M. A. (2018). Generation of ultrahigh field by micro-bubble implosion. Sci. Rep., 8, 7537.

37. Arber T. D., Bennett K., Brady C. S., Lawrence-Douglas A., Ramsay M. G., Sircombe N. J., Gillies P., Evans R. G., Schmitz H., Bell A. R., & Ridgers C. P. (2015). Contemporary particle-in-cell approach to laser-plasma modeling. Plasma Phys. Controlled Fusion, 57, 113001.

38. Murakami M., Sarukura N., Azechi H., Temporal M., & Schmitt A. J. (2010). Optimization of irradiation configuration in laser fusion utilizing self-organizing electrodynamic system. Phys. Plasmas, 17, 082702.

39. Koga J., Murakami M., Arefiev A.V., & Nakamiya Y. (2019). Probing and possible application of the QED vacuum with micro-bubble implosions induced by ultra-intense laser pulses. Matter Radiat. Extremes, 4, 034401.

IRSTI 29.27.07 https://doi.org/10.26577/phst-2019-2-p5

Plasma anisotropy around non-spherical conductive dust particles

G. Sukhinin*, M. Salnikov and A. Fedoseev

[1] *Institute of Thermophysics SB RAS, 1, Lavrentyev Ave., 630090, Novosibirsk, Russia*
**e-mail: sukhinin@itp.nsc.ru*

This paper presents a computational model that allows self-consistent simulation of plasma distributions around isolated strongly charged dust grains with different geometries: spherical, ellipsoidal, and disk-shaped dust particles. All particles in this work were considered conductive and were oriented so that cylindrical symmetry was preserved in the computational area. Dust particles of various shapes were placed in an external field, and the process of ion focusing and the formation of a wake behind them were studied. As a result of the calculation by this model, self-consistent distributions of the space charge and plasma potential around non-spherical dust particles, as well as the dependence of the main characteristics of the wake - the magnitude of the first potential maximum and its position - on the magnitude of the external field was obtained. The analysis of spatial distributions showed that near the dust grains of the same electric capacity almost identical spatial distributions of the space charge and potential are formed. When normalizing the dependence of the wake maximum value on the root of the electric capacitance, all data are described by a single parametric curve with good accuracy, which allows one to predict the plasma parameters around the dust particle without resorting to direct calculations.

Key words: dusty plasma, non-spherical dust particle, wake, plasma polarization, rod-like dust particles.
PACS numbers: 52.20.−j, 52.27.Lw.

1 Introduction

For several decades, the study of micron-sized solid particles placed in plasma has been conducted. Dusty plasma is studied in laboratory conditions [1-4], on the Earth [5], and in microgravity conditions at the International Space Station and in parabolic flights [6,7]. Numerical modeling also kept pace with the experimental study of dust particles - to calculate the plasma parameters around isolated dust particles, as well as dust particle clusters, a wide range of computational methods were developed and (or) applied: molecular dynamics [8], linear response [9,10], Monte Carlo, “Particle-In-Ccell" [11-13], etc.

Experimental and numerical methods have been studied many phenomena associated with dusty plasma: dust grains charging, the orientation of non-spherical dust particles in a discharge, self-organization of dust particles in a plasma, the formation of crystalline and liquid structures, phase transitions between these structures, wave effects in dust crystals and plane-transverse sound waves and many others. The study of dusty plasma easily obtained in the laboratory has opened a wide path for the experimental modeling of processes occurring in a gas, liquid, and solid matter at a kinetic level.

Based on the foregoing, it can be concluded that one of the main, fundamental phenomena in this complex medium is the self-organization of dust particles. Because of this, the most interesting are the reasons for the formation of ordered structures. Due to the fact that, using experimental studies, no such reasons were found, the already mentioned numerical methods were utilized to modulate the effect that a dust particle has on its surrounding.

Today, it is generally accepted that pseudo-periodic oscillating structures in potential and ion density are responsible for the dust particles ordering, which are formed behind a dust particle in a plasma stream or in an external electric field [14-16]. This structure is called a wake, and is a consequence of ion focusing behind the dust grain. The most popular approaches for studying wakes are the already mentioned PIC [11-13] and LR

[9,10] numerical methods. However, a large number of papers are devoted to studying the distribution of the plasma potential near spherical dust particles, while in nature dust grains are rarely of such a regular shape.

In [17-20], the authors of this article demonstrated the results of calculations of a model in which the distributions of space charges and potentials were determined in a self-consistent manner also around spherical particles. This article presents the dependences of the density distribution and the space charge potential, as well as the dependence of the dipole moment of the "dust particle - ion cloud" system for nonspherical particles: a flattened and elongated ellipsoid.

2 Model

Due to the fact that in the most detailed way the model has already been described in the works [17-20], only its main points will be described later. For convenience, a particle whose geometry is an elongated ellipsoid will be called ellipsoidal, and the geometry of which is a flattened ellipsoid - disk-shaped.

The geometry of the main computational domain was selected as a cube. An impenetrable sphere of radius $r_0 << \lambda_i$ was placed in the center of this cube - a figure simulating the dust particle itself. Here, λ_i is the Debye ionic length. At the very beginning of the calculations, one ion was generated, the coordinates and velocities of which were set randomly. The speeds were set so that their values obeyed the Maxwell distribution.

To calculate the trajectory of this generated ion, Newton's motion equations were used. From these equations, the trajectory of this ion in a field induced by a dust particle and an external electrostatic field was calculated. During this movement, this ion could:

1) fall on a dust particle
2) fly beyond the computational domain
3) collide with a neutral atom.

The modeling region selected in the form of a cube was divided into cells (i,j) according to the coordinates ρ and z respectively, so that the volume of each cell obeyed the following law:

$$V_{i,j} = 2\pi\rho_i \Delta\rho_i \Delta z_j. \tag{1}$$

The time $T_{i,j}$, that the observed ion spent in the space segment (i,j), is fixed, normalized to the volume of the segment $V_{i,j}$, where the ion was located, after which obtained value is summed up with the already accumulated time statistics for this space element:

$$n_i(i,j) = n_i(i,j) + \frac{T_{i,j}}{V_{i,j}}. \tag{2}$$

The parameters in the system were calculated using dimensionless variables in which the dimensionless charge of the dust particle $\widetilde{Q}$ and the external electrostatic field $\widetilde{E}$ are given by the expressions:

$$\widetilde{Q} = \frac{e^2 Z_d}{\lambda_i k T_i}, \quad \widetilde{E} = \frac{eE\lambda_i}{kT_i}. \tag{3}$$

At the beginning of the calculation, a potential is set in the system as follows:

For a spherical particle:

$$U_0(\rho,z) = -\frac{\widetilde{Q}}{r}\exp(-r) - \widetilde{E}z, \quad r = \sqrt{\rho^2 + z^2}. \tag{4}$$

For an ellipsoidal particle:

$$U_{0,el}(\rho,z) = -\frac{\tilde{Q}}{\sqrt{c^2 - a^2}} \times \mp \operatorname{Arth}\sqrt{\frac{c^2 - a^2}{\xi + c^2}}\exp(-r) - \tilde{E}z. \tag{5}$$

For a disk-shaped particle:

$$U_{0,disk}(\rho,z) = -\frac{\tilde{Q}}{\sqrt{a^2 - c^2}} \times \times \operatorname{arctg}\sqrt{\frac{a^2 - c^2}{\xi + c^2}}\exp(-r) - \tilde{E}z. \tag{6}$$

In this model, the figures are selected as ellipsoids of revolution, the two semi-axes of which are equal to each other. The length of the equal semi-axes is denoted as a, while the length of the third axis is denoted as c. In space, the dust particles were oriented so that the semi-axis c was parallel to

the external field vector. This orientation of the grain allows to maintain cylindrical symmetry in the model.

From the statistics accumulated over cylindrical segments, the dimensionless distribution of space charge $n(\rho,z)$, is calculated, which can be written in the form:

$$n(\rho,z)=\frac{n_i(\rho,z)-n_e(\rho,z)}{n_\infty}. \quad (7)$$

From which the self-consistent potential in the system is calculated:

For a spherical particle:

$$U(\rho,z)=-\frac{\widetilde{Q}}{r}+\iiint\limits_{V_{syst}}\frac{n(\rho',\varphi',z')\rho'd\rho'd\varphi'dz'}{\left|\vec{r}-\vec{r}'\right|} \quad (8)$$

For an ellipsoidal particle:

$$U_{el}(\rho,z)=-\frac{\tilde{Q}}{\sqrt{c^2-a^2}}\operatorname{Arth}\sqrt{\frac{c^2-a^2}{\xi+c^2}}+$$

$$+\iiint\limits_{V_{syst}}\frac{n(\rho',\phi',z')\rho'd\rho'd\phi'dz'}{\left|\vec{r}-\vec{r}'\right|}-\tilde{E}z. \quad (9)$$

For a disk-shaped particle:

$$U_{disk}(\rho,z)=-\frac{\tilde{Q}}{\sqrt{a^2-c^2}}\operatorname{arctg}\sqrt{\frac{a^2-c^2}{\xi+c^2}}+$$

$$+\iiint\limits_{V_{syst}}\frac{n(\rho',\phi',z')\rho'd\rho'd\phi'dz'}{\left|\vec{r}-\vec{r}'\right|}-\tilde{E}z. \quad (10)$$

The general iterative scheme for finding a self-consistent potential is as follows:

1) The ion trajectories in the potentials are calculated one by one (4-6), and how much time each ion spent in each element of space is taken into account. There is an accumulation of statistics.

2) By the formula (7), the distribution of the space charge is determined and by the formulas (8-10) the self-consistent potential of the system is calculated, and the charge of the dust particle is adjusted from the condition that the flows of ions and electrons are equal to its surface.

3) The calculation process goes into cycles, going to step one.

The algorithm was repeated until all spatial distributions, as well as the charge of the dust particle, reached the stationary regime, that is, at the moment when any further change could be characterized as a fluctuation.

3 Results

Figure 1 compares the spatial distributions of the space charge density $n(z,\rho)$ for particles of two types: a spherical dust particle of radius $r_0 = 2\ \mu m$ and an ellipsoidal dust particle of the aspect ratio $a = 1\ \mu m$ $c = 5\ \mu m$. Comparison is made for particles of precisely this size due to the fact that the conductive particles of this shape have the same electric capacity, which for particles of different types is determined by the formulas

$$C_{el}=\frac{\sqrt{c^2-a^2}}{\operatorname{Arch}(c/a)}-\text{ellipoidal};$$

$$C_d=\frac{\sqrt{a^2-c^2}}{\arccos(c/a)}-\text{disk}-\text{like}; \quad (11)$$

$$C_s=r_0-sphere.$$

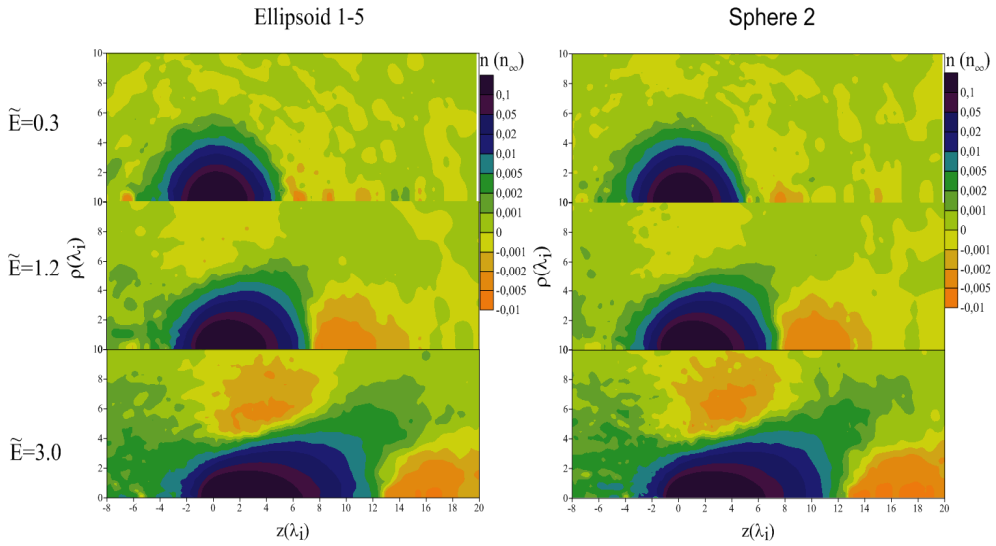

Figure 1 – The spatial distribution of the space charge density $n(z,\rho)$ for a spherical particle of radius $r_0 = 2\ \mu m$ and for an ellipsoidal particle of the aspect ratio $a = 1\ \mu m\ c = 5\ \mu m$ or various values of the external electrostatic field.

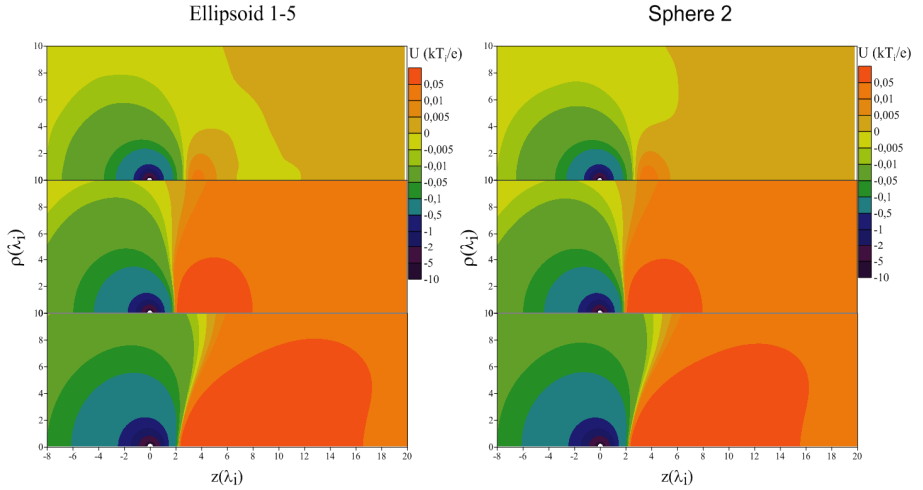

Figure 2 – The spatial distribution of electric potential $U(z,\rho)$ for a spherical particle of radius $r_0 = 2\ \mu m$ and for an ellipsoidal particle of the aspect ratio $a = 1\ \mu m\ c = 5\ \mu m$ or various values of the external electrostatic field.

A comparison of the spatial distribution of the space charge density $n(z,\rho)$ shows that the ion focusing behind the dust particle occurs in exactly the same way for particles of different types. Neither the ion cloud itself, nor the disturbances in the plasma far from the dust grain have significant differences. A similar can be observed in Figure 2, where for the same field conditions a comparison of the spatial distributions of the electric potential $U(z,\rho)$ is presented.

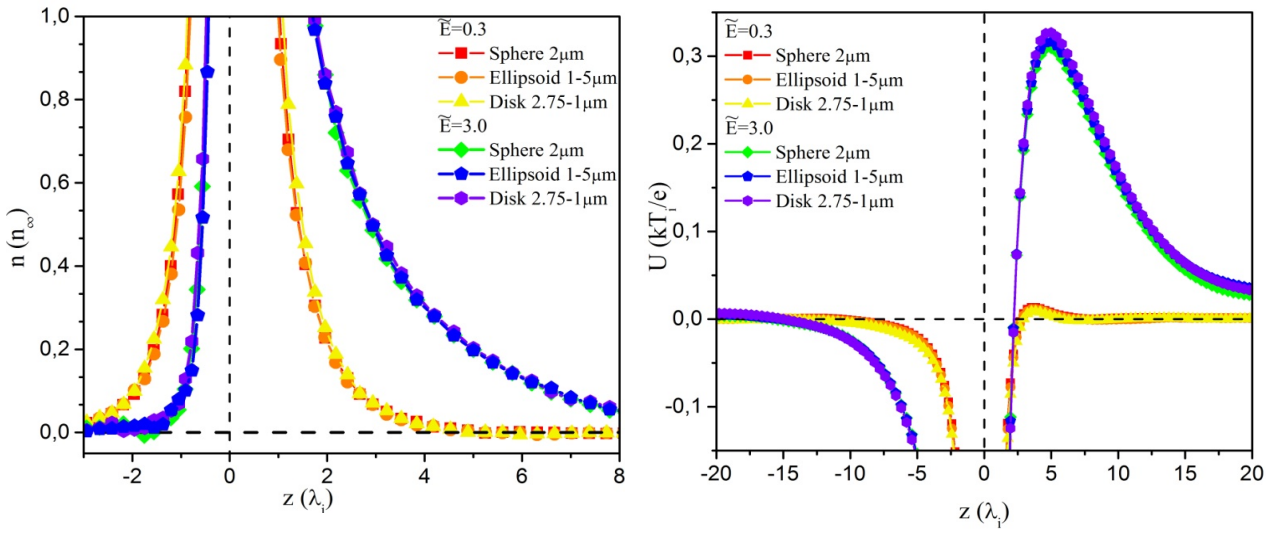

Figure 3 – The section of the spatial distribution of the space charge density $n(z,\rho=0)$ (left figure) and the potential $U(z,\rho=0)$ (right figure) for a spherical particle of radius $r_0 = 2$ *μm*, an ellipsoidal particle of the aspect ratio $a = 1$ *μm* $c = 5$ *μm* and a disk-shaped particle of the aspect ratio $a = 2.75$ *μm* $c = 1$ *μm* for various values of the external electrostatic field.

Figure 3 shows sections of the spatial distribution of the space charge density $n(z,\rho=0)$ and the potential $U(z,\rho=0)$. This representation allows comparisons for three types of particles: a sphere of radius $r_0 = 2$ *μm*, an ellipsoidal particle of the aspect ratio $a = 1$ *μm* $c = 5$ *μm* and a disk-shaped particle of the aspect ratio $a = 2.75$ *μm* $c = 1$ *μm*. All these conducting particles, when calculated by formulas (11), have the same capacitance $C = 2$. Extensive comparison of the sections of the distributions for particles of different geometries shows that in this case there are no significant differences in the distributions.

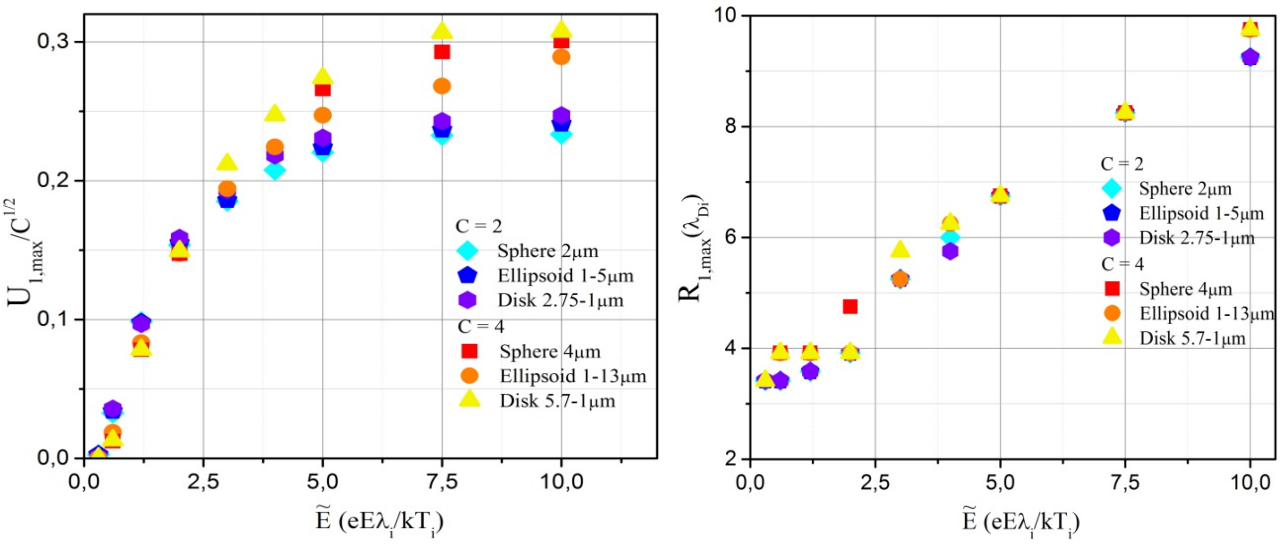

Figure 4 – The dependence of the local maximum in the potential $U_{1,max}$ (left figure) and the position of the local maximum $R_{1,max}$ (right figure) on the magnitude of the external electrostatic field for spherical particles of radii $r_0 = 2$ *μm* and 4 *μm*, ellipsoidal particles of aspect ratios $a = 1$ *μm* $c = 5$ *μm* and $a = 1$ *μm* $c = 13$ *μm*, as well as disk-shaped particles of aspect ratios $a = 2.75$ *μm* $c = 1$ *μm* and $a = 5.7$ *μm* $c = 1$ *μm*.

The data obtained in Figures 2 and 3 can be systematized, thus obtaining the dependence of the main characteristics of the wake (its maximum value and the location of this maximum) on the external field. Such dependences for particles of three grades are presented in Figure 4. Here, the comparison was expanded and dust particles with capacities equal to $C = 4$, that is, spheres of radius $r_0 = 4$ μm, an ellipsoidal particle of aspect ratio $a = 1$ μm $c = 13$ μm and a disk-shaped particle of the aspect ratio a $a = 5.7$ μm $c = 1$ μm were included in the comparison. The maximum of the wake in this case is normalized to the root of the electric capacity $\sqrt{C}$, which allows us to exclude the dependence of the wake characteristics on the dust particle charge. A similar normalization for spherical particles was considered in [19].

From this graph it can be established that there are no significant differences in the dependences of the wake characteristics on the external field for particles of different types. Thus, the approximation previously presented in [19] can be expanded:

$$U_{1,\max} = A_U \widetilde{E} \sqrt{Cl_i} (1 + (\widetilde{E} / B_U)^2)^{-\gamma}. \quad (12)$$

Where $A_U = 0.028 \pm 0.0056$, $B_U = 0.35 \pm 0.02$, $\gamma = 0{,}75$. This approximation with good accuracy allows predicting the characteristics of the wake without resorting to calculations.

4 Conclusions

The existing computational model, which was previously demonstrated in several works, was expanded by a new computational unit capable of calculating the distribution of plasma parameters (spatial distributions of space charge and potential) around dust particles of non-spherical shape: elongated and oblate ellipsoids of revolution. In this model, the figures in the computational domain are oriented so that cylindrical symmetry is preserved in the computational area.

A new block of the computational model carried out a numerical study of the wake formation behind dust particles of different geometries and examined the main characteristics of this wake - the magnitude of its first positive maximum and its location relatively to the dust particle.

The calculation of the spatial distributions of the space charge and the plasma potential near the dust particle for conducting spherical, ellipsoidal, and disk-shaped dust grains of the same electric capacity at different values of the external electrostatic field showed that when dust particles are of the same electric capacity but are of different geometry are placed in a low-temperature plasma, the formation of a wake and ion focusing for such particles are identical. A more detailed examination of these spatial distributions (sections passing through the dust particle) also did not show significant differences.

As a result of multiple calculations, general dependences of the wake characteristics on the magnitude of the external electrostatic field for dust particles of various shapes were constructed. When normalizing the dependence of the wake maximum on the root of the electric capacity, all data are described with good accuracy by a single parametric curve, which allows one to predict the plasma parameters around the dust particle without resorting to direct calculations.

References

1. Hutchinson, I. H. (2002) Plasma Phys. Control. Fusion, 44, 9, 1953.
2. Melzer, A., Schweigert, V.A., Schweigert, I.V., Homann, A., Peters, S., and Piel, A. (1996) Structure and stability of the plasma crystal. Phys. Rev. E, 54, 1, R46-R49.
3. Melzer, A., Trottenberg, T., and Piel, A. (1994) Experimental determination of the charge on dust particles forming Coulomb lattices. Phys. Lett. A, 191, 34, 301-308.
4. Winske, D. (2001) Nonlinear wake potential in a dusty plasma. IEEE Trans. Plasma Sci., 29, 2, 191-197.
5. Khrapak, S.and Morfill, G. (2009) Basic Processes in Complex (Dusty) Plasmas: Charging, Interactions, and Ion Drag Force. Contrib. Plasma Phys., 49, 148-168.
6. Verheest, F. (2000) Waves in Dusty Space Plasmas. Kluwer Academic, Dordrecht.
7. Zhukhovitskii, D.I., Fortov, V.E., et al (2012) Nonviscous motion of a slow particle in a dust crystal under microgravity conditions. Physical Review E 86, 1, 016401.
8. Vladimirov, S.V., Maiorov, S.A., Cramer, N.F. (2003) Kinetics of plasma flowing around two stationary dust grains. Phys. Rev. E., 67, 016407.

9. Dewar, R.L. and Leykam, D. (2012) Dressed test particles, oscillation centres and pseudo-orbits. Plasma Phys. Control. Fusion, 54, 014002.
10. Kompaneets, R., Morfill, G.E., and Ivlev, A.V. (2016) Interparticle Attraction in 2D Complex Plasmas. Phys. Rev. Lett., 116, 125001.
11. Ludwig, P., Miloch, W.J., Kahlert, H., Bonitz, M. (2012). On the wake structure in streaming complex plasmas. New J. Phys., 14, 053016.
12. Hutchinson, I.H. (2011) Nonlinear collisionles plasma wakes of small particles. Phys. Plasmas, ,18, 032111.
13. Hutchinson, I.H. (2012) Intergrain forces in low-Mach-number plasma wakes. Phys. Rev. E, 85, 066409.
14. Lampe, M., Joyce, G., Ganguli, G., and Gavrishchaka, V. (2000) Interactions between dust grains in a dusty plasma. Phys. Plasmas, 7, 10, 3851-3861.
15. Thomas, H., Morfill, G.E., Demmel, V., Goree, J., Feuerbacher, B., Mohlmann, D. (1994) Plasma Crystal: Coulomb Crystallization in a Dusty Plasma. Phys. Rev. Lett., 73, 652.
16. Chu, J.H. and Lin, I. (1994) Direct observation of Coulomb crystals and liquids in strongly coupled rf dusty plasmas. Phys. Rev. Lett, 72, 4009.
17. Sukhinin, G. I., Fedoseev, A. V., Salnikov, M. V., et al. (2017) Plasma anisotropy around a dust particle placed in an external electric field. Phys. Rev. E., 95, 063207.
18. Sukhinin, G.I., Fedoseev, A.V., Salnikov, M.V. (2016) Polarization of a Dust Particle and Surrounded Plasma in an External Electric Field. Contrib. Plasma Phys, 56, 5, 397-402.
19. Sukhinin, G.I., Fedoseev, A.V., Salnikov, M.V. (2019) The influence of dust particle geometry on its charge and plasma potential. Contributions to Plasma Physics, 201800153.
20. Sukhinin, G.I., Fedoseev, A.V., Salnikov, M.V. (2019) Effect of ion mean free path length on plasma polarization behind a dust particle in an external electric field. Contributions to Plasma Physics, 201800152.

IRSTI 29.27.07 https://doi.org/10.26577/phst-2019-2-p6

Development of effective potentials for complex plasmas

T.S. Ramazanov , K.N. Dzhumagulova , M.T. Gabdullin ,
Zh.A. Moldabekov and T.N. Ismagambetova*

Institute of Experimental and Theoretical Physics, Al-Farabi Kazakh National University,
71, al-Farabi Ave, 050040, Almaty, Kazakhstan
**e-mail: ismagambetova@physics.kz*

In this article the review of interaction potentials for compound particles (i.e. atoms, clusters etc.) of complex plasmas that have been derived and developed by academician Fazylkhan Baimbetov and his students over the past 25 years is given. Complex plasmas such us dense non-ideal plasmas, partially ionized plasmas, dusty plasmas are considered. We consider effective interaction potentials for classical non-ideal plasmas, semiclassical weakly coupled plasmas, and quantum plasmas. The effective potentials include relevant effects of non-idelaity and quantum degeneracy. These effective potentials are for equilibrium and stationary out-of equilibrium state of plasmas. In the latter case, the effect of dynamical screening resulting in oscillatory pattern of the potential due to formation of the wakefield considered in both classical and quantum plasmas is taken into account. There appears anomalous behavior of the wakefield in quantum plasmas. Atoms and dust particles are considered to be compound particles with allowance for polarization, i.e acquiring a dipole moment. The screening of the field of such dipoles are considered making use the multipole expansion of the screened Coulomb potential. Additionally, the discussion of these results comparing to works of researchers from elsewhere is presented. The further development of the effective potential theory should determine what effect the plasma streaming will have on transport properties such as viscosity and diffusion of non-ideal plasmas.

Key words: effective potentials, pseudopotential model, polarization effect, complex plasma.
PACS numbers: 52.27.Lw, 52.65.−y

1 Introduction

Over the last several decades, researchers from various countries have shown increased interest in non-ideal plasmas; where the latter is characterized by importance of interparticle interactions. Initially, interest in non-ideal plasmas was due to the nuclear defense projects in several countries. Later, the research in non-ideal plasmas has been continuously fueled by the national ignition campaign in the US as well as other technological applications, such as pulsed MHD generators, rocket engines with a gas-phase reactor and plasmatrons. Nowadays, the interest in non-ideal plasmas is boosted by the laser-plasma experiments allowing to study the extreme state of matter in laboratory. This paves the way to investigate the properties of state of matter in various astrophysical objects (white dwarfs, giant planets etc.) in unprecedented details.

Besides that, large variety of scientific and technological problems is associated with strongly coupled dusty plasmas. For an adequate study of the properties of plasmas of such complex composition as dusty plasmas and non-ideal plasmas in general, it is of utmost importance to know the interaction potentials of the components of the system. The important physical effects that we should be taken into account are collective effects (higher-order correlations, screening, the interaction of a large number of particles, etc.) and quantum-mechanical effects (diffraction, symmetry, etc.).

2 Pseudopotential models of the interaction of particles of classical non-ideal plasmas

In plasmas, it is necessary to take into account the effects associated with the simultaneous interaction of a large number of charged particles due to long-range nature of the Coulomb interaction. As was expressed in F. Baimbetov's doctoral dissertation [1], higher order correlations can be taken into account not only in the particle

distribution functions, but also in the potential of their interaction. As it is known, taking into account pair correlations in a rarefied system leads to the well-known Debye-Hückel potential. With increasing density, the average distance between particles decreases. In this case, the particles spend more and more time interacting with each other (the Klimontovich "delay" effect), the average particle interaction energy increases and the plasma properties can no longer be described in terms of pair correlations. Under these conditions, higher order correlations at large and quantum effects at small distances can be taken into account in the potential of interparticle interactions.

2.1 The equation for the effective potential (pseudopotential) of dense plasmas [2,3]

As already noted, in highly ionized plasmas at large distances between particles the interparticle interaction potential is different from the Coulomb interaction due to the effect of screening. In this regard, a method of computing a potential that takes into account collective (correlation) effects at large distances it is of great interest. The Bogolyubov chain for the equilibrium distribution functions [4] was taken as such a method and an equation for the effective potential (pseudopotential) was obtained on its basis $\tilde{\Phi}_{qk}$, taking into account the simultaneous correlation of particles in the framework of pair additivity [3]:

$$\Delta_i \sum_{j=1}^{S}{}' \tilde{\Phi}_{qk} = -4\pi \sum_{j=1}^{S}{}' \delta({}^k\vec{r}_j - {}^q\vec{r}_i) e_k e_q + \\ + \sum_{j=s+1}^{N} A_k \int (\Delta_i \Phi_{ij}) \exp\left\{ -\frac{\tilde{\Phi}_{qk}({}^q\vec{r}_{i,}\, {}^k\vec{r}_j)}{\Theta} \right\} \\ \nabla_j \exp\left[-\frac{\sum_{l=1}^{S}{}' \tilde{\Phi}_{qk}}{\Theta} \right] d^k\vec{r}_j \tag{1}$$

here Φ_{ij} is the microscopic Coulomb potential, $\Theta = k_B T$ and q,k are the types of particles. In the approximation of pair correlations ($S = 2$), equation (1) leads to the Debye-Hückel potential as expected. In the three-particle correlations approximation, after symmetrizing and integrating the individual terms in (1), we have [3]:

$$\Delta\Psi = \Psi \pm \Psi^2 \tag{2}$$

where $\Psi(R)$ is the effective potential in units of; $\Theta = k_B T$, $R = r / r_D$; r_D – Debye radius; Δ – Laplace operator. The minus sign corresponds to the interaction of the likewise charges, and the plus sign corresponds to the interaction of oppositely charged plasma particles.

2.2 Classical dense plasma model

To build a model of classical dense plasmas, it is necessary to take into account that

at small distances, the interaction between particles is described by the Coulomb potential, and at large distances it is equal to zero:

$$\frac{d^2\phi}{dr^2} + \frac{2}{r}\frac{d\phi}{dr} - \frac{\phi}{r_D^2} = \pm \frac{\phi^2}{r_D^2 k_B T}, \\ \phi(r \to 0) = \phi_{coul}, \quad \phi(r \to \infty) = 0 \tag{3}$$

here $\varphi = \Psi \cdot \Theta$

The boundary value problem (3) is nonlinear; therefore, it is solved numerically. However, in a fairly wide range of the parameter, the numerical solution (3) is approximated with a high degree of accuracy by the following interpolation formula [3,5]:

$$\Psi(R) = \frac{\gamma}{R} e^{-R} \frac{1 + \frac{\gamma}{2} f(R)}{1 + c(\gamma)}. \tag{4}$$

where $f(R) = (e^{-\sqrt{\gamma}R - 1} - 1)(1 - e^{-2R}) / 5$ and $c(\gamma)$ -a coefficient that depends on γ.

2.3 Weakly coupled plasma model

At parameters of weakly coupled classical plasmas, i.e. when, $\gamma = (Ze)^2 / r_D k_B T < 1$ for problem (3), we can construct an asymptotic expansion [6]:

$$\Psi(R) = \gamma[1 + \frac{\gamma}{2}\{(Ei(-R_0) - Ei(-R)) - \\ -(Ei(-3R_0)e^{2R_0} - Ei(-3R)e^{2R})\}]\frac{e^{-R}}{R} \tag{5}$$

Here $Ei(x)$ – integral exponential function, R_0 – the distance of closest approach of the particles.

3 Effective potentials for semiclassical plasmas

The inclusion of quantum effects in the interaction of charged particles allows us to solve the problem of divergence at small distances. By defining the quantum mechanical Sleter sum of particles interacting via Coulomb potential and comparing it with the classical Boltzmann factor, an analytical expression for the potential was obtained in [7,8]:

$$\varphi_{ab} = \frac{e^2}{r}\left(1-\exp(-\frac{r}{\lambda_{ab}})\right)+ \\ +\delta_{ae}\delta_{be}k_B T\ln 2\exp(-\frac{r^2}{\lambda^2_{ee}\pi\ln 2}) \quad (6)$$

where $\lambda_{ab} = \hbar/(2\pi\mu_{ab}k_B T)^{1/2}\delta_{ae}$ — de Broglie wavelength, μ_{ab} - reduced mass of interacting particles, $\hbar$ - Planck's constant.

Potential (6) is widely known as the Deutsch potential and is used to study the physical properties of a semiclassical plasma. It should be noted that this potential takes into account only quantum effects of diffraction and symmetry, but does not take into account collective effects (for example, screening). Therefore, there is a need to obtain an effective interaction potential of particles of a dense quasiclassical plasma that takes into account both of the above effects.

In Ref. [9], pseudopotentials of the interaction of charged particles were obtained, which take into account the quantum-mechanical effects of diffraction at short distances and the effects of screening of the field at large distances. For this purpose, the dielectric response functions were used. To take into account quantum effects, the Deutsch potential with the diffraction part was used as the interaction micropotential [7]:

$$\varphi_{ab} = \frac{e^2}{r}\left(1-\exp(-\frac{r}{\lambda_{ab}})\right) \quad (7)$$

and Coulomb potential was used as the micropotential of ion interaction.

The analytical expression for the electron-electron and electron-ion potential has the following form:

$$\Phi_{\alpha\beta} = \frac{Z_\alpha Z_\beta e^2}{\sqrt{1-4\lambda^2_{\alpha\beta}/r_D^2}}\left(\frac{e^{-Br}}{r}-\frac{e^{-Ar}}{r}\right). \quad (8)$$

where $A^2 = \frac{1}{2\lambda^2_{\alpha\beta}}(1+\sqrt{1-\lambda^2_{\alpha\beta}/r_D^2})$ and.

$B^2 = \frac{1}{2\lambda^2_{\alpha\beta}}(1-\sqrt{1-\lambda^2_{\alpha\beta}/r_D^2})$

An expression was also obtained for the effective potential of ion-ion interaction [10, 11]:

$$\Phi_{ii}(r) = \frac{Z_i Z_i e^2}{\sqrt{1-4\lambda^2_{ei}/r_D^2}}\left(C_1\frac{e^{-Br}}{r}-C_2\frac{e^{-Ar}}{r}\right), \quad (9)$$

where

$$C_1 = \frac{1}{2}(1+\sqrt{1-\lambda^2_{ei}/r_D^2}),$$

$$C_2 = \frac{1}{2}(1-\sqrt{1-\lambda^2_{ei}/r_D^2})$$

The obtained effective potentials (8) and (9) are valid in the region of weakly degenerate plasma. These potentials were used in analytical calculations and computer simulations of the properties of a strongly coupled semiclassical plasma.

4 Effective interparticle interaction potentials of partially-ionized dense plasmas taking into account polarization effects

As the micropotential of interaction for electron – electron in the first case, as well as for electron-dipole, dipole-dipole pairs, in the second case, we take the Deutsch micropotential (7). Consider a system of electrons and dipoles. A set of microscopic potentials is as follows:

$$\varphi_{ee} = \frac{e^2}{r}\left(1-\exp(-\frac{r}{\lambda})\right) \quad (10)$$

$$\varphi_{es} = -\frac{eQ_s(\nabla)}{r}, \quad (11)$$

$$\varphi_{ss} = -\frac{(Q_s(\nabla))^2}{r}, \quad (12)$$

where– $\lambda\!\!\!^{-} = \hbar / \sqrt{(2\pi m_e k_A T)}$ thermal de Broglie wavelength of electrons.

Using the indicated micropotentials and performing the inverse Fourier transform, we obtain the screened potential for the interaction of the electron – atom pair when [12]:

$$\Psi_{es}(r) = -\frac{e(\vec{P}\vec{\nabla})}{r\sqrt{1-4k^2/m^2}} \times \times(e^{-Br}(1-\frac{B^2}{m^2}) - e^{-Ar}(1-\frac{A^2}{m^2})) \quad ; \qquad (13)$$

where

$$A^2 = \frac{1}{2\lambda\!\!\!^{-2}}(1+\sqrt{1-4\lambda\!\!\!^{-2}/r_D^2})$$

$$B^2 = \frac{1}{2\lambda\!\!\!^{-2}}(1-\sqrt{1-4\lambda\!\!\!^{-2}/r_D^2})$$

are coefficients depending plasma density and temperature.

In the limiting case $\lambda\!\!\!^{-} \ll r_D$ potential (14) transforms into the well-known interaction potential of an isolated atom and an electron:

$$\Phi_{es} = -\frac{e^2\alpha}{2r^4} \qquad (15)$$

Finally, we consider a system of electrons and dipoles with the following micropotentials for electron-electron, electron-dipole, dipole-dipole pairs:

$$\Phi_{ee} = \frac{e^2}{r}\left(1-\exp(-\frac{r}{\lambda\!\!\!^{-}})\right) \qquad (16)$$

$$\Phi_{es} = -\frac{eQ_s(\nabla)}{r}(1-e^{-r/\lambda\!\!\!^{-}}); \qquad (17)$$

$$\Phi_{ss} = \frac{(Q_s(\nabla))^2}{r} \qquad (18)$$

where it is assumed that in the interaction of an atom with an electron, diffraction effects are also taken into account. For this case, the following expression of the screened potential was obtained [12]:

$$\Psi_{es}(r) = -\frac{e^2\alpha}{2r^4\sqrt{1-4\lambda\!\!\!^{-2}/r_D^2}} \times \times(e^{-Br}(1+Br) - e^{-Ar}(1+Ar))^2 \qquad (19)$$

In the limit $\lambda\!\!\!^{-} \ll r_D$, potential (19) goes over to the following formula:

$$\Phi_{es}(r) = -\frac{e^2\alpha}{2r^4}(1-e^{r/\lambda\!\!\!^{-}}(1+\frac{r}{\lambda\!\!\!^{-}}))^2 \qquad (20)$$

This suggests that at small distances, potential (20) tends to a finite value and agrees well with the semi-empirical Buckingham potential [13].

We note that in [14, 15] an alternative approach was developed for obtaining effective potentials based on the linearized Poisson – Boltzmann equation, which follows from (1). One of the simplest options for taking into account interparticle interactions is a self-consistent chemical model, first proposed in [14]. It is entirely based on the renormalization procedure of particle interactions [15], which leads to the following generalized Poisson-Boltzmann equation for the macroscopic potential of interaction of particle species and, taking into account collective events in the medium

$$\Delta_i\Phi_{ab}(\mathbf{r}_i^a,\mathbf{r}_j^b) = \Delta_i\varphi_{ab}(\mathbf{r}_i^a,\mathbf{r}_j^b) - \sum_c \frac{n_c}{k_BT}\int \Delta_i\varphi_{ac}(\mathbf{r}_i^a,\mathbf{r}_k^b)\Phi_{cb}(\mathbf{r}_j^b,\mathbf{r}_k^c)d\mathbf{r}_k^c$$

Here $\varphi_{ab}(\mathbf{r}_i^a,\mathbf{r}_j^b)$ denotes the genuine microscopic interaction potential, $\mathbf{r}_i^a$ stands for the radius vector of the i'th particle with Δ_i being the corresponding Laplace operator and n_c signifies the number density of particles of sort c. Note that above and everywhere below the summation is implied over the repeated subscripts of particle species.

5 Semiclassical effective interaction potentials of ions in quantum plasmas [16, 17]

At high enough plasma densities, it becomes necessary to describe the system on the basis of the effective interaction potential of the ions, taking into account their wave nature (quantum diffraction effect) at small distances. Taking into account the wave nature of the ions should lead to a finite value of the effective potential at zero and would allow for

the implementation of a semiclassical description of the ionic subsystem. The effective interaction potential, taking into account the wave nature of the ion at small interparticle distances, can be obtained using the dielectric response function method:

$$\Phi_{ii}(\vec{r}) = \int \frac{\mathrm{d}^3 k}{2\pi^2} \frac{Q_i^2}{k^2 \varepsilon(\vec{k}, \omega = 0)} \exp(i\vec{k}\vec{r}), \quad (21)$$

here Q_i is the charge of the ion. For this, in equation (21), instead of the Coulomb potential, it is necessary to use a semiclassical micropotential, which has a finite value for $r = 0$, for example, the Deutsch potential (7) with a De Broglie wavelength for ions. By calculating the dielectric response function in the random phase approximation in the long-wavelength limit, we obtain the following effective semiclassical interaction potential of ions in a dense two-component plasma with degenerate electrons:

$$\Phi_{ii}(r) = \frac{Q_i^2}{r} \times [\xi \exp(-\frac{r}{\lambda_{ii}}) + \\ + \gamma \exp(-Cr) + \alpha \exp(-Ar) + \beta \exp(-Br)] \quad (22)$$

where constants $\xi, \alpha, \beta, \gamma, A, B, C$ depends on plasma parameters.

It should be noted that in the limit $\lambda_{ii} \to 0$, the effective potential (22) transforms into the Stanton and Murillo potential [18]. If we additionally neglect the gradient correction $\widetilde{a}_2 = 0$, we obtain a screened potential of the Yukawa type. The analysis showed that the effective semiclassical potential (22), which takes into account the quantum diffraction effect, has a finite value for, on the contrary, a Yukawa type potential tends to infinity as.

6 Effective interaction potentials of particles of semiclassical two-temperature plasmas

In many experiments where a dense plasma is obtained, the temperature of electrons and ions has various values for quite a long time. Thus, it is important to take into account the fact that the plasma is non-isothermal. Dense plasma means a plasma where the average interparticle distance is comparable to the thermal wavelength of de Broglie particles and there is a high probability of particle collisions with a close encounter, in which it becomes important to take into account the wave nature of the colliding particles due to quantum-mechanical effects such as diffraction and symmetry. These effects at small distances can be taken into account in the pair potential of particle interaction or micropotential. The electron-ion temperature can be expressed through the temperature of electrons and ions in the form, $T_{ei} = \sqrt{T_e T_i}$ so that $T_{\alpha\beta} = \sqrt{T_\alpha T_\beta}$ [19].

Using the method of the dielectric response function and (7) as the micropotential, we obtain the expression for the effective interaction potential of particles of a nonisothermal plasma:

$$\Phi_{\alpha\beta}(r) = \frac{Z_\alpha Z_\beta e^2}{r} \frac{1}{\gamma^2 \sqrt{1 - (2k_D / \lambda_{ee}\gamma^2)^2}} ((\frac{1/\lambda_{ee}^{\ 2} - B^2}{1 - B^2 \lambda_{\alpha\beta}^{\ 2}}) \exp(-Br) - \\ -(\frac{1/\lambda_{ee}^{\ 2} - A^2}{1 - A^2 \lambda_{\alpha\beta}^{\ 2}}) \exp(-Ar) - \frac{Z_\alpha Z_\beta e^2}{r} \frac{(1 - \delta_{\alpha\beta})}{1 + C_{\alpha\beta}} \exp(-r / \lambda_{\alpha\beta}) \quad (23)$$

here $C_{\alpha\beta} = \frac{k_D^2 \lambda_{\alpha\beta}^2 - k_i^2 \lambda_{ee}^2}{\lambda_{ee}^2 / \lambda_{\alpha\beta}^2 - 1}$.

The effective potential (23) describes the interaction for all pairs of particles of a nonisothermal plasma. From formula (23) we obtain an analytical expression for the effective potential of electron-electron interaction:

$$\Phi_{ee}(r) = \frac{e^2}{(1 + \lambda^2_{\ ee} k_i^2)\sqrt{1 - (2k_D / \lambda_{ee}\gamma^2)^2}} \times \\ \times \frac{(\exp(-Br) - rxp(Ar))}{r} \quad (24)$$

for the effective potential of ion-ion interaction:

$$\Phi_{ii}(r)=\frac{Z_iZ_ie^2}{\gamma^2\sqrt{1-(2k_D/\lambda_{ee}\gamma^2)^2}r}\times$$
$$\times(\exp(-Br)(\frac{1}{\lambda_{ee}{}^2}-B^2)- \quad (25)$$
$$-\exp(-Ar)(\frac{1}{\lambda_{ee}{}^2}-A^2))$$

Finally, for the effective potential of ion-ion interaction we have:

$$\Phi_{ei}(r)=\frac{Z_ie^2}{\lambda_{ei}{}^2\gamma^2\sqrt{1-(2k_D/\lambda_{ee}\gamma^2)^2}r}\times$$
$$\times((\frac{1/\lambda_{ee}{}^2-B^2}{1/\lambda_{ei}{}^2-B^2})\times\exp(-Br)-(\frac{1/\lambda_{ee}{}^2-A^2}{1/\lambda_{ei}{}^2-A^2})\times \quad (26)$$
$$\times\exp(-Ar)+\frac{e^2}{r}\frac{1}{1+C_{ei}}\exp(-r/\lambda_{ei})$$

The obtained potentials satisfy all limit transitions. In the absence of shielding , $k_D\to 0, k_i\to 0, k_e\to 0$ formulas (24), (25) and (26) are equal reads:

$$\Phi_{ee}(r)=\frac{e^2}{r}\left(1-\exp(-\frac{r}{\lambda_{ee}})\right),$$
$$\Phi_{ii}(r)=\frac{Z_iZ_ie^2}{r},$$
$$\Phi_{ee}=-\frac{Z_ie^2}{r}\left(1-\exp(-\frac{r}{\lambda_{ei}})\right),$$

respectively. These potentials coincides with micropotentials, which are used as initial ones. In the case $\lambda_{ee}\to 0, \lambda_{ei}\to 0$, the expression for the effective potential, formula (23) transforms into the formula for the screened Debye potential neglecting quantum effects. Under the condition $k_i\to 0$, the | effective potentials (24) – (26) are consistent with the potentials obtained in [9, 11]. Note that under the condition $4\lambda_{ee}^2k^2{}_e=1$ and $k_i=0$, the expression for the ion-ion potential takes the following simplified form:

$$\Phi_{ii}(r)=\frac{Z^2{}_ie^2}{r}(1+\frac{r}{2\sqrt{2}\lambda_{ee}})\exp\left(-\frac{r}{\sqrt{2}\lambda_{ee}}\right) \quad (27)$$

7 Effective interaction potentials of compound particles in classical plasmas [20-22]

In many practical problems, it is necessary to consider the interaction of charged particles taking into account their internal structure. Types of particles the internal structure of which is important to take into account for the correct description of the plasma, will be referred to as compound particles. For example, such particles include atoms and micro- or nano-sized dust particles of a complex plasma, which were also considered in [23–25]. Now we consider the potential energy of interaction of the one system of charges with another system of charges located at a distance R from the first (a schematic explanation is shown in Fig. 1), introducing the dipole moment $\vec{d}_2=\sum e_\alpha{}^{(2)}\vec{r}_\alpha{}^{(2)}$ and the total charge $Q_2=\sum e_\alpha{}^{(2)}$ of the second system of charges, we find:

$$\Phi=\varphi_1Q_2+grad\varphi_1\cdot\vec{d}_2 \quad (28)$$

Using Eq. (28), for system of particles interacting via Coulomb potential, we find known result:

$$\Phi=\frac{Q_1Q_2}{R}+\frac{(Q_2\vec{d}_1-Q_1\vec{d}_2)\vec{R}}{R^3}+$$
$$+\frac{(\vec{d}_1\vec{d}_2)R^2-3(\vec{d}_1\vec{R})(\vec{d}_2\vec{R})}{R^5} \quad . \quad (29)$$

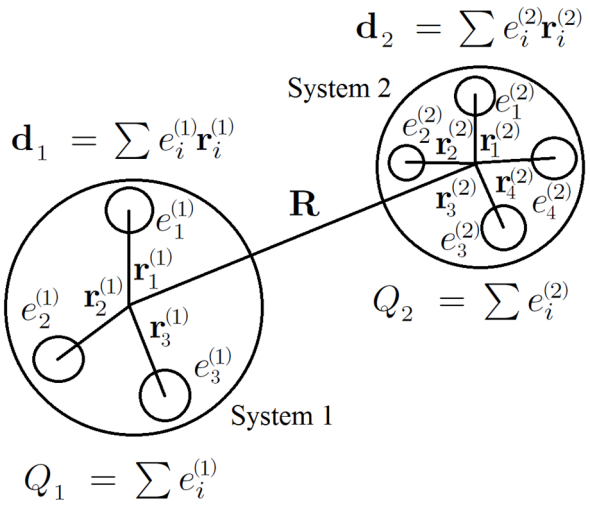

Figure 1 – Schematic explanation of the calculation of the interaction energy of two composite systems (particles)

Note that from expression (29) we can obtain all the basic formulas for potentials that are valid for various asymptotic cases [21]. We now consider the field of a composite particle in a polarizable medium. In such a medium, the field of a single charged particle is determined by a formula of the type (21). Using the methodology described above, we obtain the following expression for the effective potential:

$$\Phi = \frac{Q_1 Q_2}{R}\exp(-Rk_s) + \frac{(Q_2\vec{d}_1 - Q_1\vec{d}_2)\vec{R}}{R^3}(1+Rk_s)\exp(-Rk_s) + \\ + \frac{(\vec{d}_1\vec{d}_2)R^2 - (\vec{d}_1\vec{R})(\vec{d}_2\vec{R})(3+Rk_s) + (\vec{d}_1\vec{R})(\vec{d}_2\vec{R})Rk_s}{R^5}\exp(-Rk_s) \quad (30)$$

We consider some limiting cases of potential (30). In particular, the case when two composite particles have parallel dipole moments is of interest. For such particles from Eq.~(30) we find:

$$\Phi = \frac{Q^2}{R}\exp(-Rk_s) + \frac{d^2}{R^3}(1+Rk_s)\exp(-Rk_s) \quad (31)$$

where we set $d_1 = d_2$.

In the case when the dust particles are located along the direction of the ion flux, from equation (30) we deduce:

$$\Phi = \frac{Q^2}{R}\exp(-Rk_s) - \\ -\frac{2d^2}{R^3}(1+Rk_s + \frac{R^2k^2{}_s}{2})\exp(-Rk_s) \quad (32)$$

As can be seen from Eq. (32), at long distances, attraction between like charged particles occurs along the direction of the ion flow. This behavior of dust particles was observed in experiments on dusty plasmas in a gas discharge of direct current. Note that the oscillatory nature of the effective dipole – dipole interaction, responsible for the formation of ordered structures in a dusty plasmas, is also shown in Ref. [20].

For the case of the interaction of a charge with a dipole, we obtain:

$$\Phi_{d-ch} = \frac{Q_1\vec{d}_2\vec{R}}{R^3}(1+Rk_s)\exp(-Rk_s) \quad (33)$$

The interaction of two dipoles, , $Q_1 = Q_1 = 0, \vec{d}_1 \neq 0, \vec{d}_2 \neq 0$ is described by the following formula:

$$\Phi_{d-d} = \frac{[(\vec{d}_1\vec{d}_2)R^2 - (\vec{d}_1\vec{R})(\vec{d}_2\vec{R})(3+Rk_s)](1+Rk_s) + (\vec{d}_1\vec{R})(\vec{d}_2\vec{R})Rk_s}{R^5}\exp(-Rk_s)\,. \quad (34)$$

8 Effective interaction potentials of compound particles in quantum plasmas

As it is known, in dense plasma, when the thermal wavelength of electrons $\lambda = \hbar/(2\pi m_e k_B T)$ becomes comparable with the average interparticle distance, it is necessary to take into account the wave nature of electrons. Calculating the static dielectric function in the random phase approximation, we find the interaction energy of two composite particles in a dense plasma:

$$\Phi = \frac{Q_1Q_2}{R} f_1(R) + \frac{(Q_2\vec{d}_1 - Q_1\vec{d}_2)\vec{R}}{R^3} f_2(R) + \frac{(\vec{d}_1\vec{d}_2)R^2 f_2(R) + (\vec{d}_1\vec{R})(\vec{d}_2\vec{R}) f_3(R)}{R^5} \quad (35)$$

where for convenience the following functions are introduced:

$$f_1(R) = \frac{(\exp(-BR)(\frac{1}{\lambda_{ee}^2} - B^2) - \exp(-AR)(\frac{1}{\lambda_{ee}^2} - A^2)}{\gamma^2\sqrt{1-(2k_D/\lambda_{ee}\gamma^2)^2}} \quad (36)$$

$$f_2(R) = \frac{(\exp(-BR)(1+RB)(\frac{1}{\lambda_{ee}^2} - B^2) - \exp(-AR)(1+RA)(\frac{1}{\lambda_{ee}^2} - A^2)}{\gamma^2\sqrt{1-(2k_D/\lambda_{ee}\gamma^2)^2}} \quad (37)$$

.

$$f_3(R) = \frac{1}{\gamma^2\sqrt{1-(2k_D/\lambda_{ee}\gamma^2)^2}} \left(\begin{array}{l} \dfrac{3\exp(-BR)(1+RB)(\frac{1}{\lambda_{ee}^2} - B^2) + \exp(-BR)B^2R^2(1+RA)(\frac{1}{\lambda_{ee}^2} - B^2) -}{\gamma^2\sqrt{1-(2k_D/\lambda_{ee}\gamma^2)^2}} \\ -3\exp(-AR)(1+RA)(\frac{1}{\lambda_{ee}^2} - A^2) - \exp(-AR)A^2R^2(\frac{1}{\lambda_{ee}^2} - A^2) \end{array} \right) \quad (38)$$

Effective potential (35) at $\lambda_{ee} \to 0$ and $\lambda \to 0$ reduces to the effective potentials (30).

9 Dynamically screened potential of an ion in a stationary nonequilibrium plasma [26, 27]

It is known that often in experiments dense plasmas far from the equilibrium state are created. For instance, in experiments on the compression of matter by lasers and high-energy particle beams, a flow of particles of one type relative to particles of another type appears. In such a plasma, statically screened interaction potentials do not provide a satisfactory description. It is necessary to take into account the effect of dynamic screening. Let us consider the dynamically screened potential of an ion in a dense plasma with a density parameter $r_s \le 1$, i.e., with a density $n > 10^{24} cm^{-3}$. The electron degeneracy parameter is taken within $0.01 \le \theta \le 10$. The effects of non-ideality in the electronic subsystem are taken into account on the basis of the relationship between the collision frequency and the dielectric constant of Mermin:

$$\varepsilon_M(\vec{k},\omega) = 1 + \frac{(\omega+iv)\left[\varepsilon_{RPA}(\vec{k},\omega+iv)-1\right]}{\omega+iv\left[\varepsilon_{RPA}(\vec{k},\omega+iv)-1\right]\times\left[\varepsilon_{RPA}(\vec{k},0)-1\right]^{-1}} \tag{39}$$

Using relation (21) with dielectric function (39), dynamically screened ion-ion interaction potential in a stationary nonequilibrium plasma can be computed. A typical dynamically screened ion field is shown in Figure 2. For clarity, the "inverted" form of the potential is shown, that is, multiplied by -1. The peak in Figure 2 (minimum of potential) behind an ion, relative to the flux of electrons, corresponds to the area where ions attracts to each-other.

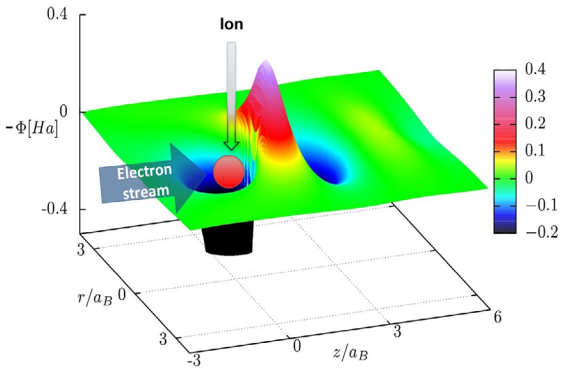

Figure 2 – Dynamically screened potential of an ion in a quantum plasma. The ion is located at the point (*r = 0; z = 0*). The electron flux is directed from left to right. For purposes of illustration, the inverse of the ion potential is shown, i.e. multiplied by -1.

10 Conclusions and Outlook

The overview of the results on the effective interaction potentials of plasma particles that have been obtained over the past 25 years by representatives of the academic school of plasma physics of academician Fazylkhan Baimbetov is given. These effective potentials have proven to provide adequate description of the various physical properties and processes occurring in a complex plasma.

Obtained effective potentials can be used for the computation of the various physical properties of plasmas. The transport properties can be found using the effective interaction potential for computation of the scattering cross section and relevant Coulomb logarithm. Furthermore, the scattering cross section can be used to compute the collision frequency and, thus, the temperature relaxation. Additionally, the knowledge of the collision frequency allows to investigate the optical properties of plasma using the relaxation time approximation for the closure of the one particle kinetic equation. Next, the effective interaction potentials can be used to compute structural properties, such as radial distribution function of particles and static structure factor, making use of the integral equations. Therefore, once radial distribution function is known, thermodynamic properties can be easily calculated.

Although non-ideal plasmas created in experiments are usually non-equilibrium, most of the works considered equilibrium non-ideal plasmas. The results on screening of the test charge in classical as well as quantum streaming plasmas clearly shows that dynamically screened potential can significantly deviate from that of in equilibrium plasmas. Therefore, it is interesting to study transport properties of particles in streaming plasmas. In other words, what is the effect of plasma streaming on such transport properties as viscosity and diffusion of non-ideal plasmas. It is anticipated that the further development of the effective potential theory should give an answer to this question.

References

1. Baimbetov, F. (1985) Transport processes and relaxation phenomena in plasma and dense gases. The dissertation for Doctoral degree in Physical and Mathematical Sciences. Tbilisi. [in russian].
2. Baimbetov, F. B., Ramazanov, T.S. (1990) Equilibrium properties of dense classical plasma. Computing Experiment Data. Thermophysics of high temperatures, 28, 3, 595-597 [in russian].
3. Baimbetov, F.B., Nurekenov, Kh.T., Ramazanov, T.S. (1995) Pseudopotential theory of classical non-ideal plasmas. Physics Letters A., 202, 211-214.
4. Bogolyubov, N. N. (1979) Problems of dynamic theory in statistical physics. M. Science. [in russian].

5. Baimbetov, F.B., Nurekenov, Kh.T., Ramazanov, T.S. (1996) Electrical conductivity and scattering sections of strongly coupled hydrogen plasmas. Physica A, **226,** 181-190.
6. Baimbetov, F. B., Dzhumagulova, K.N., Ramazanov, T.S. (1995) On the thermodynamics of weakly non-ideal plasma. Thermophysics of high temperatures, 33, 644-646 [in russian].
7. Deutsch, C., Furutani ,Y., Gombert, M.M. (1981) Nodal expansions for strongly coupled classical plasmas. Phys. Rep., 69, 85-193.
8. Minoo, H., Gombert, M.M., Deutsch, C. (1981) Temperature-dependent Coulomb interactions in hydrogenic systems. Phys. Rev. A., 23, 924.
9. Ramazanov, T.S., Dzhumagulova, K.N. (2002) Effective screened potentials of strongly coupled semiclassical plasma. Phys. Plasmas., 9, 9, 3758.
10. Ramazanov, T.S., Dzhumagulova, K.N., Gabdullin, M.T. (2006) Microscopic and thermodynamic properties of dense semiclassical partially ionized hydrogen plasma. J. Phys. A: Math. Gen., 39, 4469.
11. Ramazanov, T.S., Dzhumagulova, K.N., Gabdullin, M.T. (2010) Effective potentials for ion-ion and charge-atom interactions of dense semiclassical plasma. Phys. Plasmas, 17, 042703.
12. Ramazanov, T.S., Dzhumagulova, K.N. and Omarbakieva, Y.A. (2005) Effective polarization interaction potentials “charge-atom” for partially ionized plasma. Phys. Plasmas **12**, 9, 092702.
13. Redmer, R. (1999) Electrical conductivity of dense metal plasmas. Phys. Rev. E, 59, 1073.
14. Arkhipov, Y.V., Baimbetov, F.B., and Davletov, A.E. (2005) Ionization equilibrium and equation of state of partially ionized hydrogen plasmas: Pseudopotential approach in chemical picture. Phys. Plasmas, 12, 082701.
15. Baimbetov, F.B., Davletov, A.E., Kudyshev, Z.A., Mukhametkarimov, E.S. (2010) New Model of Dusty Plasma Particles Interaction. Contributions to Plasma Physics, 51, 6, 533–536.
16. Moldabekov, Zh., Schoof, T., Ludwig, P, Bonitz, M., and Ramazanov, T. (2015) Statically screened ion potential and Bohm potential in a quantum plasma. Phys. Plasmas, 22, 102104.
17. Moldabekov, Zh.A., Ramazanov, T.S., and Dzhumagulova, K.N. (2012) Pair Interaction Potential of Particles for Two-Component Plasma. Contrib. Plasma Phys., 52, 207-210.
18. Stanton, L.G. and Murillo, M.S. (2015) Unified description of linear screening in dense plasmas. Phys. Rev. E, 91, 033104.
19. Schoof, T., Groth, S., Vorberger, J., and Bonitz, M. (2015) Ab Initio Thermodynamic Results for the Degenerate Electron Gas at Finite Temperature, Phys. Rev. Lett., 115, 130402.
20. Ramazanov, T.S., Moldabekov, Zh.A., Dzhumagulova, K.N., and Muratov, M.M. (2011) Pseudopotentials of the particles interactions in complex plasmas. Phys. Plasmas, 18, 103705.
21. Ramazanov, T.S., Moldabekov, Zh.A., and Gabdullin, M.T. (2016) Multipole expansion in plasmas: Effective interaction potentials between compound particles. Physical Review E, 93, 053204.
22. Ramazanov, T. S., Kodanova, S.K., Daniyarov, T.T., and Moldabekov, Zh.A. (2011) Investigation an Effective Interaction Potential of Dust Particles in Nonideal Dusty Plasma. Contrib. Plasma Phys., 51, 6, 514-518.
23. Lapenta, G. (1995) Dipole moments on dust particles immersed in anistropic plasmas. Phys. Rev. Lett., 75, 4409-4412.
24. Shukla, P.K. and Eliasson, B. (2009) Colloquium: Fundamentals of dust-plasma interactions. Reviews of Modern Physics, 81, 25-44.
25. Sukhinin, G.I., and Fedoseev, A.V. (2010) Formation of a Trapped-Ion Cloud Around a Dust
26. Particle in Low-Density Plasma. IEEE Transactions on Plasma science, 38, 6, 2345-2352.
27. Moldabekov, Zh.A., Ludwig, P., Bonitz, M., and Ramazanov, T.S. (2015) Ion potential in warm dense matter: Wake effects due to streaming degenerate electrons. Phys. Rev. E, 91, 023102.
28. Moldabekov, Zh.A., Ludwig, P., Joost, J.P., Bonitz, M., Ramazanov, T.S. (2015) Dynamical Screening and Wake Effects in Classical, Quantum, and Ultrarelativistic Plasmas. Contrib. Plasma Phys., 55, 186.

IRSTI 59.45.31 https://doi.org/10.26577/phst-2019-2-p7

Thermal diagnostics of oil-filled equipment under operating voltage

B.R. Kangozhin*, S.S. Dautov, M.S. Zharmagambetova and M.A. Kosilov

Kazakh Academy of Transport and Communications named after M.Tynyshpaev,
97, Shevchenko Str.,050012, Almaty, Kazakhstan
**e-mail: almaty_bek@inbox.ru*

The article justifies the need for technical diagnostics of high-voltage insulation of electrical equipment under operating voltage. The thermal imaging monitoring method of equipment condition is considered in the document. It is shown that by means of rejection criterion ($tg\delta_{MEAS}$-$tg\delta_{PLANT}$) defects in an initial stage of development come to light. The efficiency of control of high-voltage paper-oil insulation under operating voltage has been experimentally proved. The analysis of the causes of damage to high-voltage bushings and current transformers of 500 kV, based on which it was revealed that local defects are characteristic, the development of which leads to either thermal breakdown or the appearance of partial discharges and electrical breakdown of the main insulation. Thermal imaging diagnostics of such equipment as, for example, high-voltage bushings, coupling capacitors and current transformers makes it possible to detect almost all possible defects in insulation and measure their insulation characteristics. The efficiency of thermal imaging monitoring of the state of electrical equipment under operating voltage is shown. The calculated tgδ values from thermal imaging measurements are more accurate, since the results of measurements with a thermal imager are not affected by electromagnetic interference.It has been concluded that it is possible to abandon several traditional methods of testing with shutdown and without electrical equipment.

Key words: thermal imaging control, paper-oil insulation, dielectric loss tangent, energized equipment, insulation damage, rejection criterion.
PACS numbers:

1. Introduction

The development time of most locally concentrated defects from appearance to damage of electrical insulation has not been studied and can only be estimated tentatively. But such defects are the main cause of damage to the equipment [1]. Defects cannot be ruled out. It is possible to eliminate damage of equipment by detecting and eliminating dangerous defects at an early stage of development, organizing continuous monitoring of occurrence and development of dangerous defects [2,3]. Methods of diagnostics of electrical equipment under operating voltage are required for this purpose [4].

2. Methods

By researches of paper-oil isolation with local defect, inputs and a TT, it is established if there is local defect the size tgδ depends on tension, as it must be used for timely identification of defect (Figure 1). If there is a local defect even with a strong degree of its development, when the insulation paper is charred from the heat generated in the place of the defect, the total value of the dielectric loss tangent changes slightly at measurements at UExec= 10 kV [5].

The results of insulation measurements with local defect (Figure 1.) can be calculated using the Formula [6]:

$$tg\delta = \frac{tg\delta_N \times C_N + tg\delta_Д \times C_Д}{C_N + C_Д}, \qquad (1)$$

If the following parameters for insulation parcels are specified:

$$tg\delta_N = 0{,}1\%,\ tg\delta_Д = 100\%$$

$$C_N = 0{,}999,\ C_Д = 0{,}001$$

N – insulation volume without defect;
D – volume of insulation with defect,

then calculations by Formula (1) will give the following result:

$$tg\delta = \frac{tg\delta_N \times C_N + tg\delta_Д \times C_Д}{C_N + C_Д} = 0{,}2\%$$

Other words, prior to the occurrence of the local insulation defect tgδ at 10 kV was 0.1%, and the occurrence of the highly developed defect ($tg\delta_Д$ = 100%) changed the total or measured tgδ to only 0.2%, which is within the inaccuracy and will not cause doubt in the normal insulation state [7]. However, the occurrence of a local defect with tgδ = 100% or more will lead to local intense heat generation, paper charring and the creation of a conductive channel in this zone. That means it can also lead to the classic heat breakdown. The difference between tgδ insulation with and without defect was 0.1%. Therefore, it is possible to accept the size of rejection criterion ($tg\delta_{MEAS}$-$tg\delta_{PLANT}$) considering an error of measurements more or equal to ≥ 0,3%.

$$\Delta tg\delta = tg\delta_{РАБ.} - tg\delta_{\ 10кВ} \geq 0{,}3\% \qquad (2)$$

The difference in tgδ values at two voltage levels of 0.3% or more indicates the development of a local defect, and the apparatus with such insulation should be rejected [8]. It is the difference in tgδ values at two voltage levels of 0.3% and more that should be a rejection criterion when diagnosing machines with paper-oil insulation.

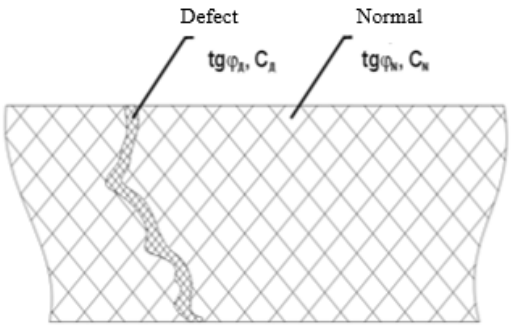

Figure 1 – Insulation area with local defect

The essence of the method is obvious from Figure 2. Measurements of tgδ value of each product concerning the object chosen for a standard are performed. The received tgδ values are the difference of $\Delta tg\delta_{MEAS}$= $tg\delta_{ИО}$- $tg\delta_{ЭТ}$ (MO – measured object, RO – reference object) which can have both positive, and negative values depending on absolute tgδ values of the compared objects. True values of $tg\delta_{ИСТ}$ of the measured object are determined by adding the following sign $\Delta tg\delta = \Delta tg\delta_{MEAS}$ with tgδ (Figure 2) obtained during measurements:

$$tg\delta_{ИСТ} = (\pm \Delta tg\delta_{MEAS}) + tg\delta_{ЭТ} \qquad (3)$$

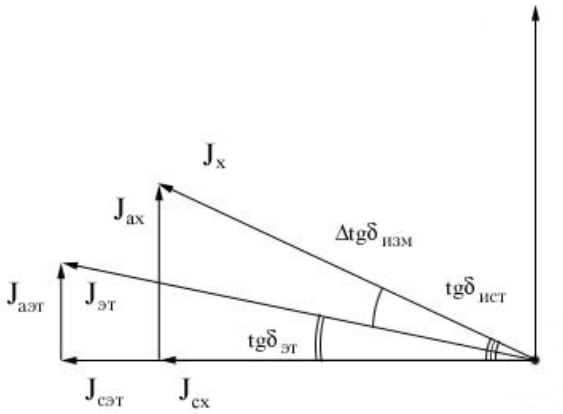

Figure 2 – The vector chart of measurements by the bridge with use of a standard with $tg\delta_{ЭТ} \neq 0\%$.

The insulation condition is evaluated by comparing the results of the first measurements with the plant measurements and the subsequent measurements with the first measurements [10]. Rejection indicator is the difference at the first measurement on $\Delta tg\delta = tg\delta_{MEAS}$-$tg\delta_{PLANT.} \geq 0{,}3\%$, and at the subsequent: $\Delta tg\delta = tg\delta_{MEAS} - tg\delta_{1\ MEAS.} \geq 0{,}3\%$.

Transformer groups input and 220-500 kV current transformers on Ekibastuz GRES-2 have paper-oil insulation (POI). Based on the analysis of the causes of damage to the inlets and TT, it was revealed that local defects are characteristic, the development of which leads to either thermal breakdown or partial discharge and electrical breakdown of the main insulation. As an axiom, it is assumed that aging of insulation leads to deterioration of its insulation characteristics. However, the operating experience shows that isolation in which there was no local defect, for example, of the moistening causing change of tgδ, the value tgδ, remains stable during all service life of the device [11].

At thermal imaging inspection of current transformer, condensers of communication, capacitive transformers of tension under the operating voltage the defects leading to increase in

the dielectric losses in isolation determined by a tangent of angle of dielectric losses (tgδ) and causing temperature increase of isolation [12,13] come to light. The temperature of the external surface of such devices should be higher than that of serviceable ones. Measurements under the operating voltage can be carried out at any ambient temperature as the difference is measured in the size tgδ of the inputs having identical dependence of tgδ=f(T). With such measurements and the use of factory measurement data as reference characteristics having the same temperature, it is not necessary to perform a temperature recalculation to the temperature of measurements at the plant to calculate the data of the measured object. This recalculation is carried out automatically as the temperature dependence of tgδ of a standard and the measured object is identical [14].

The estimation of oil-filled devices with condenser insulation is estimated by the value of the device temperature exceeding the average ambient temperature [15,16]:

$$\Delta T_i = T_i - T_0, \quad (4)$$

Where T_i – the temperature of the apparatus determined by the area of the external surface characteristic of each type of equipment; T_0 is the average ambient temperature determined for each equipment type.

Thermal imaging diagnostics of such devices as condensers of communication and transformers of current, allows not only to reveal, practically, all possible defects, but also to measure their insulating characteristics (tgδ). Recalculation of the excess of temperature of a surface of the device over ambient temperature measured by the thermal imager in value of insulating characteristic (tgδ) is made on a formula [15]:

$$tg\delta_x = \frac{tg\delta_э \times (T_x - T_0)}{(T_{эx} - T_0)}, \quad (5)$$

For recalculation the data of measurements under the operating voltage of tgδ by a bridge method of measurement (direct measurements) are used [17,18]. At measurements on temperature (indirect measurements) the device connected to any phase unlike the bridge scheme of direct measurement tgδ when the standard must be connected only to the same phase of electro installation can be taken for a standard [19]. At JSC "EGRES-2 Station" thermal imaging diagnostics of high-voltage devices 220-500kV with POI of capacitor type: current transformers, communication capacitors, high-voltage inputs were performed. By results of thermal imaging diagnostics tgδ values of all listed devices are calculated [20]. At the same time, the calculated values for thermal imaging measurements are more accurate, as the results of measurement by the thermal imager are not affected by electromagnetic interference.

3. Experiment results

Here are two examples of the thermal imaging survey results which were performed by an infrared camera ThermoPro™ by Wuhan Guide Infrared Technology Co., Ltd [19]. They show the efficiency of thermal imaging monitoring of electrical equipment under operating voltage.

Example 1. By results of measurement of temperature of a surface of TT-2 (Figure 3) calculation of tgδ of the main isolation of a TT is executed (Table1).

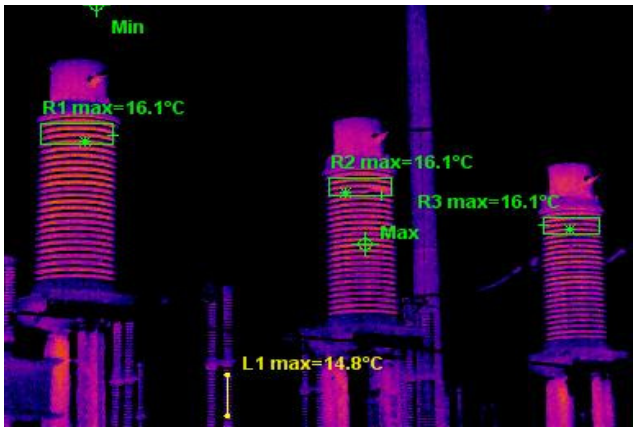

Figure 3 – Results
Thermal imaging transformers
220 kV current TT-2
Phase TT-2 thermogram C, B, A.
T_C=16,1^{0}C;
T_B=16,1^{0}C;
T_A=16,1^{0}C

Table 1 – Temperature measurements of 220 kV current transformers TT-2 by thermograms:

Transformer Phase	Tmax, ^{0}C	ΔT, ^{0}C	tgδ, % (расч.)	tgδ, % (изм.)
A	16,1^{0}C	0,00	0,32	0,35
B	16,1^{0}C	0,00	0,32	0,34
C	16,1^{0}C	0,00	0,32	0,32

Calculated values of tgδ TT-2 meet Standards and requirements of manufacturer. There are no defects that cause temperature change of 220 kV TT-2 current transformers in 220 kV current transformers TT-2 phases A, B and C. Similar results have been obtained in the diagnosis of other devices with POI.

Example 2. By results of temperature of condenser surface CC-220 PTL 2377 ODD-220 measurement (Figure 4) calculation of tgδ for elements of condensers of communication CC-220 PTL 2377 ODD-220 is executed (see Table 2).

Design values of voltage distribution and nonuniformity coefficient of communication capacitor CC-220 PTL 2377 ODD-220 do not comply with the Standards and requirements of the manufacturer. The lower element CC-220 PTL 2377 ODD-220 has a defect in the initial stage of development, the upper element has no defects which cause a change in its temperature

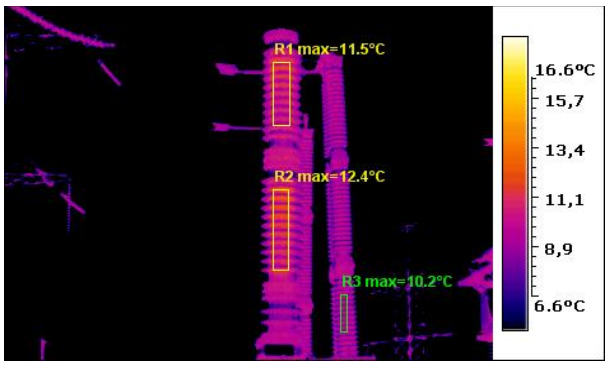

Figure 4 – The results of thermal imaging survey of CC-220 PTL 2377 ODD-220.
Thermograph CC-220 PT: 2377
ODD-220, C Phase.
T_{UP}=11,5^{0}C;
T_{DOWN}=12,4^{0}C.

Table 2 – Results of temperature measurements and voltage distribution by elements of communication capacitor CC-220 PTL 2377 ODD-220 by thermograms

Transformer Phase	Tmax, ^{0}C	ΔT, ^{0}C	U el, kV (calc.)	K_H	tgδ,% (calc.)
Up	11,5^{0}C	1,3	47,2	1,7	0,3
Down	12,4^{0}C	2,2	79,8		1,4
T_{OKP}, ^{0}C	10,2^{0}C	-	-	-	-

For a thermal imaging way of electric devices condition control dependences of tgδ on temperature by any of the known ways decide on POI. For real measurements of TT-500 kV:

- $tg\delta_{PLANT}$ values are selected according to ΔT=0°C: 0,21, 0,19, 017, 019, 0,21, 0,21, 0,21.
- $tg\delta_{PLANT}$ values are selected according to ΔT=0.1°C: 0,27, 0,27, 0,27, 0,27, 0,27.
- Max $tg\delta_{PLANT}$ values are selected according to ΔT=0°C: 0,21 and $tg\delta_{PLANT}$ values are selected according to ΔT=0,1°C: 0,27, as $tg\delta_{MEAS}$ cannot be less than $tg\delta_{PLANT}$.

The ratio is defined ΔT=0,1°C and value of tg according to:

$tg\delta_{PLANT\ 0,1°C} - tg\delta_{PLANT\ 0°C}$=0,27 -0,21=0,06, that is ΔT=0,1°C refers to tgδ=0,06%;

Then the empirical formula has the form is:

$$(tg\delta_{PLANT} \text{ for } \Delta T=0°C) + (tg\delta_{PLANT\ 0,1°C} - tg\delta_{PLANT\ 0°C})$$

or:

$$tg\delta_{PACч} = tg\delta_{PLANT\ 0°C} + 0{,}06 \cdot \Delta T\ (\%).$$

As a sample:

$$tg\delta_{PACч} = 0{,}21 + 0{,}06 \cdot \Delta T\ (\%) \qquad (6)$$

4. Discussions

The main thing when selecting the value of $tg\delta_{PLANT}$ refers to a certain ΔT is that the $tg\delta_{MEAS}$ cannot have a value less than $tg\delta_{PLANT}$. The fact that some values of $tg\delta_{PLANT}$ for $\Delta T = 0$ ° C are slightly less (in this sample 0.17 and 0.19) than the maximum value of 0.21 can be related to two circumstances:

1. The temperature measurement accuracy of the thermal gauge is $\Delta T = 0.1$ ° C, which in the example is $\Delta tg\delta = 0.06\%$. $tg\delta$ can be measured with an accuracy 0.06% and it is not possible to distinguish smaller values of $tg\delta$ (in a given sample 0.02% and 0.04%).

2. During operation there were minor changes in $tg\delta$ measured TT (0.02% and 0.04% in this sample).

5. Conclusions

1. Change of $tg\delta_{MEAS}$ concerning $tg\delta_{PLANT}$ is rejection criterion and allows to reveal existence of defect in initial extent of development. The use of the high-voltage paper-oil insulation control technique allows to eliminate all other types of tests, at least until the controlled parameters reach the limit values.

2. The thermal imaging method allows by converting the measured temperature differences into insulation characteristics (tgd), measured by direct measurement under operating voltage, to assess the condition of the object under examination, to detect defects in it and to determine the degree of their development.

3. The thermal imaging examination method allows to detect defects at an early stage of their development, as well as provides additional diagnostic criteria. In addition, this method allows the detection of defects that cannot be detected by any other test methods. Based on an analysis of the causes of damage to high-voltage bushings of transformers and current transformers, it is revealed that local defects are characteristic, the development of which leads either to thermal breakdown or to the appearance of partial discharges and electric breakdown of the main insulation.

4. Measurements under operating voltage can be performed at any ambient temperature, since the difference in the value of $tg\delta$ of inputs having the same dependence $tg\delta=f(T)$ is measured. With such measurements and using factory measurements as characteristics of a standard having the same temperature, it is not necessary to perform temperature conversion to the measurement temperature at the factory to calculate the data of the measured object. This recalculation is performed automatically, since the temperature dependence $tg\delta$ of the standard and the measured object is the same.

References

1. Statistical data on defects in high-voltage equipment at substations of JSC “FGC UES” and IDGC Holding. (2016).

2. RD 34.45-51.300-97 (1998). Electrical Equipment Test Scope and Standards. (6th ed.). Moscow: ENAS.

3. On measures to improve the reliability of hermetic bushings 110-750 kV (1988). Emergency Circular N C -06-88E. –Moscow: GN-TU USSR Ministry of Energy.

4. Polyakov V.S. (June 21-26, 2004). Principles of building an effective diagnostic system. (27th ed.). Materials of the seminar "Modern problems of production, operation and repair of transformer equipment". St. Petersburg: PEIPK, 196.

5. Polyakov V.S. (June 5-9, 2000). Analysis of the requirements of the Test Norms for the diagnosis of oil-filled equipment. (11th ed.). Materials of the seminar “Current state and problems of diagnostics of powerful power transformers and shunt reactors”. St. Petersburg: PEIPK, 387.

6. Tsirel Ya.A., Polyakov V.S., Smerling L.A.. Measurement of dielectric losses of high voltage inputs under operating voltage. (1975). Journal of Power Stations, 2.

7. Polyakov V.S. (June 25-29, 2004). Analysis of measurement schemes of insulation characteristics of high-voltage bushings and current transformers under operating voltage. (16th ed.). Materials of the seminar "Modern problems of operation of high-voltage oil-filled equipment". St. Petersburg: PEIPK, 194.

8. Polyakov V.S., Utegulov N.I. System for continuous monitoring of the isolation of high-voltage electrical equipment. (2009). Bulletin of the Almaty Institute of Energy and Communications (AIEIS), 3, 4-10.

9. RD 34.20.501-95. (2000). Rules for the technical operation of power plants and networks.(15th ed.). St. Petersburg: Dean, 352.

10. Monastyrskyi A.E. Insulation monitoring system for SKIT transformers. (2001). Journal of Technical description and operating manual. St. Petersburg: LLC Dizkon.

11. Ya.A. Tsirel, V.S. Polyakov, L.A. Smerling. Measurement of dielectric losses of high-voltage bushings under operating voltage. (1975). Journal of Electric Stations, 2.

12. Polyakov V.S. The use of infrared technology to detect defects in high-voltage equipment. (1985). Journal of Energy and Electrification. Series: Operation and repair of electrical networks. Express information. Moscow: SPO Soyuztekhenergo, 7.

13. Polyakov V.S. The use of thermal imaging detectors for detecting defects in high-voltage equipment. (1990). Methodological instructions for monitoring equipment with thermal imaging devices. Leningrad: LIPKEN, 57.

14. Afonin A.V., Polyakov V.S., et al. Infrared thermography in power engineering. (2000) Fundamentals of infrared thermography. Vol. 1. St. Petersburg: PEIPK.

15. RD 153-34.0-20.363-99. Basic provisions of infrared diagnostics of electrical equipment и AL (ORGRES).

16. RD EO-0188-00. Guidelines for the diagnosis of electrical apparatus of switchgear of power plants and substations. (1999). Section 2: “Thermal imaging control of switchgear devices”. Rosenergoatom Concern. Ministry of the Russian Federation for Atomic Energy. Moscow.

17. Vorobyov S.A. Electrical measurements of non-electrical quantities. (1975). Vol. 2. The fundamentals of the theory and calculation of unbalanced bridge circuits of the resistance-sensor. Sverdlovsk: UPI after named C.M. Kirova, 232.

18. Swee P.M. Methods and diagnostic tools for high voltage equipment. (2012). Moscow: Energoatomizdat, 240.

19. Vavilov V.P. Infrared thermographic diagnostics in construction and power engineering. (2014). Moscow: Energoprogress, 186.

20. Ekibastuz Report № 01-05-1067-0015 «System of diagnostics of electrical equipment of JSC "Ekibastuz Station GRES-2». 2011.

IRSTI 58.33.37 https://doi.org/10.26577/phst-2019-2-p8

Feasibility study of Tritium recoil barrier for neutron reflectors

E.Ishitsuka[1] and N.Sakamoto[2]

[1]Sector of Fast Reactor and Advanced Reactor Research and Development, Japan Atomic Energy Agency (JAEA), 4002 Narita-cho, Oarai-machi, Higashi Ibaraki-gun, Ibaraki-ken, 311-1393, Japan
[2]NGK Insulators, Ltd., 2-56, Suda-cho, Mizuho, Nagoya 467-8530, Japan
e-mail : ishitsuka.etsuo@jaea.go.jp

Tritium release into the primary coolant of the research and test reactors during operation had been studied, and it is found that the beryllium components used as a neutron reflector in the core strongly affect the tritium release into the primary coolant, and it is also found the recoil release from chain reaction of ^{9}Be is dominant. To reduce tritium concentration of the primary coolant, feasibility study of the tritium recoil barrier for the beryllium neutron reflectors was carried out, and the tritium recoils of various materials such as Al, Ti, V, Ni, Zr, etc., were calculated by PHITS. From these calculation results, it is clear that the thickness of tritium recoil barrier depends on the material and 20-40 μm is required for three orders reduction. Additionally, the denser materials have shorter recoil length in general, however, it is clear that the recoil lengths of Zr and Pb are similar with Ti.

Key words: primary coolant, tritium release, research and test reactors, beryllium, neutron reflectors, tritium recoil barrier.
PACS numbers: 28.50.Dr, 28.41.Bm.

1 Introduction

Tritium release into the primary coolant during operation of the JMTR (Japan Materials Testing Reactor) and the JRR-3M (Japan Research Reactor-3M) had been studied [1-9], and it is clear that the beryllium components used as a neutron reflector [10] in the core strongly affect the tritium release into the primary coolant. The sources and mechanisms for the tritium release into the primary coolant are evaluated by calculations of the MCNP [11], PHITS [12] and ORIGEN2 [13,14], and it is found that the recoil release [15,16] from chain reaction of ^{9}Be is dominant [17].

These studies show that the prevention of recoil release from beryllium is most effective to reduce the tritium release into the primary coolant. To prevent tritium recoil release, the surface area of beryllium neutron reflectors needs to be minimum in the core design and/or shielded with other material. In this paper, as the feasibility study of the tritium recoil barrier for the beryllium neutron reflectors, the tritium recoils of various materials were calculated.

2 Calculations of tritium recoil

Al, Ti, V, Ni and Zr shown in Table 1 are selected as the candidate materials from the viewpoint of low activation materials and forming intermetallic compound with beryllium [18]. The formation of the intermetallic compound considered that will prevent troubles such as peeling during the reactor operation. H_2O and Pb are selected as the reference materials.

The calculations of tritium recoil lengths were carried out by PHITS(Ver. 3.170) [12]. The calculation model for Al is shown in Figure 1. The tritium recoil was directly calculated using a triton (same meaning with tritium in this paper) source without the calculation of nuclear reactions [7], and small beryllium sphere is used in this model to get enough triton density even if short calculation time. The triton monochromatic energy (2.73MeV) of $^{6}Li(n_t,\alpha)^{3}H$ reaction is used in these calculations [7]. The material densities are used from reference [19,20]. 10^{9} triton particles were generated in this calculation, and results are shown in Figure 2~ Figure 4.

2D distribution of triton flux is shown in Figure 2, and enlarged view near boundary is shown in Figure 3. 1D distribution of triton flux near boundary is shown in Figure 4. It is clear from this calculation that the recoiled triton reached to about 40μm in Al from the boundary.

Similar calculations were carried out with different materials shown in Table 1 which surrounding beryllium sphere. Calculation results of the triton recoil length in various materials are shown in Figure 5. From these calculation results, the recoil barrier thickness that reduced to 1/1000 are estimated, and shown in Table 1.

* : Thickness reduced to 1/1000

Table 1 – Density and recoil protetion thickness

Materials	Density (g/cm^3)	Recoil barrier thickness* (μm)
H_2O	0.99	59
Al	2.7	35
Ti	4.5	25
V	5.87	19
Ni	8.8	16
Zr	6.49	23
Pb	11.34	25

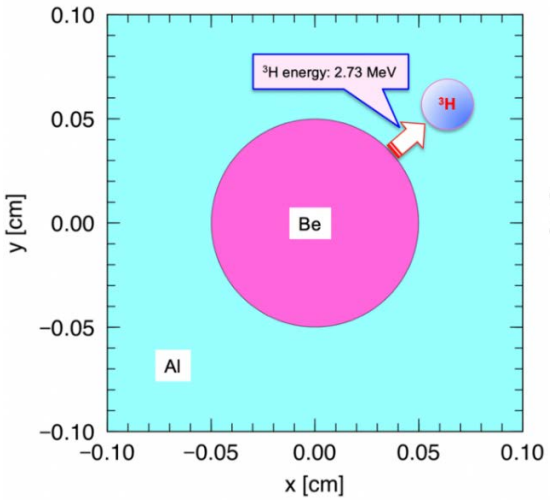

Figure 1 – Calculation model for Al

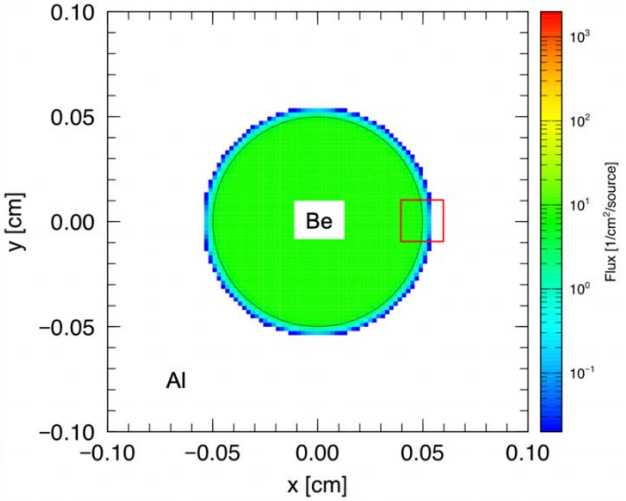

Figure 2 –2D distribution of triton flux

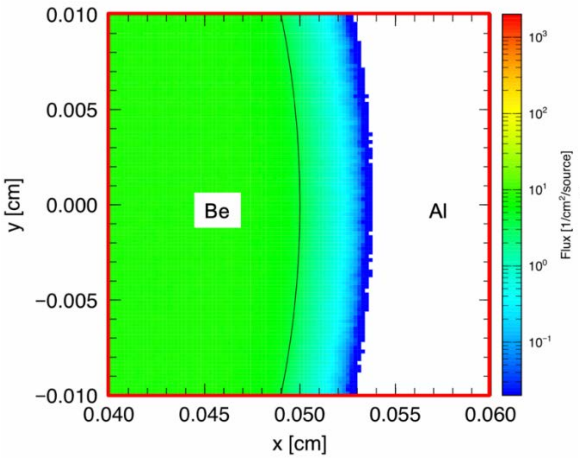

Figure 3 –2D distribution of triton flux near boundar

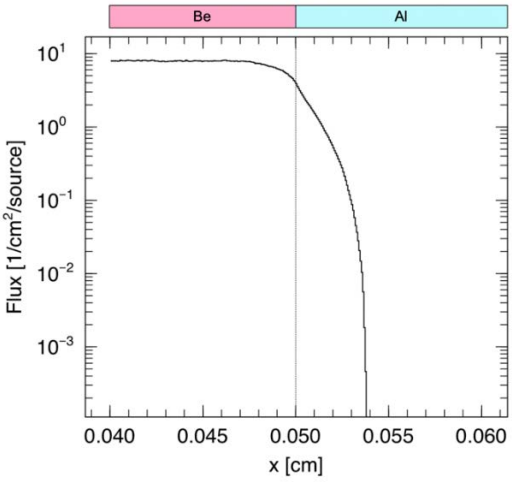

Figure 4 – 1D distribution of triton flux near boundary

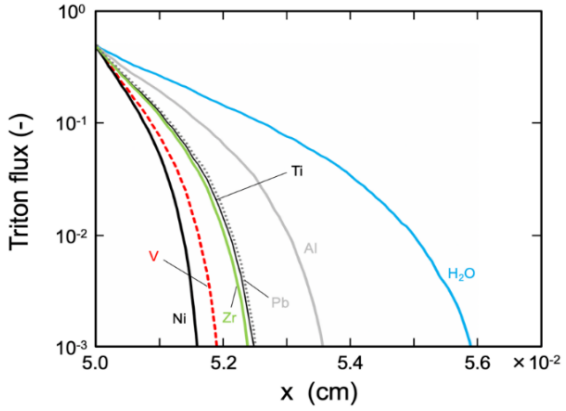

Figure 5 – Triton recoil lengths in various materials

3 Discussion

The denser materials have shorter recoil length in general, however, the triton recoil lengths of Zr and Pb are similar with Ti in these calculations. The tritium recoil release can be reduced by increasing the thickness of barrier. However, the tritium concentration in the primary coolant cannot be reduced to zero because tritium is also generated from the primary coolant. The tritium recoil release from beryllium is reported three orders of magnitude larger than that of the generated tritium from the primary coolant [17]. Therefore, the reduction performance of three orders of magnitude is sufficient as the tritium recoil barrier.

From the above calculation results, it is clear that the thickness of tritium recoil barrier depends on the material and 20-40 μm is required. As a next development step, the selection of materials in consideration of activation, the construction methods for the tritium recoil barrier, the stability under neutron irradiation, etc., will be listed.

4 Conclusions

As the feasibility study of tritium recoil barrier for the beryllium neutron reflectors, the tritium recoils of various materials were calculated, and the following results were obtained.

- The reduction performance of three orders of magnitude is sufficient as the tritium recoil barrier.
- The thickness of tritium recoil barrier depends on the material and 20-40 μm is required.

References

1. Terunuma, N., Nagao, Y., Yokouchi, I., & Sato, M. (2007). Concentration of Radio Active Elements in Primary Cooling Water at Reactor Operation of JMTR. JAEA-Review 2007- 034.
2. Department of Research Reactor. (1992). Annual Report of Department of Research Reactor, 1991 (April 1, 1991~March 31, 1992). JAERI-M 92-154.
3. Ishitsuka, E., Motohashi, J., Hanawa, Y., Komeda, M., Watahiki, S., Mukanova, A., Kenzhina, I., & Chikhray. Y. (2014). Study of Origin on Tritium Release into Primary Coolant for Research and Testing Reactors, -Tritium Release Rate Evaluated from JMTR, JRR-3M and JRR-4 Operation Data-. JAEA-Technology 2014-025.
4. Ishitsuka, E., Kawamura, H., Sugai, H., Tanase, M., & Nakata. H. (1990). Experiments on Tritium Behavior in Beryllium (2), - Tritium Released by Recoil and Diffusion-. JAERI-M 90-013.
5. Shimakawa, S., Ishitsuka, E., & Saito, M. (1992). HEINBE, The calculation program for Helium production in Beryllium under neutron Iirradiation. JAERI-M 92-174.
6. Kenzhina, I. et al. (2016). Evaluation of Curve for Tritium Release Rate into Primary Coolant of Research and Testing Reactors. 4th Asian Symposium on Material Testing Reactors, Hanoi, Vietnam, 3-4 March 2016.
7. Ishitsuka, E., Kenzhina, I., Okumura, K., Takemoto, N., & Chikhray, Y. (2016). Calculation by PHITS Code for Recoil Tritium Release Rate from Beryllium under Neutron Irradiation. JAEA-Technology 2016-022.
8. Sezaki, K., Takeda, K., Sakurai, F., Komukai, B., & Kondo, I. (1976). Correspondence between JMTR and JMTRC (No. 34 operation cycle) . JAERI-M-6686.
9. Ho H.Q., E. Ishitsuka. (2018). Calculation of tritium release from driver fuels into primary coolant of research reactors. Phys. Sci. Technol, 5 (2), 53-56.
10. Stonehouse, A.J. (1986). Physics and chemistry of beryllium. J.Vac.Sci.Technol, A3(3), 1163-1170.
11. Goorley, T. et al. (2012). Initial MCNP6 Release Overview. Nuclear Technology, 180-3: 298-315.
12. Sato, T., Niita, K., Matsuda, N., Hashimoto, S., Iwamoto, Y., Noda, S., Ogawa, T., Iwase, H., Nakashima, H., Fukahori, T., Okumura, K., Kai, T., Chiba, S., Furuta, T. & Sihver, L. (2013). Particle and Heavy Ion Transport Code System PHITS, Version 2.52. J. Nucl. Sci. Technol, 50:9, 913-923.

13. Suyama K. (2006). ORIGEN2.2-UPJ: A complete package of ORIGEN2 libraries based on JENDL-3.2 and JENDL-3.3. OECD NEA Data Bank: NEA-1642.
14. Okumura K, Sugino K, Kojima K, Jin T, Okamoto T, & Katakura J. (2012). A set of ORIGEN2 cross section libraries based on JENDL-4.0: ORLIBJ40. JAEA-Data/Code 2012-032.
15. Ward, J.C. (1961). Radioactivity of Nuclear Reactor Cooling Fluids, ORNL-3152.
16. Schmitt, R.A., & Sharp, R.A. (1958). Measurement of the range of recoil atoms. Third-Annual Radiation Effects Symposium, III (October, 1958).
17. Ishitsuka, E., Kenzhina, I., Okumura, K., Ho Hai Quan, Takemoto, N., & Chikhray, Y. (2018). Calculations of tritium recoil release from Li and U impurities in neutron reflectors. JAEA-Technology 2018-010.
18. Webster, D., & London, G.J. (1979). Beryllium Science and Technology, vol.1.
19. Table of Isotopes, 7th ed. (1978). Joho Wiley & Sons. Inc.
20. Murakami, S., et.al. (Eds.), (1982). Radiation data book. Chijinsyokan (in Japanese).

IRSTI 29.19.16 https://doi.org/10.26577/phst-2019-2-p9

Influence of Cu impurities and surface temperature to the formation of thin a-C:H(Me) film

Z. Rutkuniene

Kaunas University of Technology, Physics department, Studentu 50, LT 51368, Kaunas, Lithuania, e-mail: zivile.rutkuniene@ktu.lt

The aim of this experimental work is identify most important physical and chemical processes on the surface during amorphous carbon films formation on the silicon surface with copper nanoclusters (Cu). Duration of films deposition on n type silicon (100) surface by using different substrate temperatures (25 °C, 100 ^{oC} and 250 °C) was 45s. Velocity of film growth from C_2H_2 gas plasma depended on surface temperature and was variable (0.2-0.5 nm/s). Data of null ellipsometry, Raman spectroscopy and element analysis showed that formation of amorphous carbon film is in the early stage and mixture of Si-C, Si-COH and GLC fragments is dominant on the surface. The experimental RS curves were fitted by few Gaussian-shape lines in the spectral range from 500 cm^{-1} to 700 cm^{-1}, from 700 cm^{-1} to 900 cm^{-1}, from 900 cm^{-1} to 1100 cm^{-1} and from 1100 cm^{-1} to 1900 cm^{-1} and analysis of the additional peaks in all ranges confirmed complexes of different carbons structures in the film. Carbon films with more ordered C-C bonds grows during film formation at higher temperatures (>100^{o} C) on the silicon surface with Cu particles, because atoms of copper penetrate into the deeper layers of silicon. The substrate temperature influenced the surface amorphisation because of active oxygen and hydrogen diffusion into deeper layers and formation of hydrogenated silicon carbon with fragments of amorphous carbon films becomes not significant.

Key words: amorphous carbon films, metal impurities, Raman spectroscopy.
PACS numbers: 68.37.−d, 68.90.+g.

Introduction

The insertion of metallic phase into the a-C: H matrix improves its mechanical performance and also gives the rise to new material properties [1]. Carbon films with metal impurities are interesting because of applicable in medicine like toxins of microorganisms [2] or in microelectronics as single electron devices [3]. Early stage of amorphous carbon film with or without metal impurities formation is interestingly because single theory of this process not is in nowadays. The few theoretical models is dominant: complete condensation, growth with re-evaporation, nucleation on defects, and total or null cluster-cluster coalescence [4]. It is known, that particles of metals on the surface catalyzed growth of nanoformation during amorphous carbon films deposition. One of the earliest mechanism for CNT growth proposed A. These and others, and it is the so-called ‘‘scooter mechanism’’ [5], where metal atoms with high electronegativity chemisorbs to the open edge of a curving graphene sheet. It avoids formation of an endohedral fullerene and rearrange of carbon rings. Other mechanisms explaining the CNT growth using metal or non-metal catalyst exist also [6-8], but two of them are most acceptable: tip-growth model and base growth model. Interaction between catalyst particle and surface determined which of them would be dominant. Type of nanoformation (single or multy wall carbon nanotube, fullerene et. all) depends on the catalyst size [9]. Surface temperature is other important factor for nanostructure growth. High temperature is the reason for nanoclustering [10] because graphite like carbon films will forms on the surface during deposition in these conditions. Type of nanoformation (single or multy wall carbon nanotube, fullerene and other) depends on the catalyst size [9]. High temperature is the reason for nano-

clustering [10, 11] because graphite like carbon films will forms on the surface during deposition in these conditions [12]. Formation of graphite like carbon film at comparative low temperatures is possible using PECVD methods, so addition of metals particles can be reason of nanostructrures growth. Influence of metal additions and temperature to the properties of thin amorphous carbon films and possibilities of nanostructures formation are analyzed in this experimental work. The aim of it is to identify of most important physical and chemical processes on the surface during thin amorphous carbon films formation on the silicon surface with metals clusters (Cu) by PECVD method.

Experimental setup

a-C: H films were formed on silicon surface with copper clusters by PECVD method using C_2H_2 gas plasma. The temperature of silicon substrate was 25 °C, 100 °C and, 250 °C. Duration of deposition was 45 s bombarding ion energy was 200 eV. The copper was deposited before carbon film formation during bombardment the copper net by argon ions with ion energy 500 eV, deposition duration 20 min. The deposition and film formation took place in a single two steps technological process The films optical properties were determined by null-ellipsometry (Gaertner L117 with a He–Ne laser (632.8 nm)), Raman spectroscopy (Ivon Jobin spectrometer with a Spectra Physics YAG: Nd laser (532.3 nm, 50 mW, spot size 0.32 mm)). The experimental RS curves were fitted by few Gaussian-shape lines in the spectral range from 500 cm^{-1} to 700 cm^{-1}, from 700 cm^{-1} to 900 cm^{-1}, from 900 cm^{-1} to 1100 cm^{-1} and from 1100 cm^{-1} to 1900 The relative element concentrations were measured by Bruker AXS Microanalysis GmbH.cm^{-1}.

Results

The main properties of films and peaks values of Raman spectra are shown in the table 1 and the table 2. Deposition rate depended on the nature of metal clusters and substrate temperature (0.2 -0.5 nm/s). Differences in the Rama spectra at 25 °C are shown in the figure 1 (Raman shift range is 500 cm^{-1} – 700 cm^{-1}) and figure 2 (range 1100 cm^{-1} – 1800 cm^{-1}). Refractive index of all films is more typical polymer like films with high concentration of hydrogen and sp^2 bonds because extinction coefficients also are very high. It is important that silicon surface after Me clusters deposition is destroyed and activated during ion bombardment, so boundary line between silicon and amorphous carbon film is not clear. Interlayer becomes most important and quantity of various bond of silicon with carbon, hydrogen or oxygen are influencing to the Raman spectra form.

Table 1 – Main properties of a-C:H film with Cu impurities (thickness of film, refraction index, relative concentration of elements in the structure a-C:H/Cu/Si)

Substrate temperature	T=25°C	T=100°C	T=250°C
Thickness d, nm	22	18	12
Refraction index n	1.44	1.6	1,7
Carbon, at.%	14.4	10.3	5.7
Oxygen, at.%	8.3	6.5	5.6
Silicon, at.%	76,6	82,1	87,5
Copper, at.%	0.7	1.1	1.2

The peaks at 517 cm^{-1}, cm^{-1}, 561 cm^{-1}, 617 cm^{-1} and 669 cm^{-1} were obtained in the Raman spectra range from 500 cm^{-1} to 700 cm^{-1} when amorphous carbon films were deposited on the silicon surface with Cu clusters at the room temperature. The peak at 517 cm^{-1} associated with silicon substrate but it shifts to the lower value when surface temperature increased (516 cm^{-1} at 100 °C and 509 cm^{-1} at 250 °C). Shifting of the silicon peak to lower values corresponds with the process of amorphization and intensity of it depends on substrate temperature [13]. Existing peak at 532cm^{-1} -535 cm^{-1} correlate with the strain in the silicon [14] and at the higher temperature it become more intensive. The next two peaks in this range (561 cm^{-1} and 617 cm^{-1}) are related with Cu_2O because this compound have three characteristic vibrations: at 570 cm^{-1}, 618 cm^{-1} and 624 cm^{-1} [15]. Intensities of that are variable and depend on the temperature: the third peak is weak and is not fixed in the spectra when substrate temperature is 25 °C and 250 °C, but becomes dominant at 100 °C. Intensity of the second peak (617 cm^{-1}) decreasing at 100 °C, but it is dominant and shifted to the lower values (614 cm^{-1}) at 250 °C when other two peaks disappear. Variations of these peaks show dependence of structure and concentration of

cooper bonds with oxygen in the film and interlayer on the surface temperature. Wide peak at 669 cm^{-1} is related to the Si-O-Si stretching [16] and its shift to the lower values with the temperature increasing is conditioned by the bond deformation or deficiency of oxygen.

Table 2 a – C:H(Me) film peaks values of Raman spectra

Vibration modes	Peaks n RS spectra of the films, cm^{-1}	References	
Si-Si TO mode	509-518;	520;	[13]
Strain in Silicon	533; 535;	537	[14]
Cu_2O	570; 614; 617; 623;	570; 618; 624;	[15]
SiOH	586-610;	606;	[16]
Symmetric Si-O-Si stretching	664-669;		
Si-CH_3 rocking	690;	687;	[17]
Si-C	682; 732; 784; 763-765; 809-813; 841, 874; 855;		[18] [19] [20]
C-H	1036-1037; 1079;		[21]
Oxyethylene ring deformation	1122;		[22]
D4	1181-1197;	~1190;	[23]
C-O-C stretching	1247;	1252;	[24]
C-C inter-ring stretching	1288;	1286;	[25]
D peak	1313-1396;	1350;	[26]
Transpolyacetylene ν_3 *C=C* stretching mode	1410-1454;	~1450;	[25]
Semicircle stretch vibrations in benzene or benzene clusters	1484;	1486;	[26]
G peak (E_{2g} symmetry)	1510-1553;	1550;	[23]
D‘ (G2 mode)	1611-1637;	1620;	[26, 27]
C=O stretching	1713-1788;	1680-1820;	[28]

The characteristics peaks for hydrogenated amorphous silicon (SiOH) (586 cm^{-1} and 639 cm^{-1}) and Si-C (682 cm^{-1}) becomes more intensive in the spectra when the substrate temperature is 100 °C, but peak of Si-O-Si is less intensive. It means that competition of processes hydrogenation and oxidation of silicon is very important for interlayer formation of the early stage film deposition when substrate temperature increase.

The peak at 732 cm^{-1} associated with O-C-O bonds in plane bending or CH_2 in rocking mode is obtained in the spectra range of 700 cm^{-1} – 900 cm^{-1} for samples with Cu impurities. This range is typical for silicon carbide. Most likely that this peak is related with amorphous SiC because other peaks characteristic for it at 763 cm^{-1},784 cm^{-1}, 809 cm^{-1}, 841 cm^{-1} and 874 cm^{-1} were obtained also. Their intensity decreased with increasing temperature and it show that structure of silicon carbide becomes more orderly because weak peak of crystalline SiC at 855 $cm^{-1}$is defined in the spectra. It is important that peaks related with C-H bonds deformation at 750 cm^{-1} (also peaks at 1037 cm^{-1} and 1079 cm^{-1} in the RS range of 1000 cm^{-1} – 1800 cm^{-1}) becomes more intensive with increasing temperature. And it confirms that the oxygenation becomes less intensive than the hydrogenation of silicon or carbon when temperature of surface increases.

Typical asymmetric curve for amorphous carbon films was not obtained in the Raman spectra range at

1000 cm^{-1} to 1800 cm^{-1}. The separate peaks at 1197 cm^{-1}, 1313 cm^{-1}, 1409 cm^{-1}, 1510 cm^{-1}, 1552 cm^{-1}, 1611 cm^{-1} and 1738 cm^{-1} are identified in the spectra of samples deposited in the 25 °C. First of them together with peak at 1409 cm^{-1} can be related to the vibration of transpolyacetylene carbon groups, but confirmation of it is complicated because other authors [22] demonstrate that intensity of these peaks increase with increasing of hydrogen concentration in the plasma and it is not typical for transpolyacetylene. So, the peak at 1197 cm^{-1} can be attributed to any known sp^2 – related feature also, so in agreeing with the other authors it was remarked that this peak shows highly defective graphitic structure relaxes through the formation of occasional four-coordinated atoms between the planes [29, 30].

So, the shift to the lower values with increasing of the surface temperature is related with increasing of order in the graphitic structure, the relaxing of internal stress and the decreasing of defect. Some authors peak at 1450 cm^{-1} ascribe to fullerene-like structures [31]. Confirmation of it is formation of these structures during longer time (300 s) deposition at the same experimental conditions [32]. It was obtained that this peak shifted to higher values with increasing temperature of samples and becomes equal to 1453 cm^{-1} at 250 °C. Other peaks at 1510 cm^{-1}, 1552 cm^{-1}, 1611 cm^{-1} can be attributed to variation of G band.

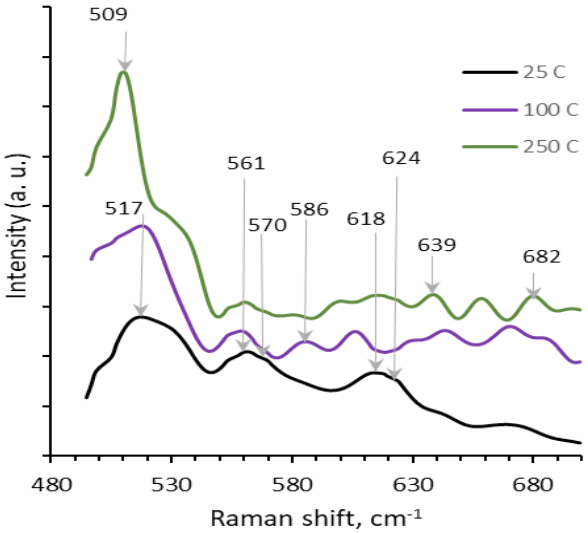

Figure 1 – The Raman spectra of the a-C:H film with Cu impurities in the range from 500 cm^{-1} to 700 cm^{-1}

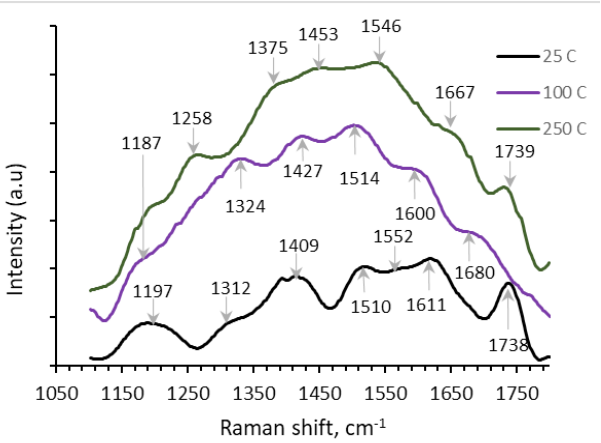

Figure 2 – The Raman spectra of the a-C:H film with Cu impurities in the range from 1100 cm^{-1} to 1800 cm^{-1}

Peak at 1611cm^{-1} is dominated when temperature of surface is 25 °C and it can be related with D` or G2 mode because the tangential G-band (at ~1580 cm^{-1}), which derived from the graphite-like in-plane mode, can split into several modes where two are the most distinct: G1 (1577 cm^{-1}) and G2 (1610 cm^{-1}) [33]. This splitting was also observed in the other papers [33-35].

The peak at 1738 cm^{-1} comes from C=O stretching vibration and is intensive at low temperature. It confirmed that SiCOH groups formed on the surface. This peak becomes weak at 100 °C substrate temperature, but it arises becomes more intensive in the spectra at 250 °C.

Discussion

EDS analysis shows, that initial concentration of Cu is same (1.2%) for all samples but films thickness and growth velocity decreased with increasing of sample temperature. Theoretically, only relative concentrations of carbon and silicon will depend on the film thickness, but cooper concentration will remain same because cooper clusters are in the interlayer and depths of EDS measurement are constant. But experimental results show that cooper concentration also depends on surface temperature and it increased with temperature increasing. So, it is reason for assumption that cooper can be removed from the surface because of desorption or ion bombardment during film deposition at 200 eV ion energy and 25 °C temperature. For that reason concentration of cooper become,

lower (0.8%) and traces of cooper oxides were obtained in the RS spectra. From another side, cooper diffused into the deeper layers using silicon defects when substrate temperature is 100 °C. Concentration of it become lower in the film, but not in the film/interlayer/substrate structure and EDS measurements shows that total Cu concentration is higher (1.16%) but intensity of cooper oxides peaks becomes lower in the Raman spectra. Peaks of Cu_2O disappears, but relative concentration of Cu remain similar (1.18%) when temperature increases till 250 °C and it show that diffusion process becomes more intensive at higher temperature. Amorphisation of silicon confirms these assumptions (shift of the silicon peaks into the lower values at higher temperatures, table 2). Single peak at 614 cm^{-1} remains in the RS spectrum at highest temperature case, but it not related with cooper oxide because other additional peaks not exist there. Also single similar peaks at 613 cm^{-1} – 617 cm^{-1} were obtained in the samples with Ag and Au [32], so it was decided that this peak is attributed to the C–C–C deformation in-plane vibration [36].

Analysis of the RS spectra in the other ranges shows that hydrogen remains in the forming film while Cu atoms bonds with oxygen and only part of it penetrate into the silicon substrate at low temperature. Slow film formation and more intensive penetration of hydrogen and oxygen into the silicon at higher temperatures create condition for hydrogenated silicon carbide formation. More intensive peaks related with Si-H, Si-C and Si-O and obtained in the spectra confirm this assumption. It is important also, that typical for the amorphous hydrogenated carbon films D and G modes in the spectra have low intensities and it shows that a-C:H films is in early stage formation at low temperature. C-C bond become more ordered when temperature increased and it conditioned that thickness of this ordered film decreased. Measurement of refracting indexes also confirms these assumptions. Low refractive index (1.4) of films deposited at 25 °C is more characteristic for SiCOH films formed by PECVD method [37] than amorphous carbon film. Refractive index increased with temperature increases and becomes ~1.6 at 250 °C. Featureless visible Raman spectra with no clear Raman peaks shows that films becomes polymer like (PLC) with low Young modulus (≤20 GPa) and low density (≤1,2 g/cm^3) [38].

Conclusions

Formation of hydrogenated silicon carbon with fragments of amorphous carbon films on the silicon surface was obtained during early stage of a: C-H films deposition by PECVD methods. Carbon films with more ordered C-C bond grows during film formation at higher temperatures (>100° C) on the silicon surface with Cu particles, because atoms of cooper penetrate into the deeper layers of silicon. Amorphisation of substrate increases also. Lower refractive index than typical amorphous carbon films confirmed that the films deposited at 25 °C is more characteristic for SiCOH films. The typical for the amorphous hydrogenated carbon films D and G modes in the spectra have low intensities when films were formed at low temperature. More polymer like films forms at higher temperatures of the substrate.

References

1. Kukielka S., Gulbiński W., Pauleau Y., Dub S.N. and Grob J.J. (2007). Nikel/Hydrogenated amorphous carbon composite films deposited in acetylene/argon microwave plasma discharge. Reviews on advanced materials science, 15, 127 – 133.

2. Ivanov-Omskii V.I., Panina L.K., Yastrebov S.G. (2000). Amorphous hydrogenated carbon doped with cooper as antifungal protective coating. Carbon, 38, 495-499

3. Kolobov A.V., Oyanagi H., Akinaga H., Zvonaryova T.K. and Ivanov-Omskii V.I. (2000). Cooper and cobalt nanoclusters embedded in hydrogenated amorphous carbon: an X-ray absorption study. 8th Int. Symp. „Nanostructures: Physics and Technology“, St.Peterburg, Russia, 299-303

4. Jensen P. (1999). Growth of nanostructures by cluster deposition: Experiments and simple models. Reviews of Modern *Physics*, 71, 1695–1735

5. Thess A., Lee R., Nikolaev P., Dai H., Petit P., Robert J., Young H. Lee, Xu C., Kim S. G., Rinzler A. G., Colbert D.T., Scuseria G.E., Tomanek D., Fischer J.E., Smalley R.E.(1996) Crystalline Ropes of Metallic Carbon Nanotubes. Science, 273(5274), 483-487.

6. Hong G., Chen Y., Li P., Zhang J. (2012). Controlling the growth of single-walled carbon nanotubes on surfaces using metal and non-metal catalysts. Carbon, 50 (6), 2067-2082.

7. Ding F., Rosen A. and Bolton K. (2005). Dependence of SWNT growth mechanism on temperature and catalyst particle size: Bulk versus surface diffusion. Carbon, 43 (10), 2215-2217.

8. Tessonnier J.P, Su D.S. (2011). Recent progress on the growth mechanism of carbon nanotubes: a review. ChemSusChem, 4(7), 824-847.

9. Yellampalli Siva. (2011). Carbon Nanotubes – Synthesis, Characterization, Applications, SRM University, India

10. Mora E., Pigos J.M., Ding F., Yakobson B.I. and Harutyunyan A.R. (2008). Low-temperature single-wall carbon nanotubes synthesis: feedstock decomposition limited growth. Journal of the American Chemical *Society*, 130, 1-8.

11. Tailleur A., Achour A., Djouadi M.A., Le Brizoual L., Gautron E., Tristant P. (2012). PECVD low temperature synthesis of carbon nanotubes coated with aluminum nitride. Surface & Coatings Technology, 211, 18–23.

12. Fadzilah A.N., Dayana K., Ruso M. (2013). Fabrication and characterization of camphor-based amorphous carbon thin films. Procedia Engineering**,** 56**,** 743 – 749.

13. Ambrosone G., Basa D.K., Coscia U., Santamaria L., Pinto N., Ficcadenti M., Morresi L., Craglia L., Murri R. (2010). E-MRS Spring meeting 2009, Symposium B. Structural and electrical properties of nanostructured silicon/carbon films. Energy Procedia, 2, 3-7

14. Prakash R., Amirthapandian S., Phase D.M., Deshpande S.K., Kesavamoorthy R., Nair K.G.M. (2006). Study of ion beam induced mixing in nano-layered Si/C multilayer structures. Nuclear Instruments and Methods in Physics Research Section B Beam Interactions with Materials and Atoms, 37 (30), 283-288.

15. Gan Z.H., Yu G.Q., Tay B.K., Tan C.M., Zhao Z.W., Fu, Y.Q. (2004). Preparation and characterization of copper oxide thin films deposited by filtered cathodic vacuum arc. Journal of Physics D: Applied Physics, 37(1), 81-85.

16. Grigonis A., Rutkuniene Z. and Vinciunaite V. (2010). Different wavelength laser irradiation of amorphous carbon. Acta Physica Polonica A, 120 (1), Proceedings of the VIII International Conference ION 2010, Kazimierz Dolny, Poland, 26-29/

17. Bae S.C., Lee H., Lin Z., Granick S.(2005). Chemical imaging in a surface forces apparatus: confocal Raman spectroscopy of confined poly(dimethylsiloxane). Langmuir, 21(13), 5685-5688.

18. Wasyluk J., Perova T.S., Kukushkin S.A., Osipov A.V., Feoktistov N.A., Grudinkin S.A. (2010). Raman investigation of different polytypes in SiC thin films grown by solid-gas phase epitaxy on Si (111) and 6H-SiC substrates. Materials Science Forum, 645-648, 359-362.

19. Moumita Mukherjee (2011). Silicon Carbide – Materials, Processing and Applications in Electronic Devices, Rijeka, Croatia, 8-9.

20. Kuntumalla M.K., Ojha H., Srikanth V.S. (2013). Identification of β-SiC surrounded by relatable surrounding diamond medium using weak Raman surface phonons. Bulletin of Materials Science, Volume 36 (6), 1087-1090.

21. Casiraghi C., Piazza F., Ferrari A.C., Grambole D., Robertson J. (2005). Bonding in hydrogenated diamond-like carbon by Raman spectroscopy. Diamond and Related Materials*,* 14, 1098-1102.

22. Birrell J., Gerbi J. E., Auciello O., Gibson J.M., Johnson J. and Carlisle J.A. (2005). Interpretation of the Raman spectra of ultrananocrystalline diamond. Diamond and Related Materials, 14 (1), 86-92.

23. Schwan J., Ulrich S., Batori V., Ehrhardt H., Silva S.R.P. (1996). Raman spectroscopy on amorphous carbon films. Journal of Applied Physics, 80 (1), 440-447.

24. Ahmed M.H., J.A. Byrne. (2012). Effect of surface structure and wettability of DLC and N-DLC thin films on adsorption of glycine. Applied Surface Science, 258 (12), 5166–5174.

25. Ferrari A.C., Robertson J. (2001). Origin of the 1150 cm^{-1} Raman mode in nanocrystalline diamond. Physical Review B, 63, 121405-12408.

26. Makarova T., Ricc M., Pontiroli D., Mazzani M., Belli M., and Goffredi A. (2008). Ageing effects in nanographite monitored by Raman spectroscopy. Physica status solidi (b), 245(10), 2082–2085.

27. Pimenta M.A., Dresselhaus G., Dresselhaus M.S., Cancado L.G., Jorio A., Saito R. (2007). Studying disorder in graphite-based systems by Raman spectroscopy. Physical Chemistry Chemical Physics, 9, 1276–1291

28. Cong C., Yu T., Saito R., Dresselhaus G.F., Dresselhaus M.S. (2011). Second-Order Overtone and Combination Raman Modes of Graphene Layers in the Range of 1690-2150 cm^{-1}. ACS Nano, 5 (3), 1600 –1605.

29. Ulrich J., Batori S., Ehrhardt V., and Silva. (1996). *Raman spectroscopy on amorphous carbon films***.** Journal of Applies Physics, 80 (1), 440 – 447.

30. Beeman D., Silverman J., Lynds R. and Anderson M. (1984). Modeling studies of amorphous carbon. Physical Review *B,* 30 (2), 870-875.

31. Blank V.D., Denisov V.N., Kirichenko A.N., Kulnitskiy B.A., Martushov S.Yu., Mavrin B.N. and Perezhogin I. A. (2007). High pressure transformation of single-crystal graphite to form molecular crbon onions. Nanotechnology, 18, 345601-1-4.

32. Rutkuniene Z., Vigricaite L. and Grigonis A. (2014). Nanostructure Formation during Amorphous Carbon Films Deposition. *ACTA PHYSICA POLONICA A* Vol. 125, No. 6, 1303-1306

33. Zdrojek M., Gebicki W., Jastrzebski C., Melin T., Huczko A. (2004). Studies of Multiwall Carbon Nanotubes Using Raman Spectroscopy and Atomic Force Microscopy. Solid State Phenomena*,* 99-100, 265-268.

34. Rao A.M., Ritcher E., Bandow S., Chase B., Eklund P.C., Williams K.A., Fang S., Subbaswamy K.R., Menon M., Thess A., Smalley R.E., Dresselhaus G., Dresselhaus M.S. (1997). Diameter-Selective Raman Scattering from Vibrational Modes in Carbon Nanotubes. Science, 275 (5297),187-191.

35. Duesberg G.S., Loa I., Burghard M., Syassen K., and Roth S. (2000). Polarized Raman spectroscopy on isolated single-wall carbon nanotubes**.** Physical Review Letters*,* 85 (25), 5436-5439.

36. Nguyen B., Thu Vu T.K., Nguyen Q.D., Nguyen T.D., Nguyen T.A., Trinh T.H. (2012). Preparation of metal nanoparticles for surface enhanced Raman scattering by laser ablation method. Advances in Natural Sciences: Nanoscience and Nanotechnology, 3(2)**,** 025016.

37. Park J.-M., Rhee Sh.-W. (2002). Remote plasma-enhanced chemical vapour deposition of nanoporous low-dielectric constant SiCOH films using vinyltrimethylsilane. Journal of the Electrochemical Society, 149(8), F161–F170.

38. Casiraghi C., Piazza F., Ferrari A.C., Grambole D., Robertson J. (2005). Bonding in hydrogenated diamond-like carbon by Raman spectroscopy. Diamond and Related Materials, 14, 1098-1102.

IRSTI 29.19.21 https://doi.org/10.26577/phst-2019-2-p10

Polymorphic phase transitions and recombination luminescence in ammonium halide crystals

T.A. Koketayev and A.K. Tussupbekova*

Karaganda State University named after Y.A. Buketov,
100028, 28, Universitetskaya str., Karagandy, Kazakhstan
**e-mail adress: tussupbekova.ak@gmail.com*

Spectral-luminescent properties of ammonium halide crystals were studied in this work. The properties of the peak of thermally stimulated luminescence (TSL) in the region of the phase transition temperature were studied and the basic laws were established. A sequential thermal annealing isolated the TSL peak with a maximum at 240 K for ammonium chloride activated with rare-earth ions (RI). It was found that an order-disorder phase transition occurs for activated RI of ammonium chloride at a temperature of 240 K. An appearance of TSL peak with a maximum at 240 K causes because of exposure to ionizing radiation upon activation of ammonium halides by thallium and tin ions. This phenomenon is observed when ammonium halides are activated by europium, ytterbium, neodymium, praseodymium, copper, cadmium and potassium ions. The introduction of impurity homologous anions into the crystal lattice does not give a similar effect. Therefore, it can be argued that observed phenomenon is associated with the presence of impurities in the cationic sublattice and its appearance does not depend on the parameters of the impurity center. On the one hand, the TSL peak is not impurity, since its position is determined by the properties of matrix and on the other hand, its appearance is associated only with substitution ions in the cationic sublattice. The obtained results allow studying the crystals response under exposition to ionizing radiation.

Key words: luminescence, radiation-stimulated processes, crystal, defects.
PACS numbers: 61.10.Ht, 61.50.Ks, 61.72.−y, 61.80.−x.

1 Introduction

Investigations of the spectral-luminescent properties of ammonium halide crystals activated by various metallic ions have established that phase transitions cause abrupt changes in the parameters of the luminescence centers. The most significant changes are observed in the frequency of active vibrations of impurity ions, electron-phonon interaction, mean free path and activation energy of exciton migration.

In crystals with complex anions and cations, radiation-stimulated processes have a number of specific features. Radiation defects can conditionally be divided into primary and secondary defects. Primary defects arise as a result of exposure to ionizing radiation, secondary defects appear during the transformation of primary defects as a result of migration of radiolysis products. Recombination luminescence is also a consequence of the migration of radiolysis products. It is obvious that the thermal activation of migration and the migration of radiation defects themselves are structurally sensitive. Therefore, polymorphic phase transitions should have a significant effect on the course of radiation-stimulated processes. In this paper, we consider a number of phenomena in irradiated crystals due to rearrangement of the crystal lattice [1-15].

2 Experiment

Ammonium halide crystals in the temperature range of 80-300 K have an order-disorder polymorphic phase transition. Figure 1 shows, by way of example, the curves of thermally stimulated luminescence for pure (1) and activated with Tl^+ (2) and Sn^{2+} (3) ions for a crystal of ammonium chloride. In an unactivated crystal, there are two peaks of thermally stimulated luminescence in the region of 110–120 K

and 160–180 K. The first peak of the recombination luminescence is associated with the thermal activation of the migration of Vc centers. From an analysis of the results of our studies of thermostimulated currents and thermal bleaching of radiation-induced absorption bands and published data, it was established that the second TSL peak is due to the decay of defects of the NH_3^+ type.

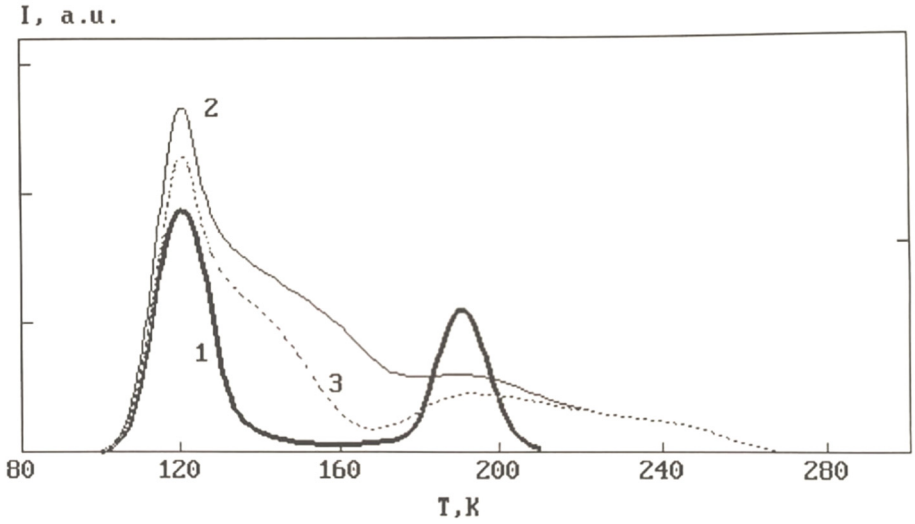

Figure 1 – TSL curves of pure (1) and doped with thallium (2) and tin (3) ions NH_4Cl

When NH_4Cl crystals are activated by Tl^+ or Sn^+ ions, in addition to the TSL activator peaks, a glow appears in the region of 200–250 K in the form of a "shoulder" of a high-temperature peak. Similar TSL curves with the same activators are also observed in NH_4Br crystals (Figure 2).

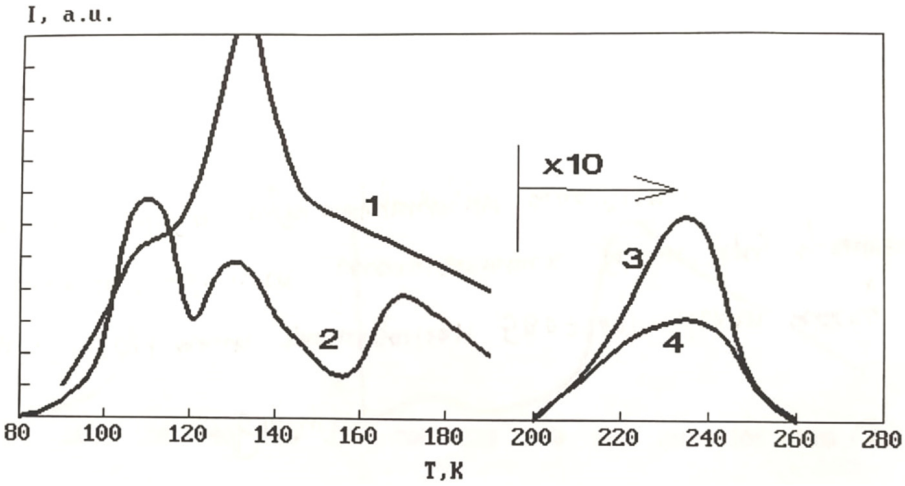

Figure 2 – TSL curves of NH_4Br crystals activated by thallium (1) and tin ions (2) and after thermal annealing at 190-200 K, respectively (3) and (4)

For activated RI of ammonium chloride, a TSL peak with a maximum at 240 K was isolated by sequential thermal annealing (Figure 2). It is known that an order-disorder phase transition occurs at this temperature. Therefore, as a result of the activation of ammonium halides by thallium and tin ions after exposure to ionizing radiation, a TSL peak appears, the maximum of which is linked to the phase transition temperature.

It was established in the work that a similar phenomenon is observed upon activation of ammonium halides by europium, ytterbium, neodymium, praseodymium, copper, cadmium and potassium ions. Thus, regardless of the nature of the impurity ions, a TSL peak appears in the region of the phase transition temperature. The introduction of impurity homologous anions into the crystal lattice does not give a similar effect. Therefore, it can be argued that this phenomenon is associated with the presence of impurities in the cationic sublattice. The appearance of this phenomenon does not depend on the parameters of the impurity center. On the one hand, the TSL peak under study is not impurity, since its position is determined by the properties of the matrix; on the other hand, its appearance is associated only with substitution ions in the cationic sublattice. Studying the properties of the TSL peak in the region of the phase transition temperature, the following basic laws were established:

1. The high-temperature "shoulder" in the region preceding the temperature of the order – disorder structural phase transition arises only in activated and irradiated crystals. Checking the occurrence of this phenomenon due to pre-radiation defects did not give positive results;

2. The appearance of recombination luminescence in the phase transition region is independent of the electronic and charge state of the impurity. The impurity ion must be a substitutional ion in the cationic sublattice.

3. Within the accuracy of the TSL method, the activation energy of the peak extracted by thermal annealing does not depend on the nature of the cationic impurity ion.

4. The spectral composition of the radiation of the high-temperature peak of the matrix and in the phase transition region are qualitatively the same. It consists of a band of activator luminescence and radiation with a maximum of 2.5 eV. In the NH_4Cl-K^+ crystal, there is radiation in the region of 3.8 eV. However, it cannot be attributed to an activator, because it is optically inactive. It was shown that the 3.8 eV band can be attributed to a near-activator exciton.

5. The dependences of the accumulated light sum in the studied peak on the exposure dose and concentration reveal the relationship of this phenomenon with impurity ions.

Earlier, we proposed a recombination luminescence model related to structural features and dynamics of NH_3^+ defects [12, 16]. Its reorientation in the 180K region leads to perturbation of the nearest cation and the proton from it can pass into the anionic sublattice, which leads to the launch of recombination mechanisms. Assuming that in activated crystals, cationic impurity ions "freeze" the reorientation of NH_3^+ defects, the recombination mechanism is triggered by the reorientation of the ammonium ions NH_3^+ themselves. This allows us to explain all the established patterns. Upon recombination of the NH_3^+ ion with hydrogen, a mobile hole appears in the anion sublattice. Its migration and interaction with electronic centers leads to the transfer of energy to impurity ions. An activator glow appears. In this temperature range, the luminescence of the excitons themselves is quenched, etc.

It was experimentally established that pure ammonium halides have a "memory" of previous exposure. In figure 3 shows the corresponding result. Curve 1 – TSL of inactive NH_4Br. Curve 2 – TSL of NH_4Br, measured after the first exposure, heating to 300K, cooling to 80K, and re-exposure. It is seen that in this case a "shoulder" appears, which is characteristic of an activated crystal.

It was found that AGA have another TSL peak in the region of 360-380K, depending on the anion. Its study is difficult, since ammonium halides are sublimated when heated. In view of the foregoing, it can be argued that in AGA this high-temperature TSL peak is associated with a defect in the cationic sublattice. One of all known defects is the hydrazine ion $N_2H_4^+$. The crystals "remember" about the previous exposure when stored at room temperature for about 20 hours, which is consistent with the literature on EPR on the stability of hydrazine ions. Thermal annealing of the TSL peak above 300K leads to the disappearance of the "memory" effect. Thus, the features of recombination luminescence in the region of the phase transition temperature made it possible to establish a defect, the decay of which is responsible for the high-temperature peak of TSL.

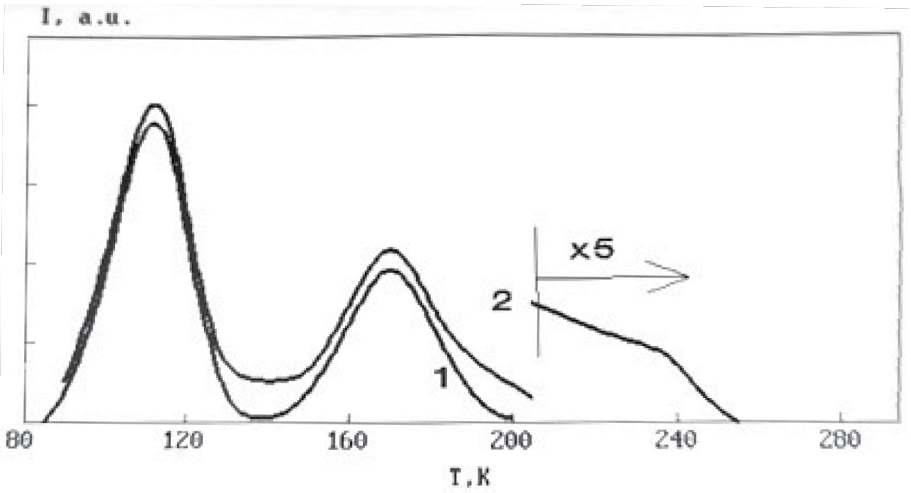

Figure 3 – TSL curves of NH_4Br pure (1) and after repeated irradiation (2)

$LiKSO_4$ crystals have in the region of 80-300K two polymorphic phase transitions at 180K and 250K in the heating mode. Low-temperature – the first kind and comes with the release of heat, the second – the second kind [13, 17-19].

After irradiation with x-ray quanta at liquid nitrogen temperature, the spectra of thermally stimulated luminescence were measured. In figure 4 shows the TSL curve for the $LiKSO_4$ crystal. A rather complicated picture was obtained, having luminescence maxima at 125K, 150K, 205K, 260K. In addition, an increase in luminescence is observed in the 170K-180K region, accompanied by stochastic outbursts of luminescence intensity. The last peak of the luminescence is complex, since there is a "shoulder" on the high-temperature wing, which indicates the presence of another TSL peak with a lower light sum and strongly overlapping with luminescence at 260K.

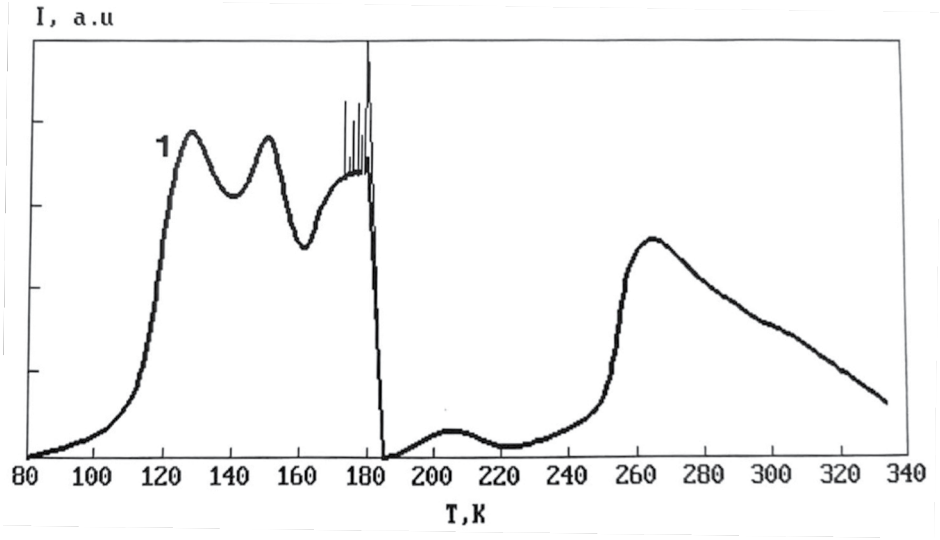

Figure 4 – TSL crystal curve of $LiKSO_4$.

In figure 5 shows the TSL curve of mixed lithium potassium sulfate after irradiation at 80 K, slow heating to a temperature not higher than 175 K, followed by cooling. It is seen that the thermal annealing of the low-temperature TSL peaks leads to the disappearance of a weak glow in the 205K

region. Using the method of subsequent thermal annealing, it was shown that the same recombination process is responsible for the luminescence in the regions of 170-180K and 205K. The appearance of a recombination luminescence peak at 205K depends on the heating rate. With a slow rise in temperature, it disappears. It is natural to associate the separation of one peak into two with an abnormal decrease in the glow intensity of the low-temperature component with a polymorphic phase transition at 180 K. It is a first-order transition. The observed anomalies indicate that when the structure of the crystal lattice changes, the activation energy of recombination luminescence increases.

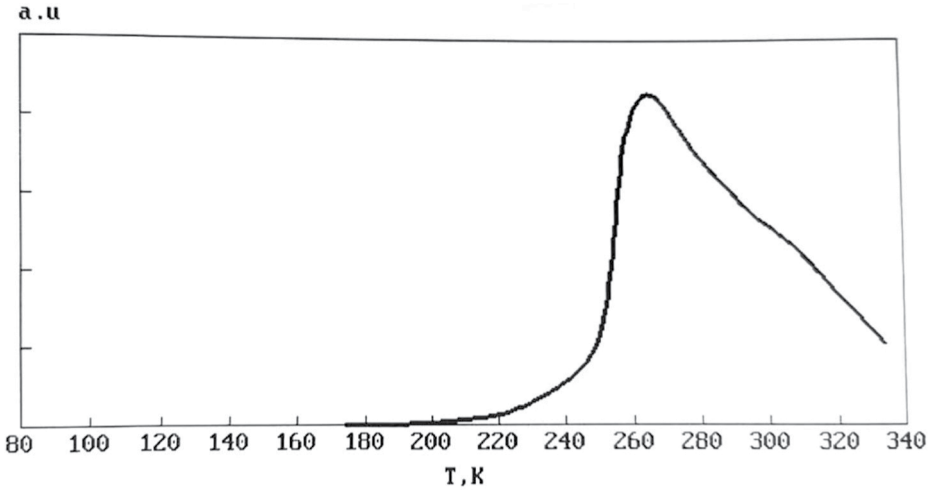

Figure 5 – TSL curve of $LiKSO_4$ crystal after thermal annealing at 175 K

Stochastic emissions in the region of 170-180K (see Figure 4) are repeated from experiment to experiment. Their number, intensity, and temperature position of an individual ejection are changing. The temperature range of their observation, the position of the last ejection remain unchanged. Note that in an unirradiated crystal this phenomenon does not exist. The phase transition at 180 K is of the first kind and is accompanied by the release of heat. The assumption that this transition is preceded by the formation of "nuclei" of a new phase allows one to explain these recombination "thermoscintillations". The heat released during the formation of "nuclei" leads to additional activation of recombination processes in the low-temperature phase.

An increase in the activation energy during the 180K phase transition and the presence of the corresponding TSL peak creates a situation when it is possible to expect the appearance of a "cold" flash. Figure 6 shows this result.

After heating the crystal to the indicated temperature, recombination luminescence occurs again upon cooling. A small peak sum at 205K does not allow for numerous thermal cycling.

For TSL peaks in the 260K region (Figure 4), the observed recombination luminescence has an anomalously fast luminescence flare up in the 250K region. there is also a phase transition, but of the 2nd kind. The shape of the TSL curve suggests that in this case the activation energy decreases.

The spectral composition of the TSL peak at 260 K has the form of a single weakly asymmetric band on the long-wave side with a maximum in the region of 2.8 eV. Our measurements of the TSL curves at various doses of radiation and spectral composition on the wings of the TSL peak showed that the shape of the curve does not change qualitatively, and the radiation spectrum is the same. This suggests that this complex TSL peak is due to the decay of the same defects slightly differing in thermal stability. The crystal lattice structure of this sulfate allows the existence of one type of defects having different coordination and, therefore, thermal stability.

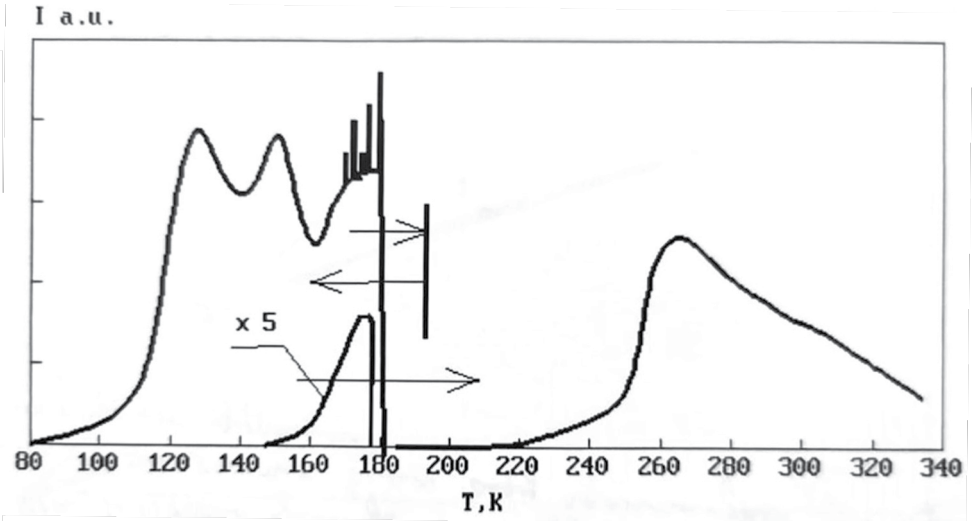

Figure 6 – "Cold flash" in $LiKSO_4$ in the area of 170K. the arrows indicate the temperature course, the figure indicates the increase in gain

The TSL peak at 260K does not change shape with increasing radiation dose. This allows measurements to be taken on the accumulation of the light sum depending on the irradiation temperature without separation. In figure 7 shows the dependence of the light sum in high-temperature TSL peaks on the irradiation temperature. It can be seen that above 180 K the nature of the dependence changes dramatically. A slight decrease in the light sum with increasing temperature is associated with a partial annealing of defects during irradiation.

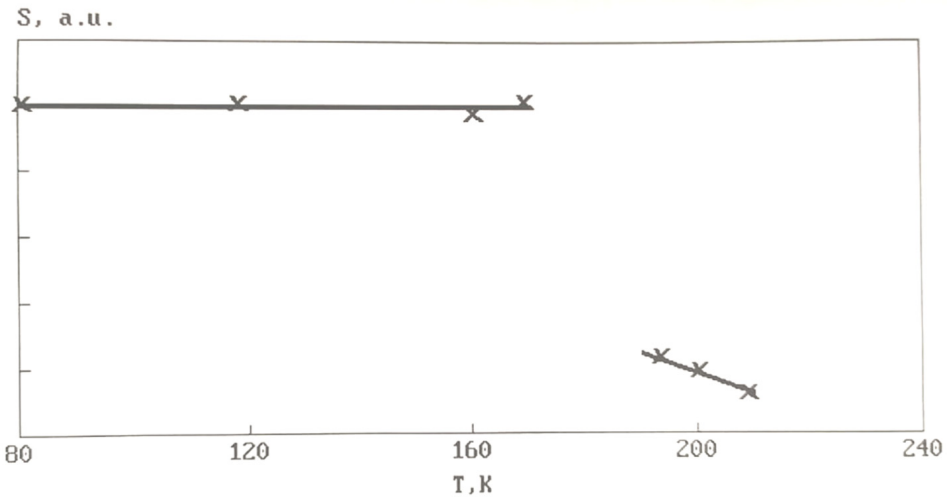

Figure 7 – Dependence of the light sum of the high-temperature TSL peaks in $LiKSO_4$ on the irradiation temperature

Figure 8 shows the dependences of the light sum of the studied luminescence peaks on the exposure dose. After irradiation at nitrogen temperature, the accumulation curve of the light sum is well approximated by two linear dependences: with an exposure dose of up to 30 minutes and from 30 to 90 minutes (see Figure 8).

The presence of two stages of accumulation is possibly associated with the presence of

different mechanisms of defect formation. Curve 2 shows the same dependence, but upon irradiation at a temperature of 220K, i.e. higher than the temperature of the first phase transition. A comparison of these curves suggests that one of the defect formation channels is structurally sensitive, while the second is not. Note that if the temperature of 220K is achieved by cooling, then the light sum does not accumulate in the temperature range of 250-300K. The second phase transition has significant hysteresis. In cooling mode, it occurs at 200K. The absence of TSL peaks is due to the fact that during the irradiation process, thermal annealing of defects occurs [20 – 22].

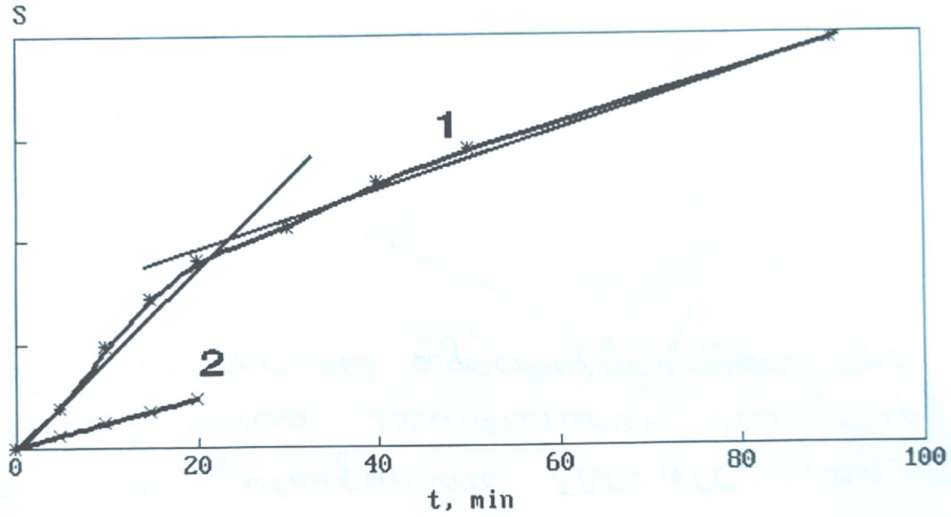

Figure 8 – Dependence of the accumulated light sum at TSL peaks in the region of 260 K on the exposure dose at 80K (1) and 220K (2) in $LiKSO_4$

In sulfates of all known radiation defects (SO_4^-, SO_3^-, O^- and SO_3^{2-}), only SO_3^- according to published data is formed as a result of SO_4^- conversion [23-26].

3 Conclusions

We have determined by quantum chemical methods that this requires the interaction of SO_4^- with atomic oxygen. Obviously, due to the need for a similar transformation of oxygen migration defects, the process is structurally sensitive. Another channel for the formation of SO_3^- defects is the ionization of SO_3^{2-} centers. When ammonium halide crystals are irradiated with X-rays, ionization practically does not feel changes in the lattice structure. In addition, the resulting free electron experiences dissociative capture by the sulfate anion, which leads to the formation of O^- and SO_3^{2-}. Consequently, ionization does not lead to a decrease in the concentration of the latter, which ensures the observed linear dependence on the radiation dose.

The above results show that the use of a polymorphic phase transition allows one to obtain additional information about radiation-stimulated processes, i.e. it can be used as a tool to study the response of crystals to ionizing radiation.

References

1. Dikke G.H., Crosswhite H.M., Dunn B. (1961). Emission Spectra of the Doubly and Triply Ionsed rare carths. J. Opt. Spec. America, 51, 820-827.

2. Aseltine C. L., Kim Y.W. (1967). Electron Paramagnetic Resonance Studies of Electron Irradiated Lithium Sulphate at Liquid Nitrogen Temperature. J. Phys. Chem. Sol., 28, 867-873.

3. Hariharan N., Sobhanandri J. (1969). ESR studies of paramagnetic centers in irradiated Li_2SO_4:H_2O. J. Phys. Chem. Sol., 30, 778-781.

4. Kumar V.S.K., Sastry S.B.S., Acharyulu B.S. (1989). Optical stadies on Europium Doped K_2SO_4. Phys.Stat.Sol. (b), 155, 679-684.

5. Hisnnyakov V., Zazubawich S., Soovik T. (1974). Kinetik and temperatures dependens of polarised emmission of anisotropic centers in alkali halides. Phys. stat. sol., 66, 727-731.

6. Natarajan M., Secco E. (1975). Electrical Condactivity and Phase Transformation Studies on Pure and Doped (Mg^{+}, Zn^{2+}, Cu^{2+}, Mn^{2+}) Crystal of K_2SO_4. Can. J. Chem., 53, 1542-1547.

7. Jia Wie-yi, Wang H., Shen J., Huang Y., Gu B.(1984). Optical rotation and phase transitions of $LiKSO_4$ crystal. Acta phys.sin., 33, 1765-1770.

8. Wang J., Wang R., Zhang L., Li F., Lin S. (1989). The atteanuation peak and elastic anomaly of $LiKSO_4$ crystal under low temperature. J. Low Temp. Phys., 11, 135-140.

9. Perpetuo G.I., Dantas M.S., Gazzinelli R., Pimenta M.A. (1991). Low-temperature suguence of phase trasitionin $LiKSO_4$ studied by EPR. Phys. Rev. B, 45, 5163-5770.

10. Sheludko V.I., Nedilko S.G., Bojko V.V. (2003). Post-annealing green luminescence of sulphate crystals. Functional Matter., 10, 93-97.

11. Lochab S.P., Share P.D., Chauhan R.S., Salah N., Pandey A. (2006). Thermoluminescence and photoluminescence study of $Ba_{0,97}Ca_{0,03}SO_4$:Eu. J. Phys. D., 39, 1786-1792.

12. Su Fuhai, Ma Balei (2006). Luminescence temperature and pressure studies of Zn_2SiO_4 doped by with Mn^{3+} and Eu^{3+} ions. J. Luminescence, 116, 117-126.

13. Aitasalo T., Durigyn A., Holsa J., Lastusaari J., Suchocki A. (2004). Low temperature thermoluminescence properties of Eu^{2+} and R^{3+} doped $CaAl_2O_4$. Allows and compounds, 380, 4-8.

14. Lakshminarasimhan N., Varadarajui U.V.J. (2004). Eu^{3+} luminescence – a structural probe in $BiCa_4(PO_4)_3O$ an apatite related phosphate.Solid State Chem., 177, 3536-3544.

15. Shim J.B., Yoshikawa A., Bensalah A., Fucuda T. Solovieva N., Niki M., Rosetta E., Vedda A., Toon D.H. (2003). Luminescence, radiation damage and color center creation in Eu^{3+}-doped $Bi_4Ge_3O_{12}$ fiber single crystals. J. Appl. Phys., 93, 5131-5135.

16. Alybakov A.A., Gubanova V.A., Kudabaev K., Sharsheev K.(1988). Optical absortion and EPR spectra of Cu^{2+} ions in $LiKSO_4$ single crystals. Phys.Status.Solidi (b), 146, 135-139.

17. Kim L.M., Kuketayev T.A. (2000). Polymorphic phase transitions and recombination luminescence in crystals. Vestn. KazGU. Ser. Physical, 2 (9), 3-12.

18. Kuketayev T.A. (2003). Influence of phase transition in crystals on radiation-induced processes. 12th international conference on radiation physics and chemistry of inorganic materials. 45–46.

19. Kuketayev T.A. (2003).The effect of heterovalent impurity ions on the recombination of radiation defects in sulfates. 4th international conference “Nuclear and radiation physics”, 248-249.

20. Kuketayev T.A. (2004). Radiation defect formation in lithium sulfate crystals. News of universities. Physics, 3, 87-88.

21. Salkeyeva A.K, Kim L,M., Kuketayev T.A. (2005). Recombination luminescence of potassium sulfate activated by samarium ions. Poisk, 4, 34-40.

22. Kuketayev T.A. (1988). Radiation defects and phase transitions in crystals. Bulletin of the Academy of Sciences of the Kazakh SSR. Ser. Phys.-Math., 35-38.

23. Kuketayev T.A. (1989). Features of the decay of excitons into structural defects in crystals of ammonium halides. Solid State Physics. 6, 256–258.

24. Krupin A.S., Karyakin M.E., Molostova E.Yu. (2015). Optical properties of LC complexes of samarium (III) and europium (III). Bulletin of the Technological University, 14, 36-39.

25. Koketai T.A., Mussenova E.K. (2018). Luminescence of K2SO4 Crystals Doped by Ions of Divalent Rare-earth Elements. Book of abstracts. Functional Materials and Nanotechnologies, 164.

26. Lushchik A.Ch., Kuketay T.A., Tussupbekova A.K., Tagaeva B.S. (2015). Luminescence of potassium sulfate crystals with an admixture of ions of divalent rare earth elements. International Scientific and Practical Conference dedicated to the 90th anniversary of Academician Y.A. Buketov, 308-311.

Toktar Iskatayevich Taurbayev (14.11.1937 – 05.06.2019)

Dedicated to the memory of scientist and developer of photovoltaics in Kazakhstan, obituary

Toktar Iskatayevich Taurbayev, physicist, candidate of physical and mathematical sciences, professor at al-Farabi Kazakh National University and chief researcher of the Institute of Experimental and Theoretical Physics (IETP) and Natoinal Nanotechnological Laboratory of Open Type (NNLOT). He was a remarkable man and a great developer of the scientific direction of "Photovoltaics" in the Republic of Kazakhstan. He has passed away on the 05 th June, 2019 at the age of 81.

Toktar Taurbayev was born on November 14, 1937 in Almaty, Kazakhstan. In 1962, he graduated from the Tomsk Polytechnical University, with qualification in semiconductor and dielectric materials. In between 1966-1970, he was an aspirant of the Physics and Energetics Institute of the USSR Academy of Sciences, in Obninsk, Russian SSR. In 1971, he defended his candidate thesis on the topic: "The study of EMF in semiconductors with fissile material".

Since 1973, T. Taurbayev worked at the Faculty of Physics at al-Farabi Kazakh National University. He started his university career as a senior scientific fellow at the Department of nuclear physics. Since 1977, he started giving lectures as an Assistant professor at the Department of solid-state physics. At the same period T. Taurbayev is being involved in active research work and was a coordinator of scientific research projects with various organizations, such as NPO Kvant, Moscow, GOI, Institute of High Energies and INP. In 1978, the T.I. Taurbaev's research group on of the first in the Soviet Union, obtained solar cells with efficiency compared with the level of the best samples in the world. Later these solar cells were used in solar panels, which were installed on the wings of Soviet satellites.

In 1982, T.I. Taurbayev founded the "Laboratory of semiconductor optoelectronics and photonics" equipped with latest educational research equipment, computers and office equipment which employs was more than 50 people. In addition to the continuation of applied research, an important focus of his laboratory was the performance of fundamental researches related to the study of different semiconductor materials and their optoelectronic properties.

During the work the laboratory staff have published about 100 articles, 200 abstracts and proceedings of conferences and obtained 40 authorship certificates. More than a hundred students completed their diploma projects in the laboratory on semiconductor materials, as well as solar cells based on gallium arsenide, amorphous and crystalline silicon.

Under supervising of Toktar Taurbayer 9 candidates in physical and mathematical sciences and 3 Ph.D have successfully defended their thesis.

Two Marks of Honor have awarded T.I. Taurbayev: for contribution to the development of science in the Republic of Kazakhstan and «Honorary Worker of Education» of the Republic of Kazakhstan.

Professor T.Taurbayev continued research works in the development of semiconductors and dielectric materials physics and their application in photovoltaics as a head of scientific projects in a number of fundamental research programs of the Ministry of Education and Sciences of the Republic of Kazakhstan. At the same time, Laboratory of semiconductor optoelectronics and photonics carried out researches and production activities, introducing novel semiconductor technologies at enterprises in Kazakhstan. He was also engaged in activity related with establishment of close scientific, industrial and pedagogical relationships with leading universities in the former Soviet space and far abroad. Among them Lomonosov Moscow State University (MSU, Moscow, Russia), Moscow Physical and Technical Institute (Moscow, Russia), Institute of Radioelectronics RAS (Fryazino, Russia), Saint-Petersburg State University (Saint-Petersburg, Russia), Ioffe Physical and Technical Institute (Saint-Petersburg, Russia), Vilnius State University (Vilnius, Lithuania), Renn University (Renn, France), Karlsruhe Institute of Technology (Karlsruhe, Germany), Leibniz Institute of Photonic Technology (Jena, Germany).

Al-Farabi Kazakh National University,
Faculty of Physics and Technology

Institute of Experimental and
Theoretical Physics

National Nanotechnological Laboratory
of Open Type